ABSTRACT

ISOBARIC ANALOG STATE TRANSITIONS IN (p,n) REACTIONS ON ^{48}Ca, ^{90}Zr, ^{120}Sn, AND ^{208}Pb AT 25, 35, AND 45 MeV

By

Robert Reid Doering

Differential cross sections have been measured for (p,n) reactions to the isobaric analogs of the targets ^{48}Ca, ^{90}Zr, ^{120}Sn, and ^{208}Pb at proton bombarding energies of 25, 35, and 45 MeV. The angular distributions include 0° and generally extend from 10° to 160° in 5° steps. Neutron spectra at these scattering angles have been obtained with the time-of-flight technique. The isospin-flip strength of a phenomenological nucleon-nucleon force has been determined with microscopic DWBA calculations including the "knockon" exchange amplitude. The strength required to fit the data decreases with increasing bombarding energy. At the higher proton energies a realistic G-matrix effective interaction also provides a reasonable account of the observed angular distributions.

ISOBARIC ANALOG STATE TRANSITIONS IN (p,n) REACTIONS ON ^{48}Ca, ^{90}Zr, ^{120}Sn, AND ^{208}Pb AT 25, 35, AND 45 MeV

By

Robert Reid Doering

A THESIS

Submitted to

Michigan State University

in partial fulfillment of the requirements

for the degree of

DOCTOR OF PHILOSOPHY

Department of Physics

1974

ACKNOWLEDGEMENTS

I would like to thank the entire staff of the Michigan State University Cyclotron Laboratory for their patient assistance with many essential aspects of this work. I am also grateful to Professor George Bertsch and Professor Hugh McManus for providing answers to numerous theoretical questions.

Dr. Don Patterson has actively participated in the experimental phase of this project, and I am indebted to him for his many contributions. Jim Branson also aided with the data collection and reduction, in addition to assembling the neutron detector.

Finally, I would especially like to thank Professor Aaron Galonsky for his assistance, encouragement, and guidance.

TABLE OF CONTENTS

LIST OF TABLES v

LIST OF FIGURES vi

I. INTRODUCTION 1

A. Nuclear Forces 1

B. (p,n)-IAS Reactions 11

II. EXPERIMENTAL TECHNIQUE 19

A. The Proton Beam 19
1. The Cyclotron 19
2. The Beam Transport System 20

B. The Scattering Geometry 25
1. The 0^{o} System 25
2. The 10-160^{o} System 27

C. The Detectors 31
1. The Proton Monitor 31
2. The Neutron Detector 32

D. Electronics 36
1. The LIGHT Signal 36
2. The PSD Signal 38
3. The TOF Signal 39
4. The Monitor Signal 39

E. Data Acquisition 40
1. TOF Spectra 40
2. Monitor Spectra 68
3. Charge Collection 70
4. Dead-Time Measurement 71

F. Data Reduction 72
1. Spectrum Calibration 72
2. Peak Fitting 75
3. Neutron Detection Efficiency 79

4. Neutron Attenuation 89
5. Targets 90
6. Cross Sections 93

III. DATA ANALYSIS 101

A. Calculations 101

B. Results 106

LIST OF REFERENCES 110

LIST OF TABLES

1.	Neutron Resolution Function	76
2.	Gamma-Ray Sources for Neutron Detector Calibration	82
3.	Neutron Attenuation (E_n = 11.59 MeV)	91
4.	Target Data	92
5.	Measured Differential Cross Sections	95
6.	(p,n)-IAS Total Cross Sections	100

LIST OF FIGURES

1. Experimental Area of the M.S.U. Cyclotron Laboratory 22
2. Horizontal Acceptance of the Beam Transport System Following the Target 23
3. Vertical Acceptance of the Beam Transport System Following the Target 24
4. Small-Angle Scattering of Protons from a Typical Target 26
5. Neutron-TOF Beam Line and Detector Cart 28
6. Neutron-TOF Scattering Chamber and Quadrupole Triplet 30
7. Neutron-Detector Preassembly 33
8. Electronics 37
9. LIGHT-PSD Histogram 41
10. Neutron and Gamma-Ray Bands in the LIGHT-PSD Plane 43
11. Neutron and Gamma-Ray TOF Spectra at 0° for 25-MeV Protons on ^{48}Ca 45
12. Neutron and Gamma-Ray TOF Spectra at 0° for 25-MeV Protons on ^{90}Zr 46

13. Neutron and Gamma-Ray TOF Spectra at 0° for 25-MeV Protons on ^{120}Sn 47

14. Neutron and Gamma-Ray TOF Spectra at 0° for 25-MeV Protons on ^{208}Pb 48

15. Neutron and Gamma-Ray TOF Spectra at 0° for 35-MeV Protons on ^{48}Ca 49

16. Neutron and Gamma-Ray TOF Spectra at 0° for 35-MeV Protons on ^{90}Zr 50

17. Neutron and Gamma-Ray TOF Spectra at 0° for 35-MeV Protons on ^{120}Sn 51

18. Neutron and Gamma-Ray TOF Spectra at 0° for 35-MeV Protons on ^{208}Pb 52

19. Neutron and Gamma-Ray TOF Spectra at 0° for 45-MeV Protons on ^{48}Ca 53

20. Neutron and Gamma-Ray TOF Spectra at 0° for 45-MeV Protons on ^{90}Zr 54

21. Neutron and Gamma-Ray TOF Spectra at 0° for 45-MeV Protons on ^{120}Sn 55

22. Neutron and Gamma-Ray TOF Spectra at 0° for 45-MeV Protons on ^{208}Pb 56

23. IAS-Neutron and Gamma-Ray Arrival Times for E_p=25 MeV 59

24. IAS-Neutron and Gamma-Ray Arrival Times for E_p=35 MeV 60

25. IAS-Neutron and Gamma-Ray Arrival Times for E_p=45 MeV 61

26. Energy vs. RF for the M.S.U. Cyclotron 62

27. Doubled Neutron-TOF Spectrum 64

28. Typical Neutron-Energy Resolution 67

29. Proton-Monitor Spectrum Resolving the 1.87-MeV, 1.17-MeV, and Ground States of ^{120}Sn at E_p=45 MeV 69

30. Gaussian-Plus-Quadratic Fit to a Lorentzian Peak 78

31. IAS of ^{208}Pb Fit with Lorentzian (solid) and Gaussian (dashed) Peaks Plus Quadratic Background 80

32. Fit to the Compton Edge for 1.275-MeV Gamma Rays from ^{22}Na 83

33. Light Resolution of the Neutron Detector 84

34. Light-Threshold Calibration of the Neutron Detector 86

35. Efficiency of the Neutron Detector 88

36. Comparison of Experimental and Theoretical (p,n)-IAS Angular Distributions 102

I. INTRODUCTION

A. Nuclear Forces

For almost three hundred years, physicists have attempted to account for natural phenomena in terms of mutual forces between material bodies. Although the venerable Newtonian laws (Ne 87) are presently recognized as approximations most appropriate for macroscopic physical systems, the term "force" is still employed to denote the interactions between elementary particles. On the basis of vastly different strengths and symmetry properties, all known interactions have been classified as manifestations of four fundamental forces: gravitational, "weak," electromagnetic, and "strong" (Fe 62). The latter is also referred to as "the nuclear force," since it is primarily responsible for binding protons and neutrons into stable nuclei.

In addition to being the strongest, the nuclear force also appears to be the most complex. The most general expression for the corresponding potential energy between two nucleons, assuming translational, rotational, Galilean, space-reflection, and time-reversal invariance together with charge independence, permutation symmetry, and hermiticity, is

$$
\begin{aligned}
v_{ij} = {} & v_0 + (\underline{\sigma}_i \cdot \underline{\sigma}_j) v_\sigma + (\underline{\tau}_i \cdot \underline{\tau}_j) v_\tau \qquad \text{(I-1)} \\
& + (\underline{\sigma}_i \cdot \underline{\sigma}_j)(\underline{\tau}_i \cdot \underline{\tau}_j) v_{\sigma\tau} + (\underline{L} \cdot \underline{S}) v_{LS} \\
& + (\underline{L} \cdot \underline{S})(\underline{\tau}_i \cdot \underline{\tau}_j) v_{LS\tau} + S_{ij} v_T + S_{ij}(\underline{\tau}_i \cdot \underline{\tau}_j) v_{T\tau} \\
& + L_{ij} v_{LL} + L_{ij}(\underline{\tau}_i \cdot \underline{\tau}_j) v_{LL\tau} + (\underline{\sigma}_i \cdot \underline{p})(\underline{\sigma}_j \cdot \underline{p}) v_{\sigma p} \\
& + (\underline{\sigma}_i \cdot \underline{p})(\underline{\sigma}_j \cdot \underline{p})(\underline{\tau}_i \cdot \underline{\tau}_j) v_{\sigma p\tau} \\
& + \text{Hermitian conjugate},
\end{aligned}
$$

where

$$
\begin{aligned}
S_{ij} &= 3(\underline{\sigma}_i \cdot \underline{r})(\underline{\sigma}_j \cdot \underline{r})/r^2 - (\underline{\sigma}_i \cdot \underline{\sigma}_j), \\
L_{ij} &= \tfrac{1}{2}(\underline{\sigma}_i \cdot \underline{L})(\underline{\sigma}_j \cdot \underline{L}) + \tfrac{1}{2}(\underline{\sigma}_j \cdot \underline{L})(\underline{\sigma}_i \cdot \underline{L}), \\
\underline{L} &= \underline{r} \times \underline{p}, \\
\underline{S} &= \underline{s}_i + \underline{s}_j, \\
\underline{r} &= \underline{r}_j - \underline{r}_i, \\
\underline{p} &= \underline{p}_j - \underline{p}_i;
\end{aligned}
$$

$\underline{r}_i$, $\underline{p}_i$, $\underline{\sigma}_i$, and $\underline{\tau}_i$, are the position, momentum, and Pauli spin and isospin operators, respectively, of the individual nucleons, and each term is a function of r^2, p^2, and L^2 (Ok 58). Thus far, it has not been possible to unambiguously derive these functions from a fundamental theory of nuclear forces, although the exchange of pi mesons appears to account for the long-range part of the potential (Ro 67). However, several attempts to fit nucleon-nucleon scattering data with phenomenological potentials of the general form given by Equation I-1 have been reasonably successful. In

particular, the Hamada-Johnston (Ha 62) and Reid (Re 68) potentials reproduce the bulk of the scattering measurements at nucleon energies up to the threshold for meson production, which is about 300 MeV.

The systems of interest in nuclear physics generally contain more than two nucleons. Although, in principle explicitly many-body forces are present in nuclei, calculations indicate that they contribute less than 10% of the binding energy (Be 72A). Thus, the previously discussed two-body potential is considered to dominate nuclear structure and reactions induced by projectiles with energies less than about 300 MeV per nucleon. Therefore, a sufficiently general nuclear Hamiltonian for most purposes is

$$\mathcal{H} = \sum_i k_i + \sum_{i<j} v_{ij}, \qquad \text{(I-2)}$$

where k_i is the kinetic energy operator for a particular nucleon and v_{ij} is the aforementioned nucleon-nucleon potential.

Scattering experiments have provided most of the detailed information which has been accumulated about nuclear systems. The immediate objective of most scattering experiments is the measurement of cross sections, which are proportional to the probabilities that transitions will occur between specific initially prepared and

finally observed states. For the nucleon-nucleus scattering problem, it is convenient to group the individual kinetic and potential energies in Equation I-2 into the form

$$\mathcal{H} = H_0 + V_0 \qquad \text{(I-3)}$$

where

$$H_0 = H_A + k_0,$$

$$V_0 = \sum_{i=1}^{A} v_{i0},$$

0 labels the projectile, and H_A includes all terms containing only the coordinates of the A target nucleons. The differential cross section for a particular scattering transition is then given by

$$\sigma_{FI}(\theta) = \frac{1}{h v_I} \left| T^D_{FI} - A T^E_{FI} \right|^2_{E_F=E_I} \rho_F(E_I), \qquad \text{(I-4)}$$

where

$$T^D_{FI} = \langle \Psi_{0F} \mid V_0 \mid \Psi^{(+)}_{0I} \rangle,$$

$$T^E_{FI} = \langle \Psi_{1F} \mid V_1 \mid \Psi^{(+)}_{0I} \rangle,$$

$$H_0 \Psi_{0\underset{F}{I}} = E_{\underset{F}{I}} \Psi_{0\underset{F}{I}},$$

$$\Psi^{(+)}_{0I} = \Psi_{0I} + \frac{1}{E_I - H_0 + i\epsilon} V_0 \Psi^{(+)}_{0I},$$

I and F label the initial and final states, respectively, θ is the scattering angle, h is Planck's constant, v_I is the initial velocity of the projectile relative to the target, ρ_F is the energy density of final states, and it is understood that all matrix elements are ultimately evaluated in the limit $\epsilon \to 0$ (Ro 67A). The first term of Equation I-4 is the amplitude for "direct" scattering of the projectile, whereas, the second term represents "exchange" scattering, in which the projectile is interchanged with the target nucleon labeled 1. The exchange amplitude results from the necessity to antisymmetrize the initial and final states with respect to the coordinates of the projectile and the indistinguishable nucleons in the target.

Even with two-body potentials, the many-body problem for the scattering amplitudes in Equation I-4 cannot be solved exactly with presently available mathematical techniques. Furthermore, the projectile-target interaction is generally too strong for a direct perturbation expansion. However, it is often possible to obtain reasonable approximations to the actual scattering amplitude by expanding about the amplitude for an auxiliary one-body potential which may be treated exactly. An arbitrary potential in the space of the relative projectile-target coordinate may be introduced by

$$V_0 = U_0 + (V_0 - U_0). \qquad \text{(I-5)}$$

The direct scattering amplitude is then given by

$$T_{FI}^{D} = \langle \Psi_F \mid U \mid \chi_I^{(+)} \rangle + \langle \chi_F^{(-)} \mid (V-U) \mid \Psi_I^{(+)} \rangle , \tag{I-6}$$

where the projectile label has been dropped and

$$\chi_{F\,I}^{(\pm)} = \Psi_{F\,I} + \frac{1}{E_F - H \pm i\epsilon} U \chi_{F\,I}^{(\pm)}$$

defines the "distorted waves" which describe elastic scattering by the auxiliary potential (Go 64). The first term of Equation I-6 vanishes if the initial and final states of the target are not identical, since they are orthogonal and unaffected by the one-body potential. Thus, Equation I-6 reduces to

$$T_{FI}^{D} = \langle \chi_F^{(-)} \mid (V-U) \mid \Psi_I^{(+)} \rangle \tag{I-7}$$

for inelastic scattering. In terms of the initial distorted wave, the eigenstate of the total Hamiltonian subject to the appropriate boundary conditions on the incident and outgoing waves is given by

$$\Psi_I^{(+)} = \chi_I^{(+)} + \frac{1}{e}(V-U)\,\Psi_I^{(+)} , \tag{I-8}$$

where the energy denominator is defined by

$$e = E_I - H - U + i\epsilon .$$

Thus, the wave operator defined by

$$\Psi_I^{(+)} = \Omega \chi_I^{(+)} \qquad \text{(I-9)}$$

satisfies

$$\Omega = 1 + \frac{1}{e}(V-U)\Omega \,. \qquad \text{(I-10)}$$

Substituting Equation I-9 into Equation I-7 produces

$$T_{FI}^{D} = \langle \chi_F^{(-)} \mid (V-U) \mid \Omega \chi_I^{(+)} \rangle \,. \qquad \text{(I-11)}$$

Equation I-10 may be used to expand this exact expression for the direct scattering amplitude in "powers" of (V-U). Retaining only the first-order term of such a series yields

$$T_{FI}^{D} \approx \sum_{i=1}^{A} \langle \chi_F^{(-)} \mid v_i \mid \chi_I^{(+)} \rangle \,, \qquad \text{(I-12)}$$

which is the usual "distorted-wave Born approximation" (DWBA).

The DWBA may be adequate when an auxiliary potential which accurately represents the bulk of the nucleon-nucleus interaction is employed. The common choice for U is an "optical-model" potential obtained from fitting elastic scattering data. The removal of probability flux from the elastic channel by inelastic scattering and other reactions is accounted for in the optical model with an imaginary term in U. However, despite such refinements in the auxiliary potential, the

distorted-wave Born series generally fails to converge for the currently popular versions of the free nucleon-nucleon force. For example, the DWBA amplitude given by Equation I-12 would be infinite for the Hamada-Johnston potential, unless the distorted waves contained no overlap of the projectile and target nucleons within the "hard-core" radius ($v_{ij}(r \leq 0.485\ F) = \infty$).

Fortunately, the multiple-scattering formalism of Watson (Wa 57) allows v_i to be replaced with an effective two-body scattering operator which is less pathological. The essential idea is to rearrange the expansion for the scattering amplitude so that the basic interaction includes multiple scattering by a particular target nucleon as the projectile propagates under the average influence of the entire target, as represented by an optical potential for elastic scattering. Such an effective scattering operator may be defined by

$$t_i^e = w_i + w_i \frac{1}{e} t_i^e, \qquad \text{(I-13)}$$

where the residual interaction is related to the free two-nucleon potential by

$$w_i = v_i - u_i,$$
$$u_i = \langle \Phi_I \mid v_i \Omega \mid \Phi_I \rangle,$$

and

$$H_A \Phi_I = E_I^A \Phi_I.$$

To first order in t_i^e, the direct scattering amplitude is given by

$$T_{FI}^{D} \approx \sum_{i=1}^{A} \langle \chi_F^{(-)} \mid t_i^e \mid \chi_I^{(+)} \rangle \qquad \text{(I-14)}$$

(Ro 67A). This is known as "the single-inelastic-scattering approximation" (Go 64), since it neglects virtual excitation of the target in intermediate states. Disregarding such processes is an essential feature of the microscopic-direct-interaction" concept of nuclear reactions (Au 70A). However, intermediate excitations are obviously important for a reaction known to proceed through a metastable "compound nucleus" (Vo 68). Thus, the single-inelastic-scattering approximation may only be expected to give a reasonable account of reactions induced by projectiles which bring sufficient energy into the compound nucleus so that the probability of its decay to any particular final state is small compared to that for the competing direct-reaction process. For nucleon-nucleus elastic scattering, the compound-nucleus reaction mechanism appears to be relatively unimportant for bombarding energies above about 10 MeV (Be 69).

Determinations of the appropriate effective interactions and distorted waves are, of course, prerequisite for practical applications of Equation I-14. In general,

the first of these problems involves the solution of Equation I-13, which is intractable with the full many-body propagator. However, if the effect of the remaining target nucleons on the scattering by a particular one is neglected, Equation I-13 may be reduced to

$$t_i^f = v_i + v_i \frac{1}{E_I - k_0 - k_i + i\epsilon} t_i^f, \qquad \text{(I-15)}$$

which is just the free nucleon-nucleon scattering operator. Using the free interaction in Equation I-14 results in the "impulse approximation," which has been demonstrated to be useful for nucleon-nucleus scattering at energies greater than about 100 MeV (Ke 59). At lower energies, the scattering of a pair of nucleons is influenced to a greater extent by the proximity of others. This subject has been studied extensively in relation to nuclear structure (Ba 73), and it has been suggested that the effective interactions used in structure calculations may also be appropriate for "medium-energy" nucleon-nucleus scattering (Pe 70). It seems plausible that a bound target nucleon should not interact much differently with its neighbors than with a free nucleon possessing a kinetic energy only a few tens of MeV greater. Indeed, Watson's approach to multiple scattering has also been adapted to the

derivation of expressions similar to Equation I-13 for bound-state effective interactions. In particular, a "G-matrix" effective interaction may be obtained from Equation I-13 by replacing the complex optical-model potential with a purely real Hartree-Fock or "shell-model" potential, including the Pauli projection operator in the propagator, and deleting the $i\epsilon$ (Ba 72). The most significant difference is probably the lack of an imaginary term in the bound-state case. Nevertheless, G-matrix effective interactions have given reasonable descriptions of nucleon inelastic scattering (Lo 70, Pe 70) and the real part of the proton-nucleus optical potential (Sl 68).

B. (p,n)-IAS Reactions

The distorted waves in Equation I-14 contain the initial and final states of the target in addition to the wavefunctions for the relative projectile-target coordinate which are more commonly referred to as "the distorted waves." Thus, the scattering amplitude depends on the bound states of H_A as well as the effective nucleon-nucleon interaction. Therefore, if the latter were well established, it would be possible to investigate nuclear structure with nucleon-nucleus scattering. However, as is indicated in Section I.A,

the calculation of a realistic effective interaction from a free nucleon-nucleon potential is a formidable undertaking. Furthermore, it is difficult to estimate the effects of the approximations used to calculate interactions on the structure information extracted with them. Thus, it has been suggested that phenomenological effective interactions should be determined from scattering experiments involving nuclei with relatively well-understood structure so that a "calibrated spectrometer" would be available for exploring more obscure nuclear wavefunctions (Sa 67).

In general, direct nuclear reactions with large cross sections proceed predominantly via the central-force part of the nucleon-nucleon interaction, the standard phenomenological form of which is given by

$$\begin{aligned} t^{e}_{ij} = {} & V_0 g_0(r_{ij}) + V_\sigma g_\sigma(r_{ij}) \underline{\sigma}_i \cdot \underline{\sigma}_j \\ & + V_\tau g_\tau(r_{ij}) \underline{\tau}_i \cdot \underline{\tau}_j \\ & + V_{\sigma\tau} g_{\sigma\tau}(r_{ij}) \underline{\sigma}_i \cdot \underline{\sigma}_j \underline{\tau}_i \cdot \underline{\tau}_j , \end{aligned} \qquad \text{(I-16)}$$

which is a local parameterization of the effective scattering operator, patterned after the corresponding terms in the general two-body potential of Equation I-1 (Au 70A). For simplicity, a common radial function of either Gaussian or Yukawa form is usually selected. Attempts to extract the associated empirical strengths

from nucleon-nucleus scattering data have been reviewed by Austin (Au 72). Assuming a Yukawa radial dependence given by

$$g(r) = \frac{\exp(r/\mu)}{(r/\mu)}, \qquad \text{(I-17)}$$

with a range (μ) of 1.0 F, he concludes that $V_0 = -27 \pm 5$ MeV, $V_{\sigma\tau} = 12 \pm 2\frac{1}{2}$ MeV, and that V_σ and V_τ are poorly determined. In particular, his compilation includes values of V_τ from below 10 to nearly 30 MeV.

The present study concentrates on obtaining more precise knowledge of the purely isospin-dependent part of the effective nucleon-nucleon interaction, which refers to the third term of Equation I-16. This term may be isolated by considering transitions from the ground state (GS) of a target with mass number A, composed of Z protons and N neutrons, to its "isobaric analog state" (IAS) in the "residual" nucleus with Z+1 protons and N-1 neutrons. The IAS may be defined in terms of the action of the "isospin-lowering" operator (T^-) on the target ground state by

$$\Phi_{IAS}(T=T_>, T_z=T_<) = (2T_>)^{-\frac{1}{2}} T^- \Phi_{GS}(T=T_>, T_z=T_>), \qquad \text{(I-18)}$$

where

$$T^\pm = \sum_{i=1}^{A} t_i^\pm,$$

$$t_i^{\pm} = t_i^x \pm i t_i^y,$$

$$\underline{t}_i = \tfrac{1}{2}\underline{\tau}_i,$$

$$T_> = \tfrac{1}{2}(N-Z),$$

and

$$T_< = T_> - 1.$$

As Equation I-18 indicates, the isospin-lowering operator creates the IAS by reducing the z-component of the target isospin by one unit while conserving the magnitude of T. Since the z-component of isospin is defined as half the neutron excess (in the usual nuclear physics convention), the isospin-lowering operation amounts to converting an excess neutron into a proton. If there is only one excess neutron in the target, the IAS will be the ground state of the "mirror" nucleus. In the general case, the analog of the target ground state will be the first state with $T=T_>$ in the residual nucleus, the lower-energy states having $T=T_z=T_<$. For transitions between isobaric analog states with zero spin and positive parity ($J^\pi=0^+$), the only nonvanishing matrix elements in Equation I-14 will be for the purely "isospin-flip" term of the effective interaction in Equation I-16 (Au 70A). This term contains a scaler product of projectile and target-nucleon isospin operators, which may be expanded as

$$\underline{\tau}_i \cdot \underline{\tau}_0 = 2(t_i^+ t_0^- + t_i^- t_0^+) + 4 t_i^z t_0^z. \qquad \text{(I-19)}$$

The second pair of isospin-raising and lowering operators in Equation I-19 is responsible for "charge-exchange" reactions in which a neutron in the target is converted into a proton while a projectile proton becomes a neutron. Since the isospin-flip term of the effective interaction is the only central-force component which contributes to the direct amplitude for charge-exchange scattering between $J^{\pi}=0^{+}$ analog states, these reactions are quite sensitive to V_{τ}. Except for the smallness of the cross sections typically observed, (^{3}He,t) charge-exchange reactions are the most experimentally convenient means of studying such transitions. Unfortunately, conventional DWBA calculations have often been in relatively poor agreement with the (^{3}He,t) data (Fa 72, Hi 72). Besides the usual optical-model ambiguities for complex projectiles, complications of the reaction mechanism have been proposed. In particular, a (^{3}He,α)(α,t) amplitude larger than the direct amplitude has been calculated for the ^{48}Ca(^{3}He,t)^{48}Sc-IAS reaction at 23 MeV (De 72). Generally accepted optical-model potentials are available for (p,n) charge-exchange reactions, but it has been suggested that "neutron pickup" followed by "proton stripping" may also interfere with the direct amplitude in this case (Ri 73). The significance of (p,d)(d,n) contributions is currently under investigation, and this problem will

not be directly addressed in the present analysis.

The major experimental difficulties associated with (p,n) reactions result from the charge neutrality of the neutrons. Conventional charged-particle detectors generally measure the ionization produced by incident radiation. Since neutrons have no Coulomb interaction with atomic electrons, they must be indirectly detected through the charged products of nuclear reactions which they induce. Unless a "recoil telescope" (Ma 70) is used to define the scattering angle, ionizations created by the reaction products cannot be put into correspondence with unique neutron energies. A popular alternative for obtaining neutron spectra has been to directly determine their velocities. This method requires the accurate measurement of neutron flight times from the target to the detector, which is facilitated by short-duration beam bursts from the proton accelerator, a long flight path, a rapid-response detector, and precision fast-timing electronics. Of course, longer flight paths give smaller solid angles for a given detector, and, thus, some compromise between resolution and count rate is generally necessary.

Anderson and Wong employed the "time-of-flight" technique in the first observations of (p,n)-IAS transitions in nuclei heavier than the mirror pairs (An 61). Their measurements revealed the presence of a strongly

excited state in each residual nucleus at an energy corresponding to the Coulomb energy required to convert a target neutron into a proton (plus the n-p mass difference). At that time, the discovery of isobaric analog states in such heavy nuclei was unexpected, since it was widely believed that isospin conservation would be significantly broken by the electromagnetic force in all but the lightest nuclei (Wi 69). The prominence of heavy-target-ground-state analogs in charge-exchange reactions is presently understood to result mostly from the "dilution" of the isospin impurity of the nuclear core by its coupling to the pure isospin of the neutron excess (So 69, Be 72).

During the past decade, additional (p,n)-IAS experiments have been used to explore the isospin dependence of the nuclear force. However, most of the data has been obtained with proton bombarding energies of less than 30 MeV (An 64, Be 71, Wo 71, Sc 73). The few absolute angular distributions previously measured at energies above 30 MeV are essentially confined to forward angles (Va 65, Ba 68, La 68, Jo 73), and, except for the ^{27}Al(p,n)^{27}Si-IAS data from the Michigan State University Cyclotron Laboratory (Jo 73), these cross sections generally have relative errors of more than 10%.

The present work provides (p,n)-IAS angular distributions from 0^{o} to 160^{o} at proton energies of 25, 35, and 45 MeV for the targets ^{48}Ca, ^{90}Zr, ^{120}Sn, and ^{208}Pb. These nuclei span the range of masses for which a "global" optical-model potential has been obtained (Be 69). In addition, the ground states (and, hence, the analog states) of these targets have $J^{\pi}=0^{+}$ and are considered to be particularly well understood. Thus, this data is well suited to further extend our knowledge of the isospin-flip strength of the effective nucleon-nucleon interaction.

II. EXPERIMENTAL TECHNIQUE

A. The Proton Beam

1. The Cyclotron

The Michigan State University Cyclotron produces approximately 25- to 50-MeV proton beams of exceptional quality for time-of-flight (TOF) experiments. Internal slits restrict the phase width of individual beam pulses to about 2°. At a typical repetition rate of one pulse every 60 nsec, this phase width is equivalent to a time spread of 1/3 nsec. In practice, gamma-ray bursts $\lesssim 0.5$ nsec (FWHM) in duration are typically observed from thin targets intercepting the external proton beam. Widths in the neighborhood of 0.2 nsec (most of which may represent the inherent resolution of the detector and associated electronics) have been achieved by slightly reducing the magnetic field and/or radio frequency from the normal operating values. However, the improved resolution is generally more than offset by the loss of beam intensity also incurred from such a detuning of the cyclotron. During these (p,n) experiments, the current on target was usually between one and four microamps, limited for the tin and lead targets by their relatively low melting points.

2. The Beam Transport System

Figure 1 gives an overview of the "high bay" at the Michigan State University Cyclotron Laboratory. Neutron TOF measurements are conducted in the shielded experimental area designated Vault #5. The angular divergence of the proton beam transported from the cyclotron to Vault #5 is minimized by leaving off the quadrupole magnets labeled Q3 through Q6, thereby requiring greater than normal focal lengths for the remaining quads. This low-divergence mode of the beam transport system results in fewer background neutrons produced by protons striking the beam pipe. It also tends to increase the size of the beam spot on target. However, the spot diameter has been routinely maintained at <0.5 cm (as observed on a quartz scintillator mounted in the target ladder), which contributes negligible uncertainty in the scattering angle to a detector several meters away. In addition to low divergence, the proton beam is delivered to the neutron TOF line with little momentum dispersion, since the -31.5° bend through the dipole magnet M4 removes most of the dispersion introduced by the $+45^{\circ}$ bend at M3. However, the excellent energy resolution ($\Delta E/E \approx 10^{-3}$) of the proton beam completely extracted from the cyclotron on a single turn is seldom a significant fraction of the overall resolution

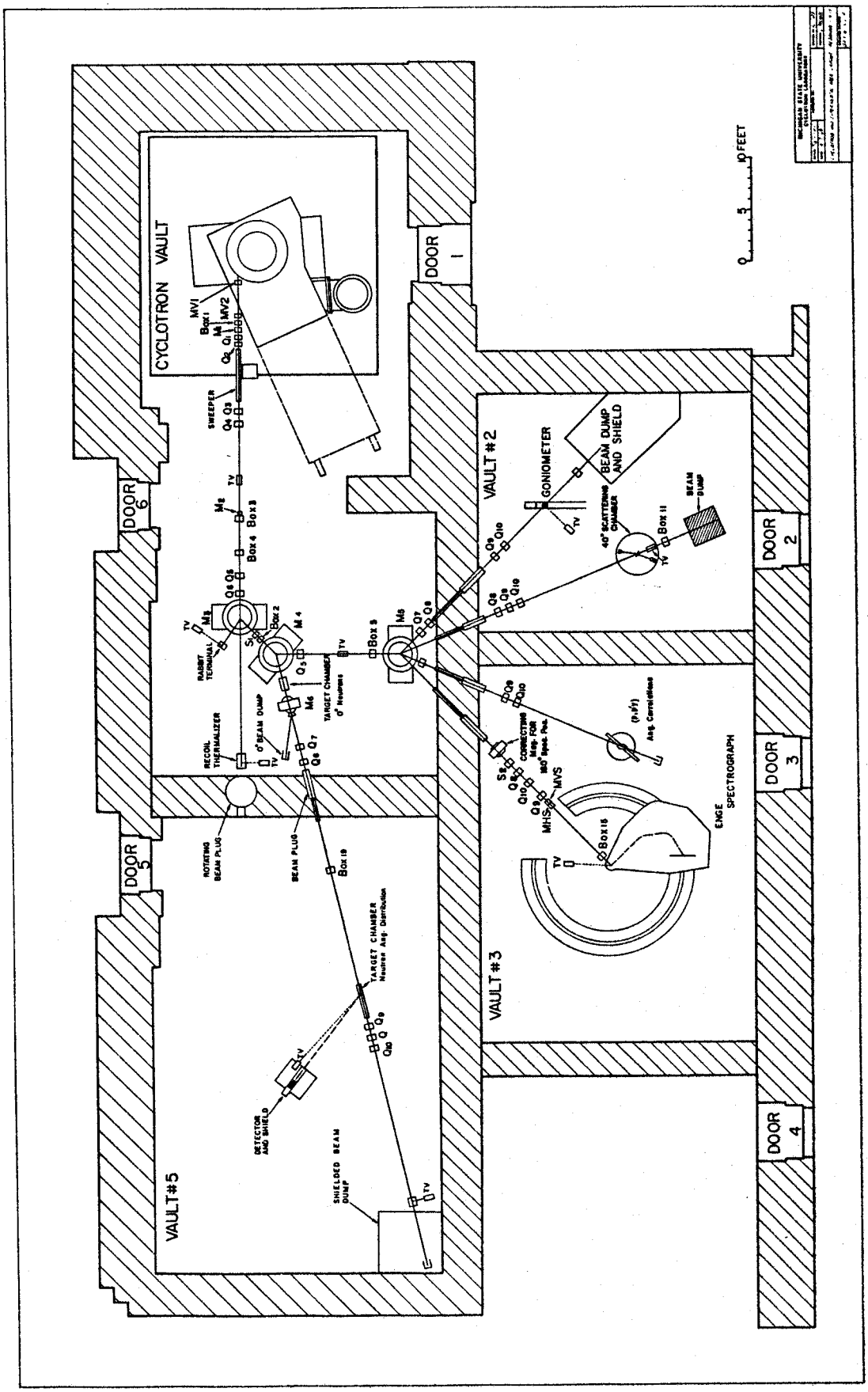

Figure 1. Experimental Area of the M.S.U. Cyclotron Laboratory

for neutron TOF experiments. Thus, it is unnecessary to have a dispersed beam available for momentum analysis. Although external slits are not used to select the beam energy spread, remotely positioned, current-sensitive jaws are employed at Box 1 through Box 4 to collimate and monitor the beam. The slits at Box 19 are used only during initial beam alignment.

With a vacuum of about 2×10^{-5} mm Hg in the line, very few protons are scattered into the beam pipe before they reach the target. The quadrupole triplet beyond the scattering chamber is used to refocus target-scattered protons into the heavily shielded beam dump, thus minimizing background from the final sections of beam pipe. The placement of the quads has been optimized with the aid of beam-optics calculations with the code OPTIK (De 61). Figures 2 and 3 indicate the acceptance of the triplet for transmission of 45-MeV protons. Each point in one of the phase-space planes represents a possible displacement and scattering angle for a proton at the target. For example, the origin corresponds to an undeflected proton passing through the center of the target. The lines indicate grazing trajectories for various apertures between the target and beam dump. Thus, the area bounded by the innermost lines surrounding the origin represents the domain of horizontal or vertical phase space (at the target) containing protons

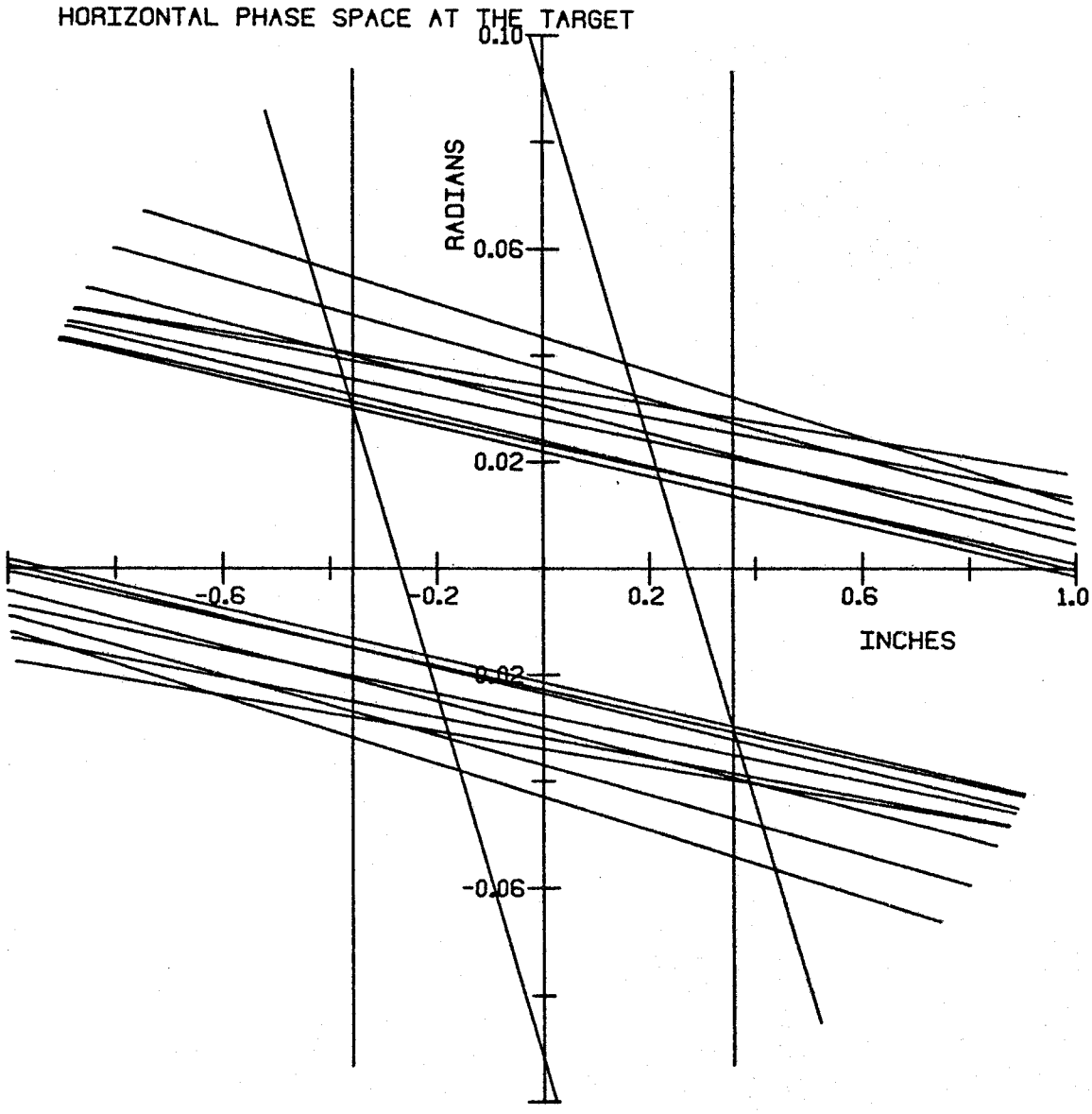

Figure 2. Horizontal Acceptance of the Beam Transport System Following the Target

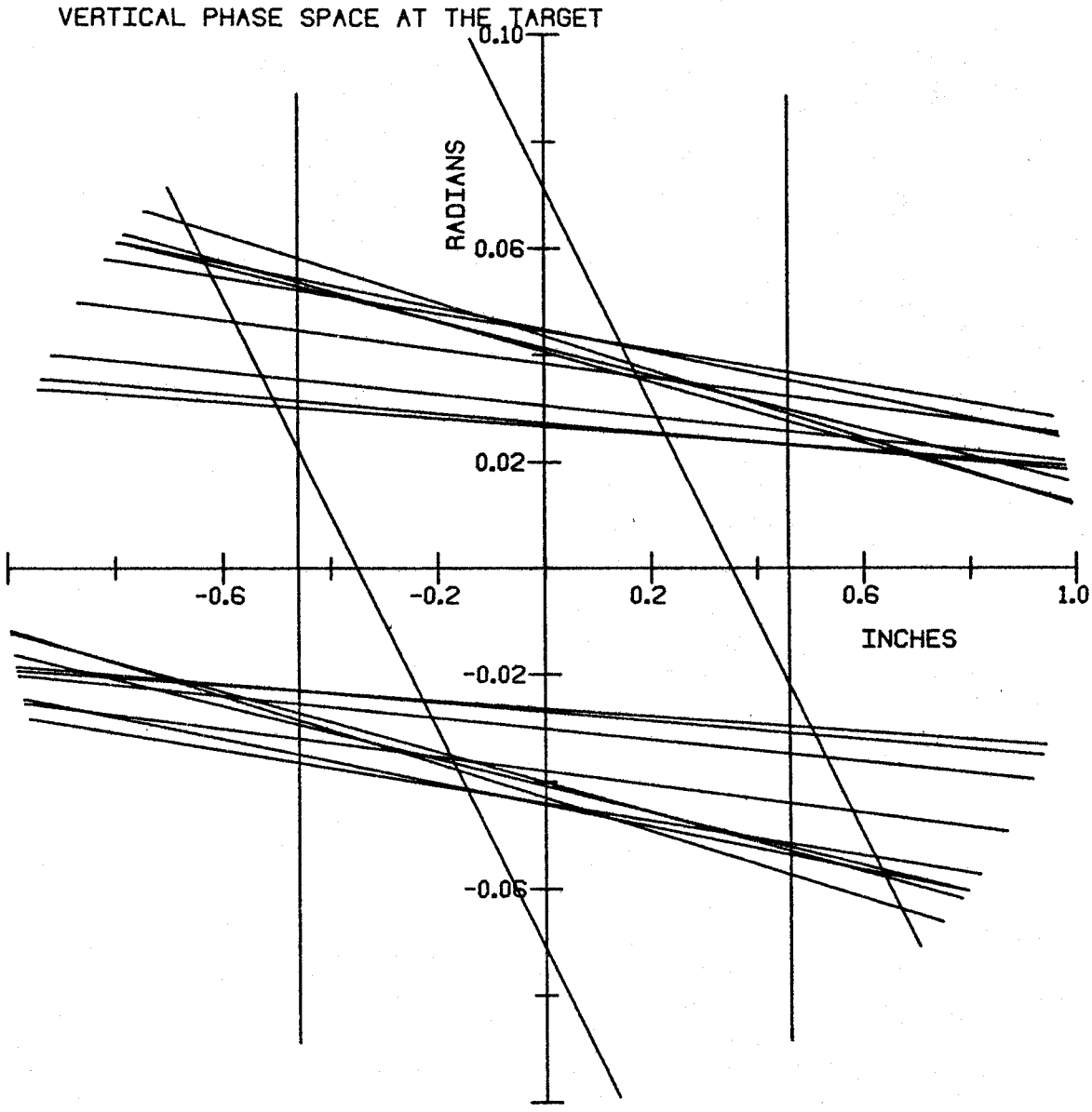

Figure 3. Vertical Acceptance of the Beam Transport System Following the Target

which would be cleanly transported to the dump. These graphs indicate that the limiting horizontal and vertical scattering angles from the center of the target are 0.022 and 0.027 radians, respectively, for 45-MeV protons. Figure 4 displays Rutherford single scattering and multiple scattering at 45 MeV from a typical target used in this experiment. For this case, only about 1% of the protons incident on the target would be deflected into the beam pipe. Multiple scattering has been calculated with the formula of Rossi and Greisen (Se 64).

B. The Scattering Geometry

1. The 0° System

A special experimental arrangement is available for observing neutrons at a scattering angle of 0°. The target ladder is mounted on a box just beyond M4, and M6 is used to bend the beam an additional 20° into an auxiliary Faraday cup. Neutrons from the target exit M6 through a 0.8-mm-thick, aluminum port and traverse several meters of air en route to a detector placed along the partially dismantled beam line. A 13.2-cm-thick, brass collimator with a 2.5-cm-diameter aperture adjacent to the port attenuates neutrons produced on the pole faces of M6. At energies of 35 and 45 MeV, the port has been covered with a 5-mm-thick, lucite

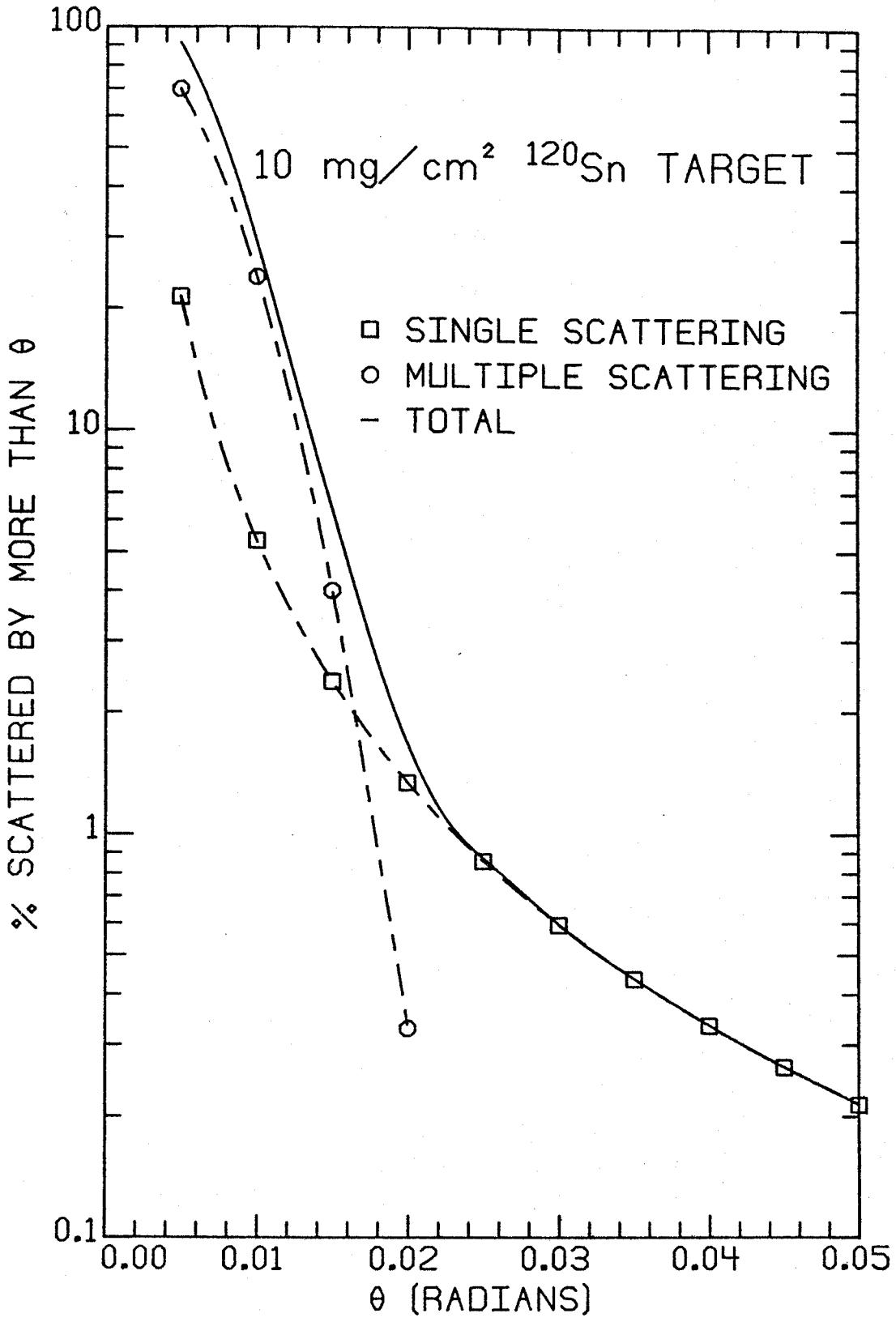

Figure 4. Small-Angle Scattering of Protons from a Typical Target

absorber to prevent protons which pick up an electron in the target and sneak through M6 as neutral hydrogen from reaching the detector. Without this absorber, approximately one 35-MeV proton out of every billion in the beam has been observed at the detector, a ratio consistent with previously measured electron-pickup cross sections (Ta 73).

Especially high quality spectra may be obtained with the 0° setup. Since the beam is dumped in the main vault and the detector is in Vault #5, the background is minimal. In addition, flight paths of up to 15 m are available for the ultimate fractional time resolution.

2. The $10\text{-}160^{\circ}$ System

Figure 5 displays the apparatus used for taking angular distributions from 10° to 160°. The detector rides on a cart which pivots about an axle above the scattering chamber. It is shielded from neutrons and gamma rays not originating in the target by a section of 105-mm gun barrel and stacks of water-filled boxes. The cart floats on an air pad which is pushed by an electric motor to change the observed scattering angle. Both the pad and motor may be remotely operated from the data room. Four closed circuit TV cameras in Vault #5 provide feedback on remote adjustments of the beam and targets as well as the cart. The camera mounted next

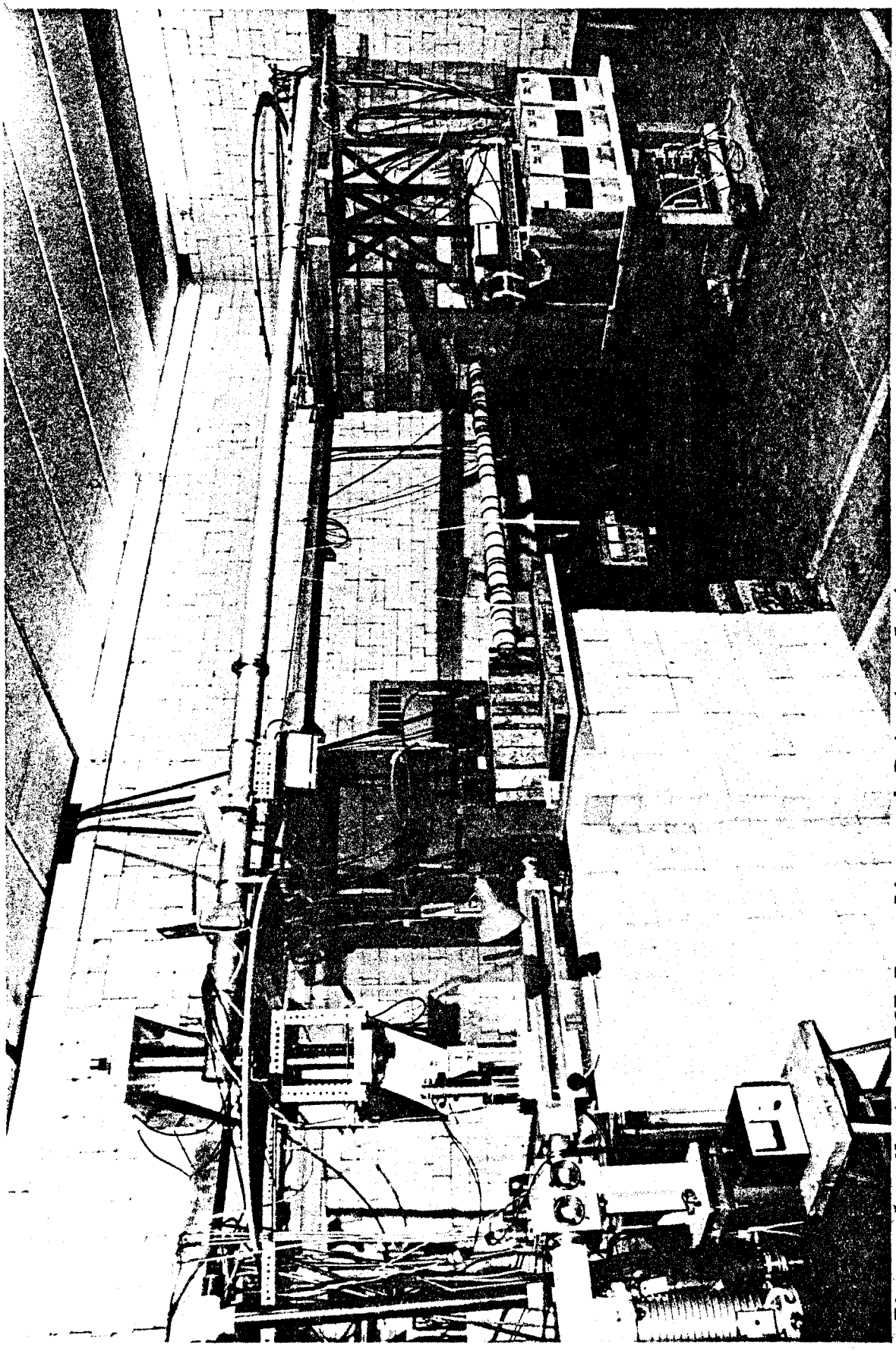

Figure 5. Neutron-TOF Beam Line and Detector Cart

to the gun barrel is equipped with a 300-mm-focal-length lens on a near-focussing adapter. It gives a close-up view of the target ladder for monitoring the alignment of beam spot, target, and gun barrel. The tight collimation afforded by the gun barrel requires that it be accurately aimed at the target. This is difficult to maintain as the heavily loaded cart traverses imperfections in the concrete floor of the vault. The present system of cantilever pipe and guy wires has been found to provide a satisfactory coupling of the cart and pivot. It has enough vertical flexibility to allow the air pad to support the cart, yet sufficient horizontal rigidity to generally maintain the flight path within ± 1 cm and the gun barrel orientation within $\pm\frac{1}{2}^{o}$. The camera attached to the cantilever pipe reads the scattering angle from a fixed scale on the pivot support. The remaining pair of cameras view plunging scintillators which intercept the beam immediately before the target ladder and the beam dump.

The scattering chamber is shown in Figure 6. It is basically a rectangular section of beam pipe with a neutron-exit window and extra ports for the target ladder and monitor detector. The target ladder holds up to six 5-x$2\frac{1}{2}$-cm target frames and provides remotely controlled drives for changing the target angle and height. The neutron window is a sheet of $\frac{1}{4}$-mm-thick

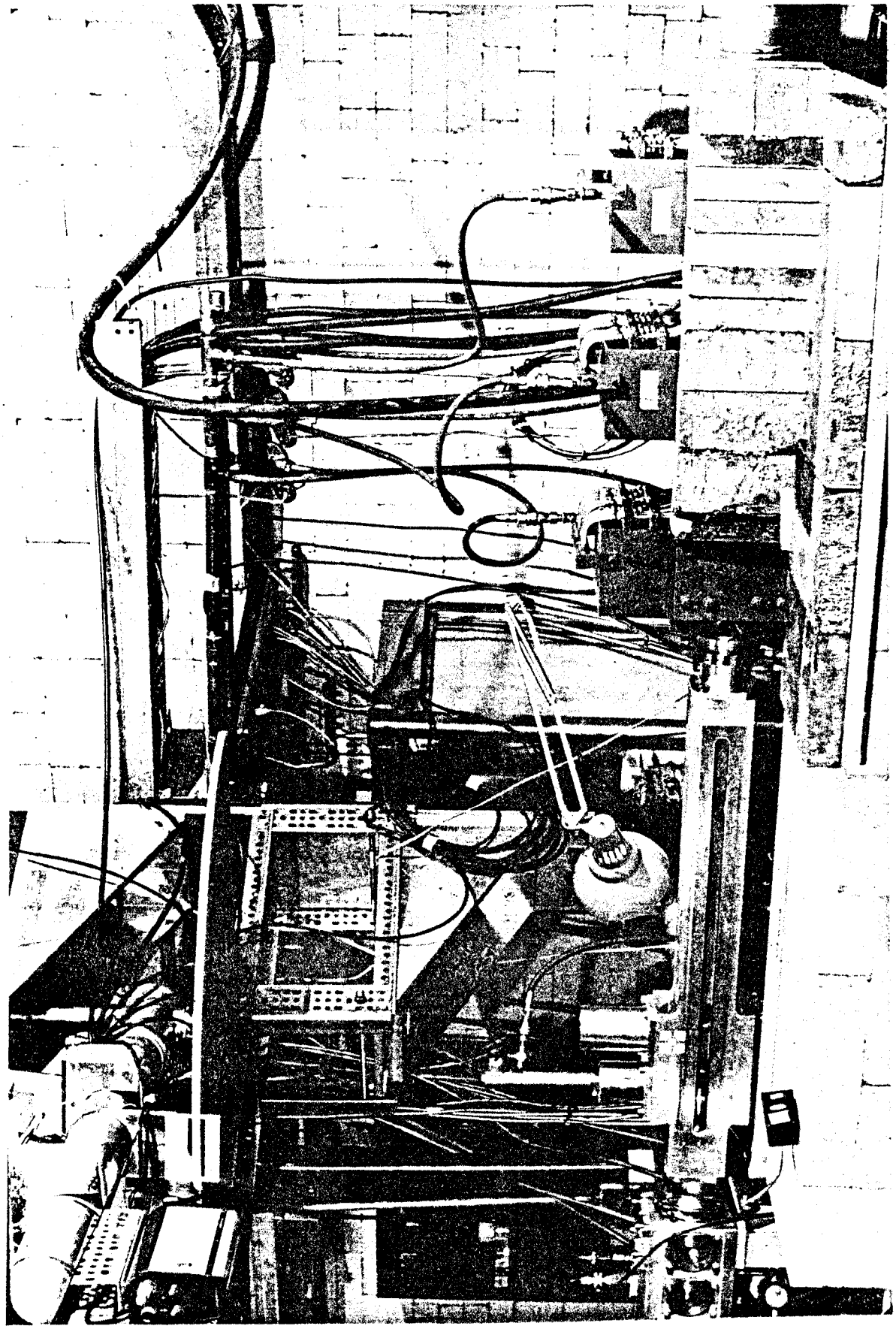

Figure 6. Neutron-TOF Scattering Chamber and Quadrupole Triplet

mylar covering a 2.5-cm-high slot which subtends scattering angles from 6° to 163°.

At selected scattering angles, the neutron detector may be positioned from about 1 to $7\frac{1}{2}$ m from the target. However, the cart can swing over the full angular range of 10° to 160° only for flight paths between approximately 3 and 5 m.

C. The Detectors

1. The Proton Monitor

The monitor detector consists of a 3.2-cm-diameter by 1.3-cm-thick, thallium-activated-NaI scintillator, optically coupled to a 5-cm-diameter RCA 4523 photomultiplier tube. A preamplifier is also included in the detector package. An aluminum window 0.025 mm thick covers the front face of the NaI crystal, and the entire assembly is surrounded by a magnetic shield.

The monitor is used to observe protons scattered through 90° by the target. The protons remain in an evacuated pipe extending from the scattering chamber until they reach a 0.025-mm, stainless steel window 98 cm from the target. Between the steel and aluminum windows is placed a 3.2-mm-thick, brass collimator with a 6.4-mm aperture.

The pulse-height resolution of this detector has been measured to be 8.6% for 662-KeV gamma rays from a ^{137}Cs source. The resolution is principally determined by statistical fluctuations in the number of photons (N) produced in the scintillator by incident particles of a definite energy (E). For large N, the Poisson probability distribution of the number of created photons approaches a Gaussian distribution with a standard deviation of $N^{\frac{1}{2}}$. Since the average number of photons produced is proportional to the available energy, the energy resolution is proportional to $E^{\frac{1}{2}}$. Thus, from the 57-KeV resolution observed for 662-KeV gamma rays, 470-KeV resolution would be expected for 45-MeV protons. This estimate is about 30% below the values achieved in practice. However, the actual monitor resolution provided adequate separation of the elastically and inelastically scattered protons in this experiment for the former to be accurately counted.

2. The Neutron Detector

Figure 7 gives an exploded view of the neutron detector prior to assembly. The heart of this detector is a 7.0-cm-diameter by 3.8-cm-thick volume of the liquid organic scintillator NE 213, which is encapsulated in a glass cell. The walls of the cell are $2\frac{1}{2}$ mm thick

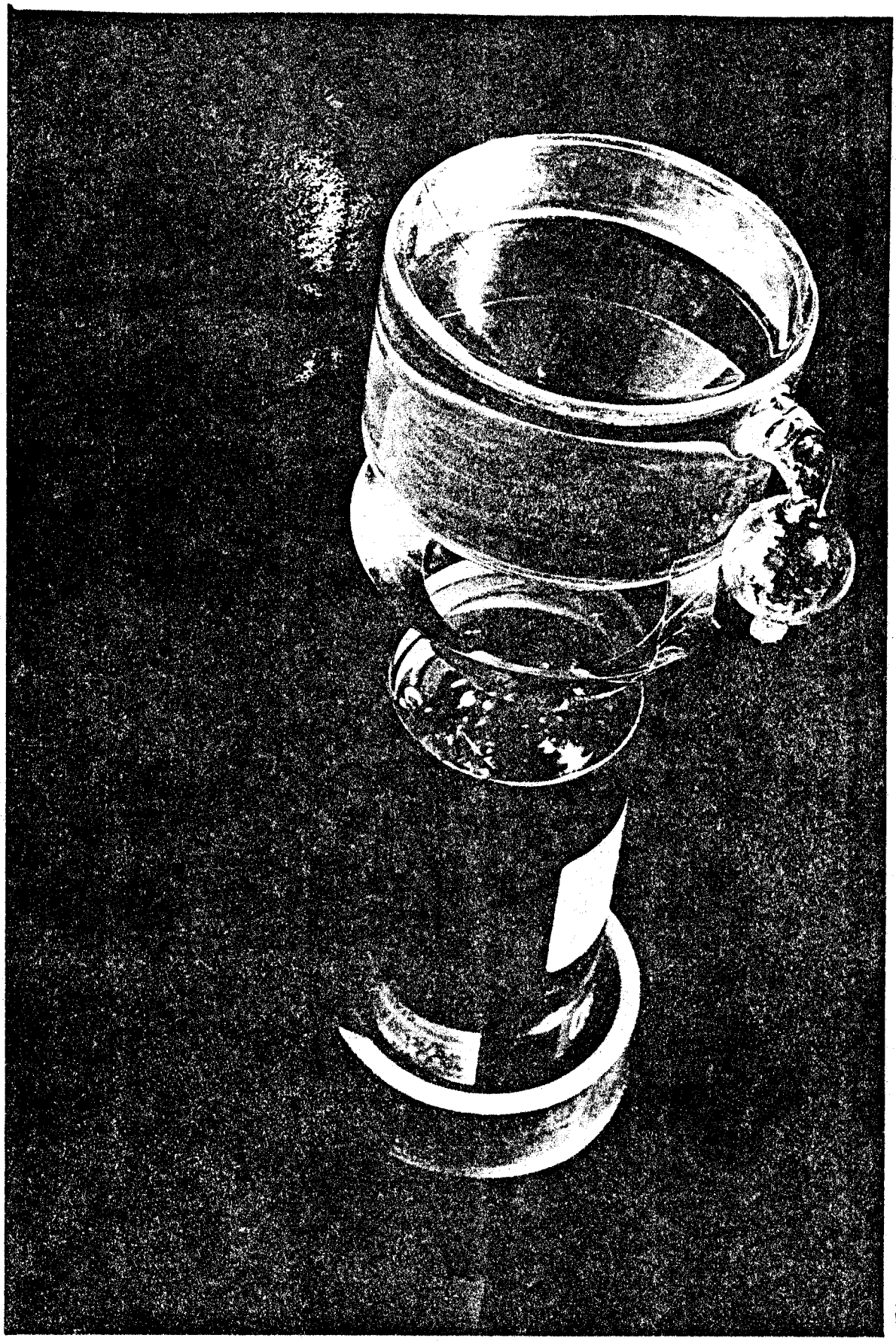

Figure 7. Neutron-Detector Preassembly

both on the flat ends and the curved edge, to which is attached a spherical expansion chamber. The cell is optically and mechanically coupled to a 5 cm diameter RCA 8575 photomultiplier (PM) tube with a 2.5-cm-long, tapered, lucite light pipe. The glass-lucite interfaces are cemented with Dow-Corning Sylgard resin. The light pipe and cell are coated with Eastman White Reflectance Paint, except for the expansion chamber, which is painted flat black. The high reflectance paint is covered with a layer of aluminum foil to insure opacity. The PM tube is also protected against light leaks with a wrapping of black vinyl tape. In addition, it is shielded from external magnetic fields with a cylindrical sheet of Netic supported by felt spacers. As a magnetic shield, this high permeability metal complements the lower permeability, but more difficult to saturate, steel of the gun barrel. The PM tube is plugged into an Ortec 270 Constant Fraction Timing Photomultiplier Base, to which is fastened a protective steel cover for the entire detector assembly.

The detector is "breech-loaded" into the gun, with the center of the scintillator 74 cm from the front of the 113-cm length of barrel. Lucite absorbers of sufficient thickness to stop the maximum energy scattered protons are hung from the contilever pipe about 1 m from the target. For 25-MeV protons, the absorber is 10 cm

high, 6 cm wide, and 0.3 cm thick. At 35 and 45 MeV, the thickness used is 1.2 cm, and the height and width are increased to 40 and 58 cm, respectively, which eliminates most of the protons rescattered by the air toward the detector.

The net detector shielding prevents essentially any radiation except neutrons, gamma rays, and occasional mu mesons (cosmic rays) from reaching the scintillator. Charged particles, such as the mu mesons, produce ionized tracks as they traverse matter. In scintillators with several states of molecular excitation available, the longer-lived states are preferentially populated along densely ionized tracks (Ro 64). Thus, the decay rates of light pulses resulting from molecular de-excitation will reflect the specific energy losses of incident charged particles. Neutral radiation may also interact with the scintillator through various mechanisms to yield detectable charged particles. For example, gamma ray energy is converted into electron energy through Compton scattering, pair production, and the photoelectric effect. Similarly, neutrons may be detected via charged products of nuclear reactions which they induce. In particular, if the scintillator contains hydrogen, ionization will result from protons elastically scattered by incident neutrons. Since this process has relatively

large and well known cross sections (as a function of neutron energy), it has been extensively exploited for neutron detection. A particularly desirable quality of NE 213 for this experiment is the relatively great sensitivity of its light pulse decay shape to specific ionization (Wi 71). This "pulse-shape-discrimination" (PSD) property, coupled with the abundance of hydrogen in its solvent (xylene) and its rapid scintillation response, makes NE 213 ideal for detecting fast neutrons in the presence of a large gamma-ray background.

D. Electronics

1. The LIGHT Signal

Sophisticated electronics are necessary to obtain the maximum amount of information from the fast scintillator light pulses. As the block diagram in Figure 8 indicates, the present system derives three linear signals which characterize a light pulse in terms of its amplitude (LIGHT), decay rate (PSD), and time of occurrence relative to the cyclotron RF (TOF).

The LIGHT signal is picked off at the ninth dynode in the photomultiplier tube by a preamplifier in the PM base. The tail pulse from the preamp is further amplified and shaped by the single-delay-line stage of a Canberra 1411 Double Delay Line Amplifier. The

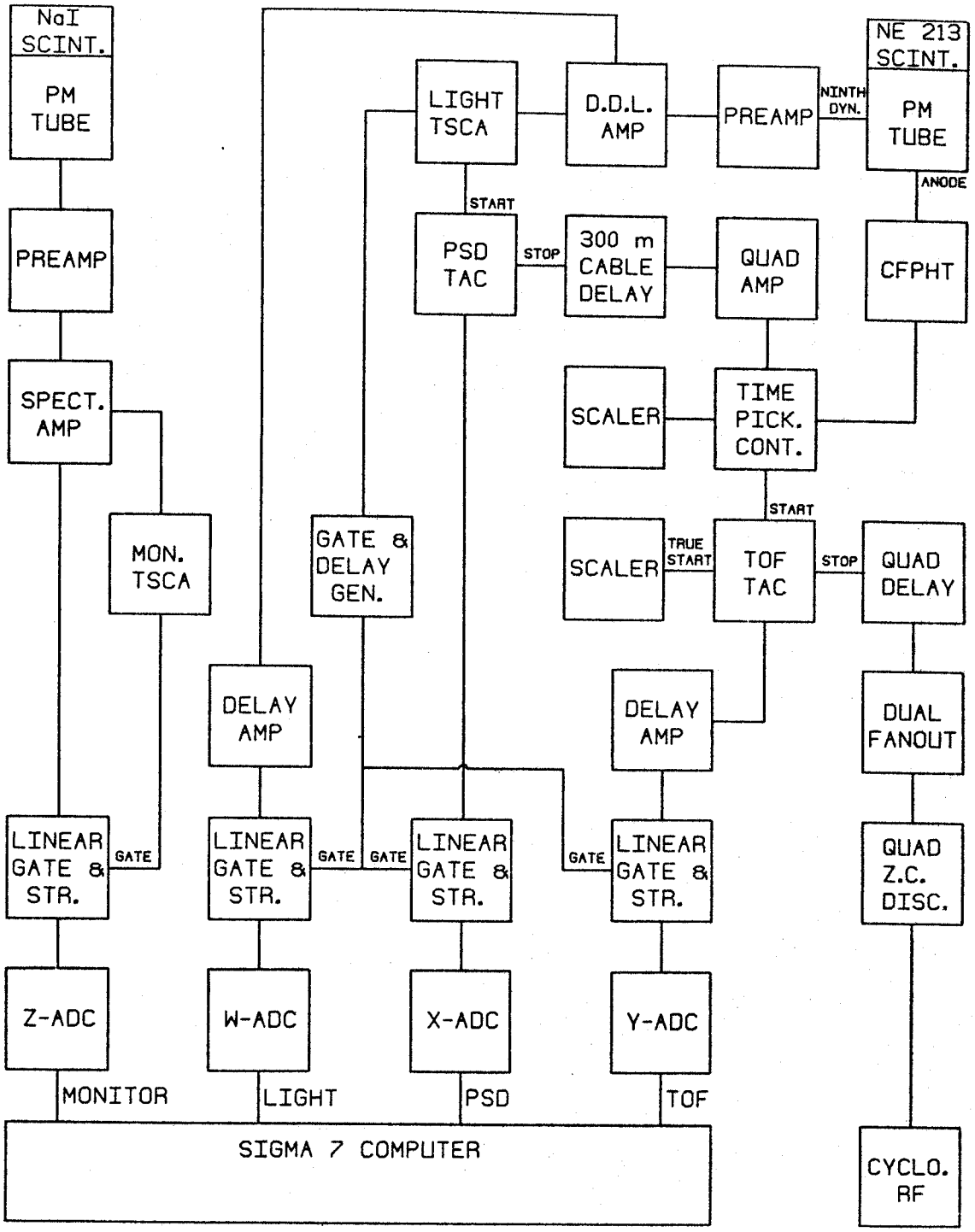

Figure 8. Electronics

resulting unipolar signal is delayed by an Ortec 427A Delay Amplifier until it can be accepted by an Ortec 442 Linear Gate and Stretcher in coincidence with the PSD and TOF signals. Finally, the LIGHT signal is digitized for computer input by a Northern NS-629 Analog to Digital Converter (ADC).

2. The PSD Signal

The double-delay-line output of the shaping amplifier is fed into a Canberra 1436 Timing Single Channel Analyzer (TSCA). If the amplitude of the input bipolar pulse is above a preselected threshold, the TSCA generates a pair of logic signals delayed by a fixed interval from the zero crossing of the input pulse. The positive logic signal is delayed and fanned-out to open the three linear gates by an Ortec 416A Gate and Delay Generator. Since the linear gates remain simultaneously open for only about a microsecond, the LIGHT, PSD, and TOF signals are required to arrive in coincidence. The fast negative logic signal starts an Ortec 437A Time to Pulse Height Converter (TAC). This PSD TAC is stopped by a signal originating in the PM base, where a constant-fraction-of-pulse-height-trigger (CFPHT) circuit generates a fast logic signal when the PM anode pulse reaches 20% of its peak amplitude. This technique of time derivation has been shown to exhibit minimal variation of triggering

time relative to pulses covering a wide dynamic range (Mc 68). Control of the CFPHT threshold and fan-out for the fast logic signal are provided by an Ortec 403A Time Pickoff Control. To prevent the stop signal from reaching the PSD TAC before the start, approximately 300 m of RG-8 cable is employed as a fixed delay. An EG&G AN201/N Quad Amplifier aids in driving the cable delay. The output of the PSD TAC is delivered directly to a linear gate. This system is based on the original "zero-crossover" PSD technique of Alexander and Goulding (Al 61).

3. The TOF Signal

Another fast logic signal from the time-pickoff control starts the TOF TAC. Its stop signal originates with the zero crossing of the cyclotron RF, which is detected by an EG&G T140/N Quad Zero-Crossing Discriminator. The stop signal may be delayed by up to 254 nsec in switch-selectable 0.5-nsec increments by an EG&G DB463 Quad Delay Box. The output of the TOF TAC passes through a delay amplifier to bring it into coincidence with the PSD and LIGHT signals at the linear gates.

4. The Monitor Signal

The output of the preamp in the monitor-detector PM base is further amplified and shaped by an Ortec 451

Spectroscopy Amplifier. The bipolar output of this unit triggers a logic signal output from an Ortec 420A Timing Single-Channel Analyzer when its amplitude is above a preset threshold. This threshold is selected to correspond to a proton energy a few MeV below the elastically scattered protons. Thus, noise and other small pulses resulting from low energy protons, gamma rays, etc. are blocked by the linear gate controlled by the monitor TSCA logic signal.

E. Data Acquisition

1. TOF Spectra

The W-,X-,Y-, and Z-ADC's, which digitize the LIGHT, PSD, TOF, and monitor signals, respectively, are interfaced to the Michigan State University Cyclotron Laboratory Xerox Data Systems Sigma 7 computer. The three linear signals from the neutron detector are analyzed on-line with the data-acquisition code TOOTSIE (Ba 71A).

In the Setup mode of this program, coincident LIGHT and PSD signals are stored as counts in a 128x128-channel array. An example of the resulting two-dimensional histogram is shown in Figure 9. Light pulses with short decay times produce bipolar signals with early zero crossings when twice differentiated by the DDL amplifier.

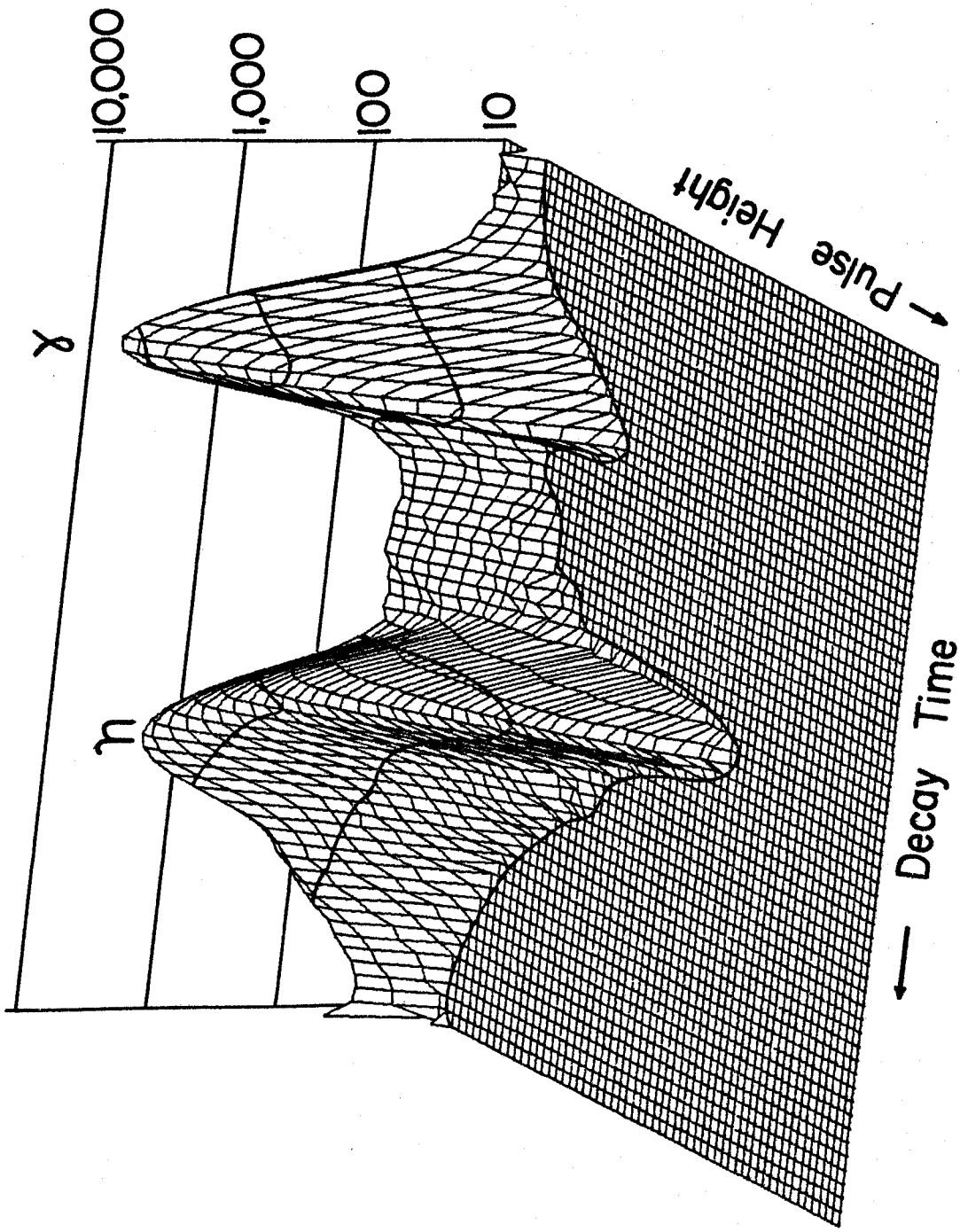

Figure 9. LIGHT-PSD Histogram

Thus, they start the PSD TAC sooner relative to their stop signals than pulses with long decay times and yield larger PSD signals. The largest PSD amplitudes in Figure 9 result almost exclusively from electrons Compton scattered by gamma rays in the scintillator. Since they yield about the same specific ionization as high-energy electrons, "cosmic" mu mesons may also contribute to the "lepton ridge." Protons recoiling from elastic collisions with incident neutrons are responsible for the other prominent cluster of events in Figure 9. Another cluster, due to alpha particles from reactions induced by high-energy neutrons on carbon in the scintillator, has been observed still farther down the PSD axis. The program displays "cross sections" of the histogram, which indicate the channels containing numbers of counts between selected upper and lower bounds. An example of the Setup mode display, as viewed on a Tektronix 611 storage scope, is shown in Figure 10. The user is allowed to define "bands" between pairs of polynomial fits to selected points in the LIGHT-PSD plane. The bands define digital gates used by the program in the Run mode to route TOF signals into separate one-dimensional spectra. For this experiment, "neutron" and "gamma-ray" bands have been drawn around the proton and lepton clusters, respectively. To avoid losing neutrons, the line between the neutron and gamma-ray bands has generally been constructed slightly closer to the

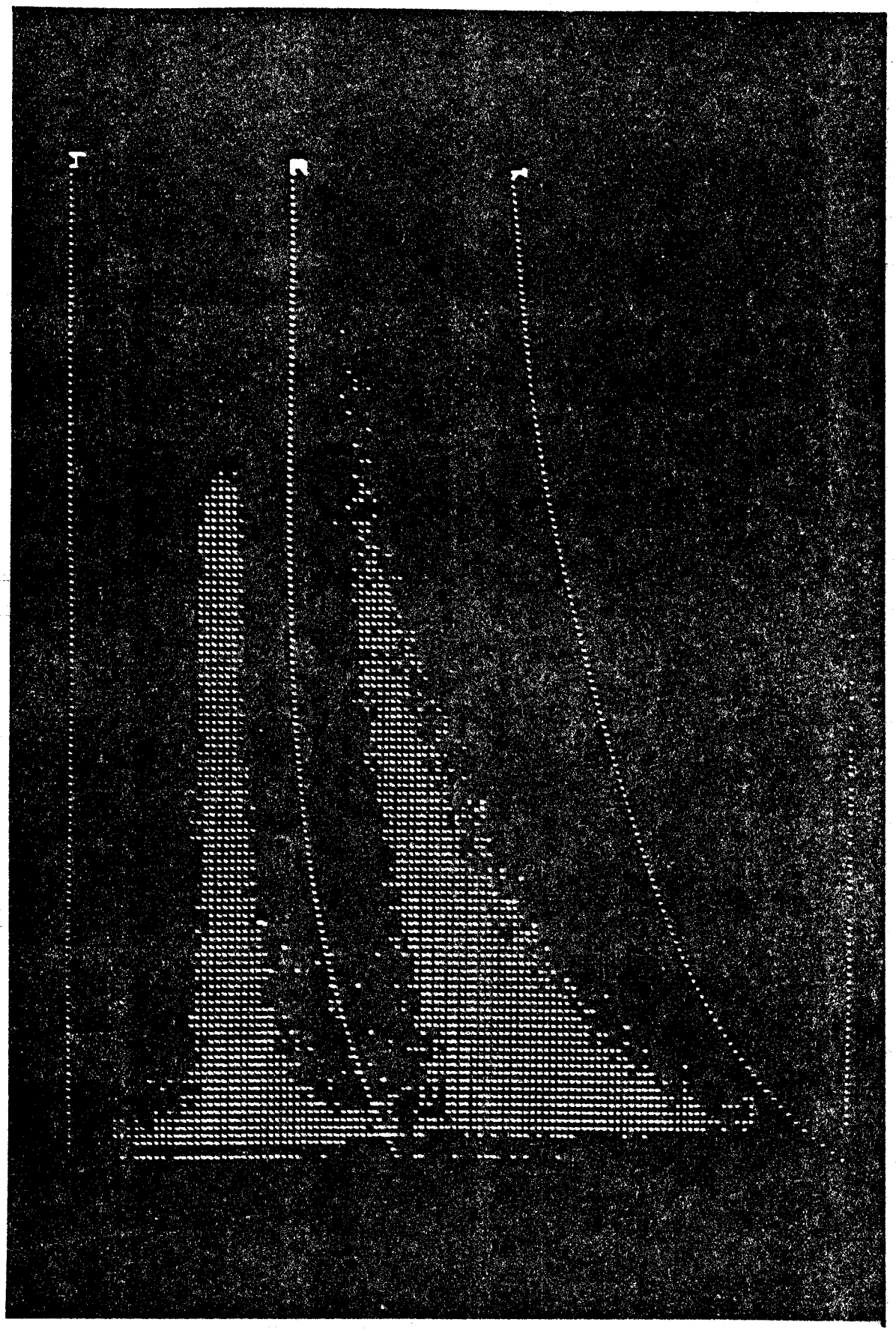

Figure 10. Neutron and Gamma-Ray Bands in the LIGHT-PSD Plane

gammas.

Superimposed neutron and gamma-ray TOF spectra obtained in the Run mode are displayed in Figures 11 through 22. Each figure contains spectra taken at 0°, where the flight paths were generally longer than those employed for scattering angles between 10° and 160°. Since the TOF TAC is started by the neutron detector and stopped by the cyclotron RF, flight time decreases with increasing channel number. Thus, faster neutrons appear to the right as in conventional energy spectra. These TOF spectra have been calibrated at about 0.1 nsec per channel. Thus, the prominent peaks in the gamma-ray spectra, which are due to prompt decays of excited states in the targets, exhibit time resolutions of about $\frac{1}{2}$ nsec (FWHM). Since the system consisting of the neutron detector and associated electronics has measured gamma-ray burst widths of 0.2 nsec, the typical $\frac{1}{2}$-nsec widths are attributed for the most part to the time structure of the incident proton beam pulses.

In the spectra taken with 25-MeV protons on the ^{120}Sn and ^{208}Pb targets, leakage of the target gamma-ray burst into the neutron band is visible. Since the relative amount of gamma-ray "feed-through" is not time correlated, the fraction of gamma-ray counts leaking into any channel of a neutron spectrum may be conveniently estimated by comparing the areas of the target gamma-ray peaks in the

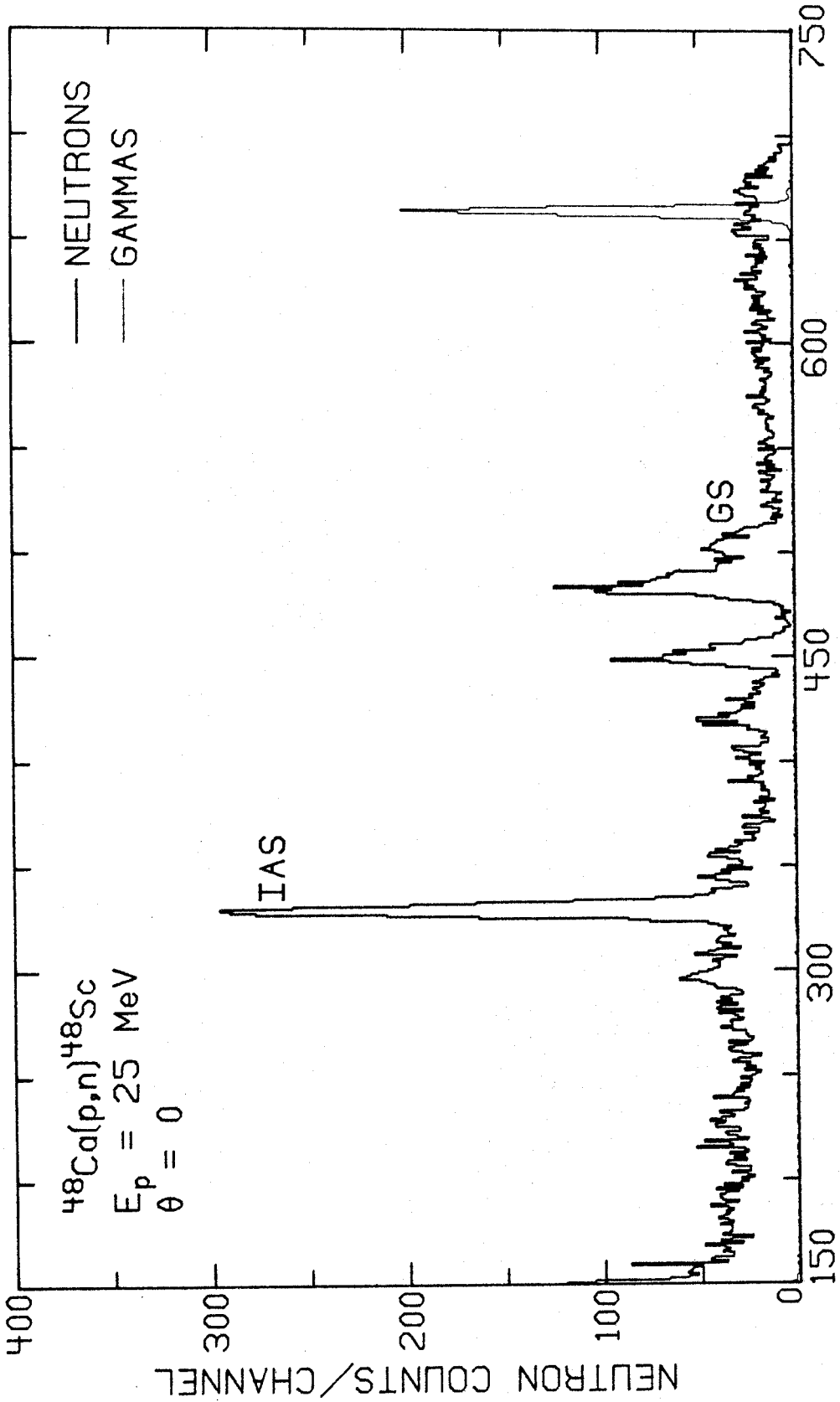

Figure 11. Neutron and Gamma-Ray TOF Spectra at 0^{o} for 25-MeV Protons on ^{48}Ca

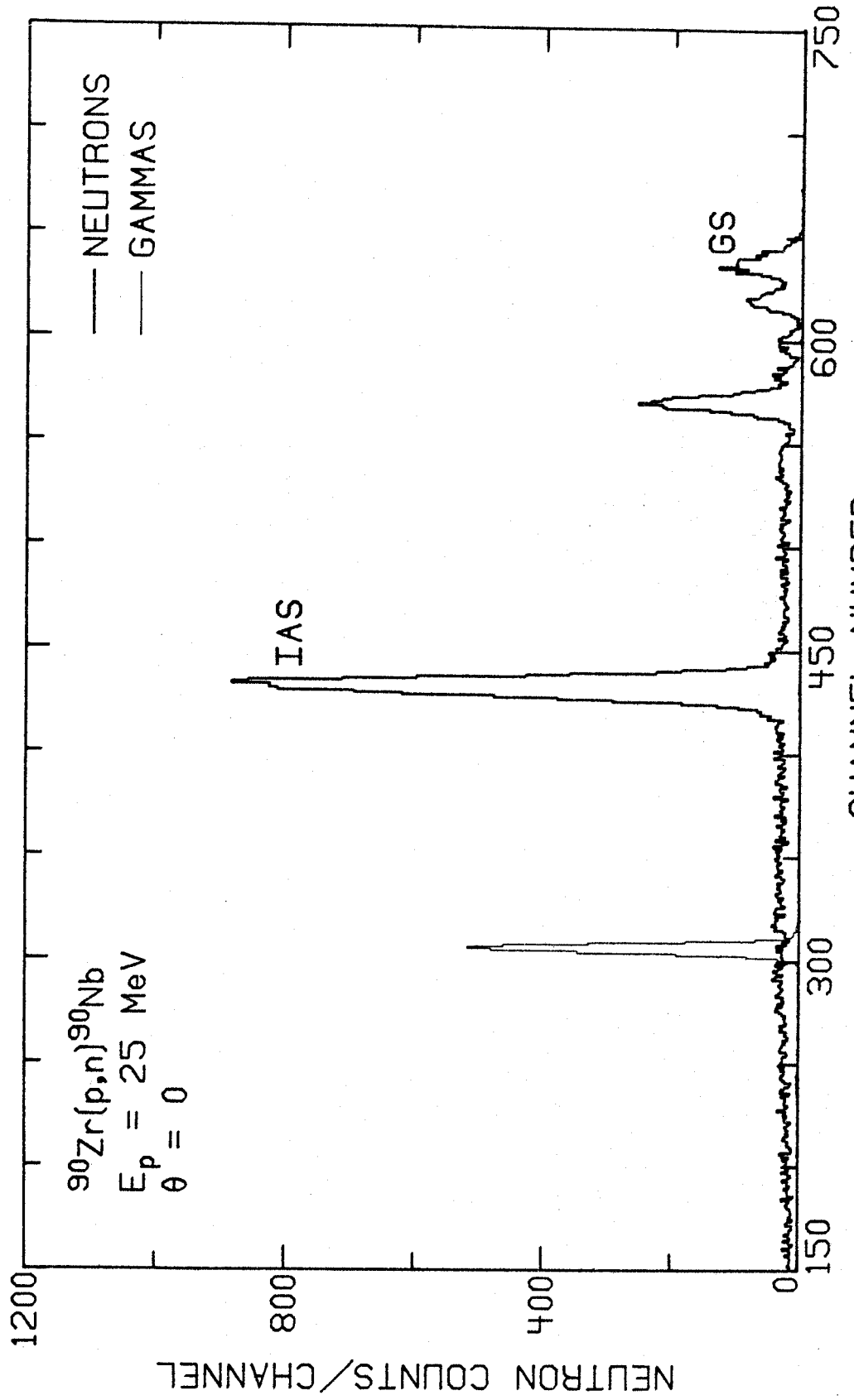

Figure 12. Neutron and Gamma-Ray TOF Spectra at 0° for 25-MeV Protons on ^{90}Zr

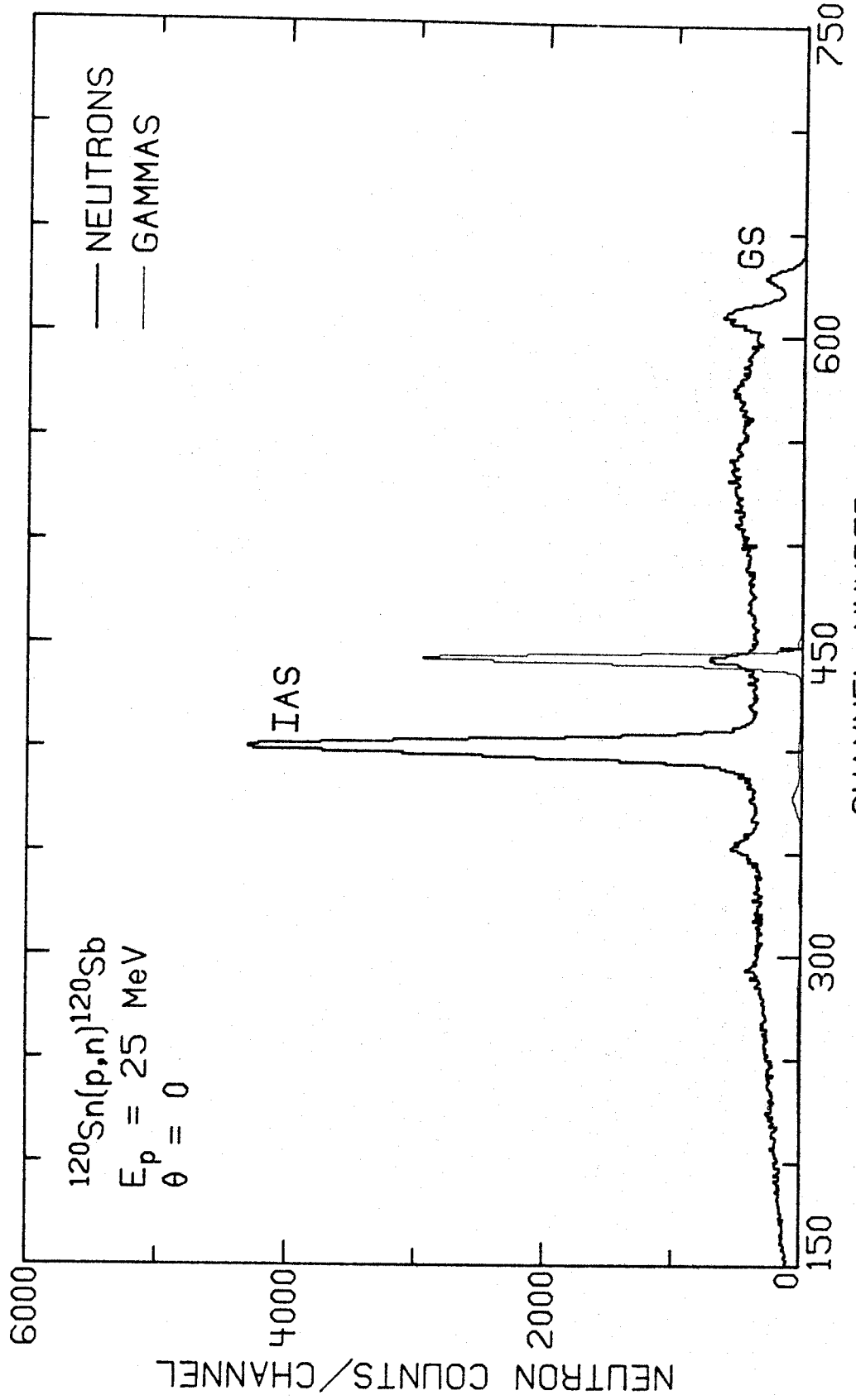

Figure 13. Neutron and Gamma-Ray TOF Spectra at 0° for 25-MeV Protons on ^{120}Sn

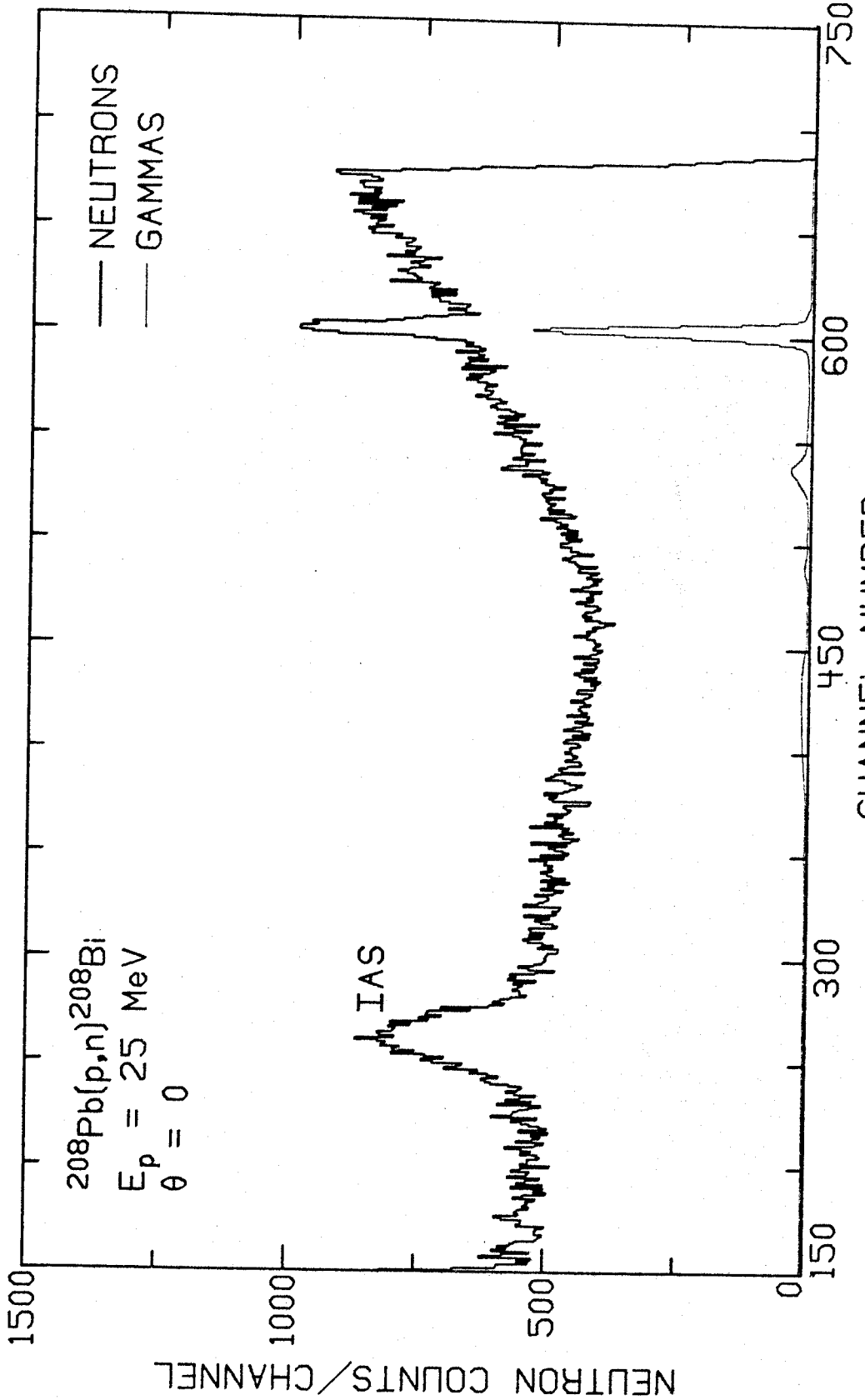

Figure 14. Neutron and Gamma-Ray TOF Spectra at 0^{o} for 25-MeV Protons on ^{208}Pb

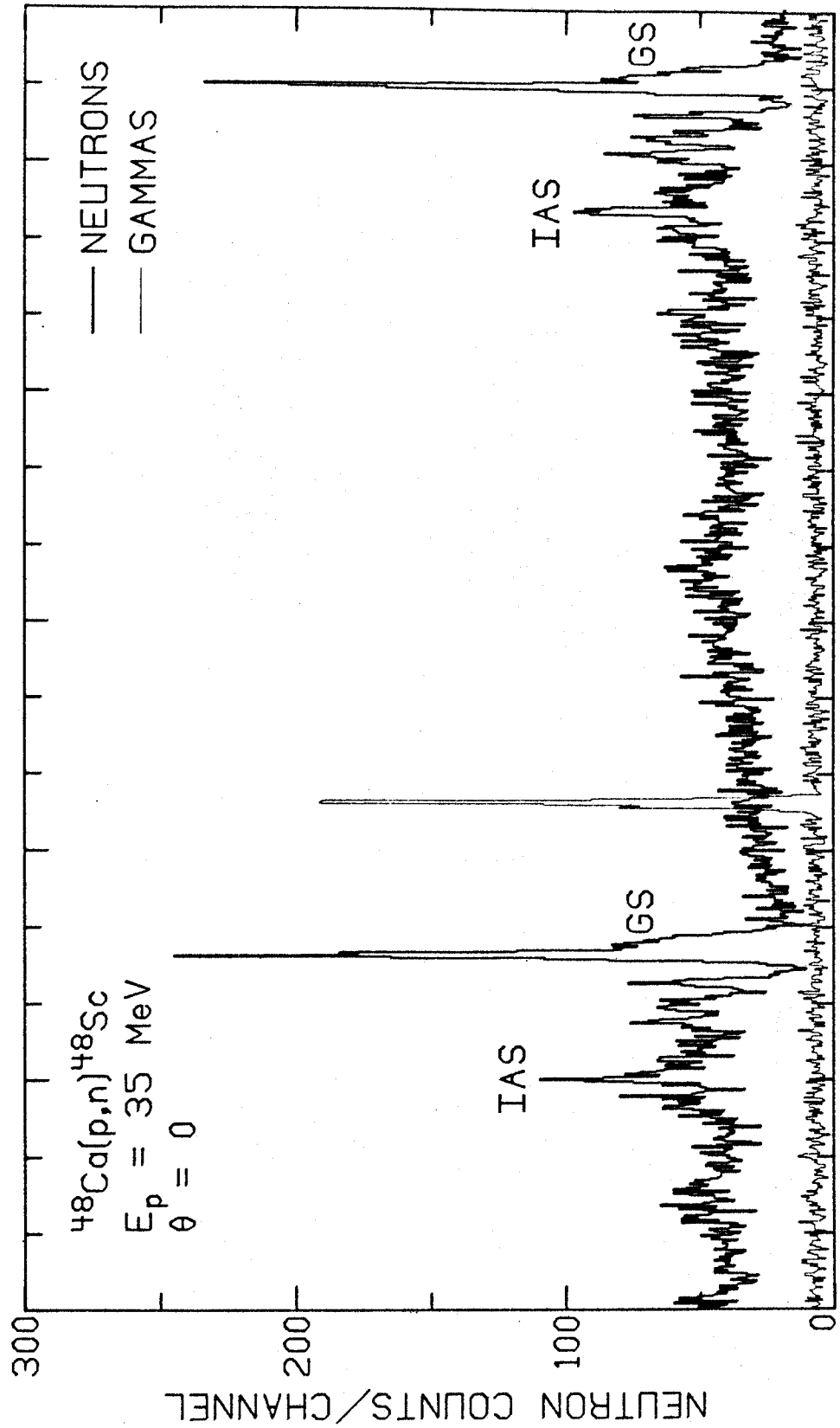

Figure 15. Neutron and Gamma-Ray TOF Spectra at 0° for 35-MeV Protons on ^{48}Ca

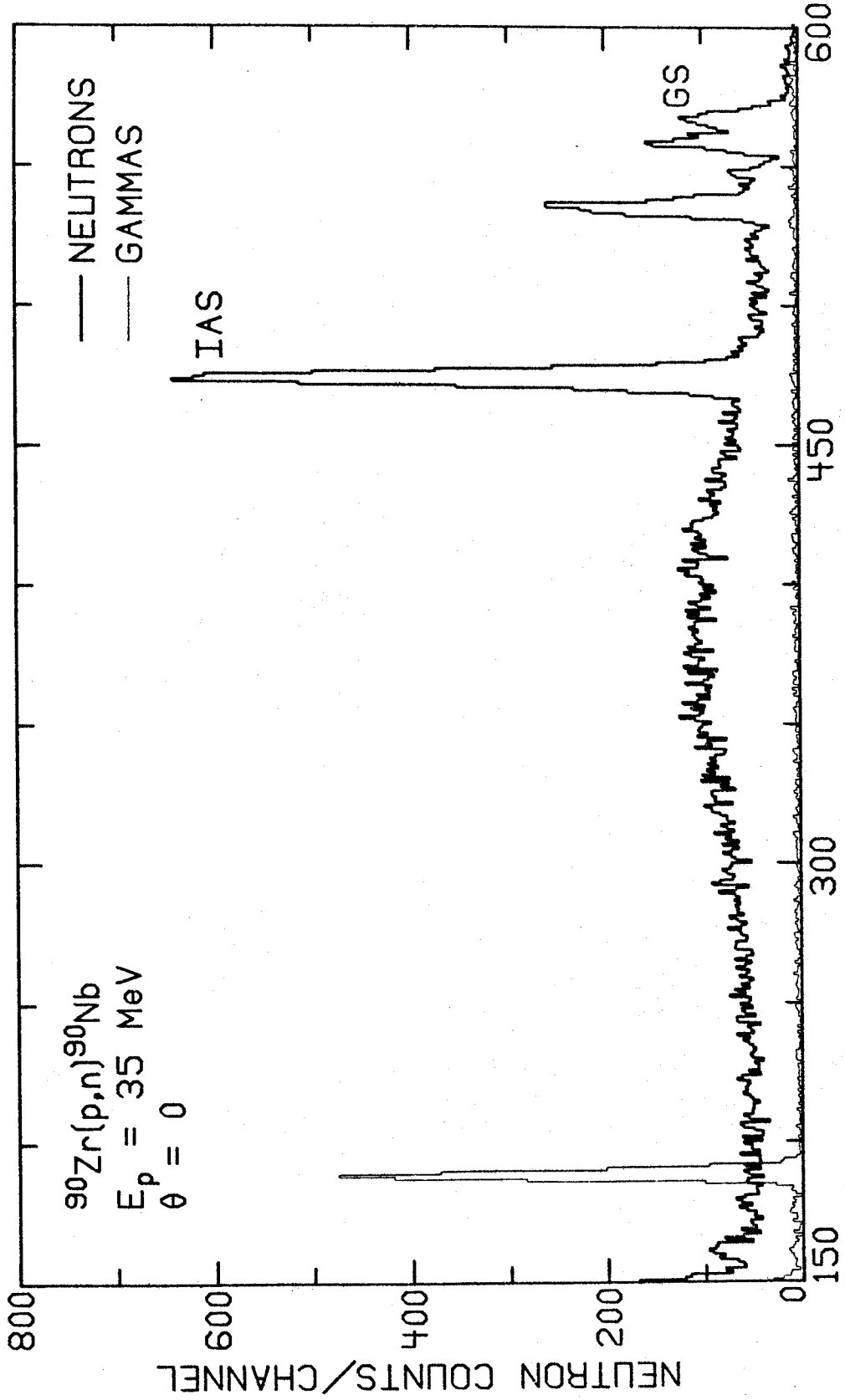

Figure 16. Neutron and Gamma-Ray TOF Spectra at 0° for 35-MeV Protons on ^{90}Zr

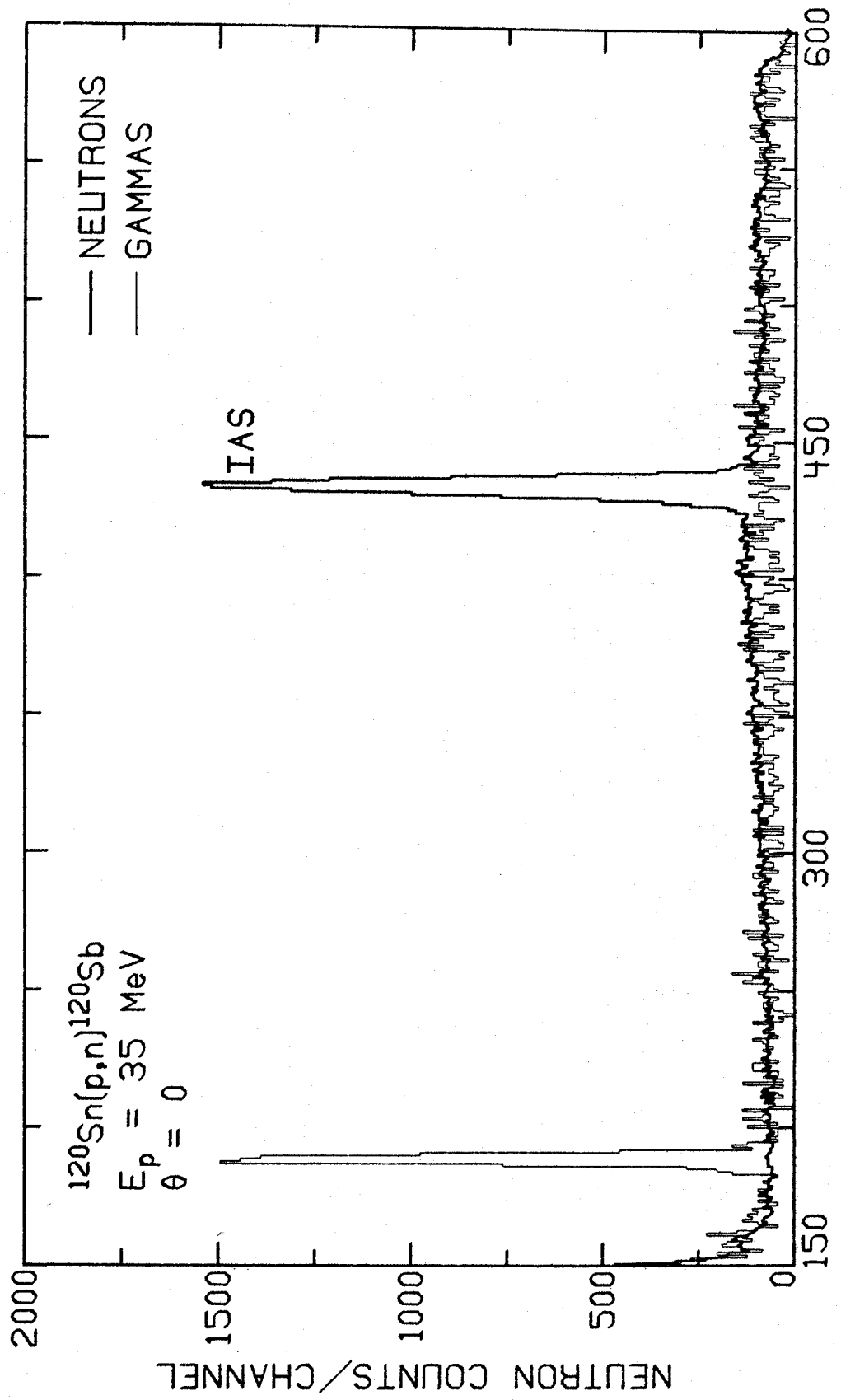

Figure 17. Neutron and Gamma-Ray TOF Spectra at 0° for 35-MeV Protons on ^{120}Sn

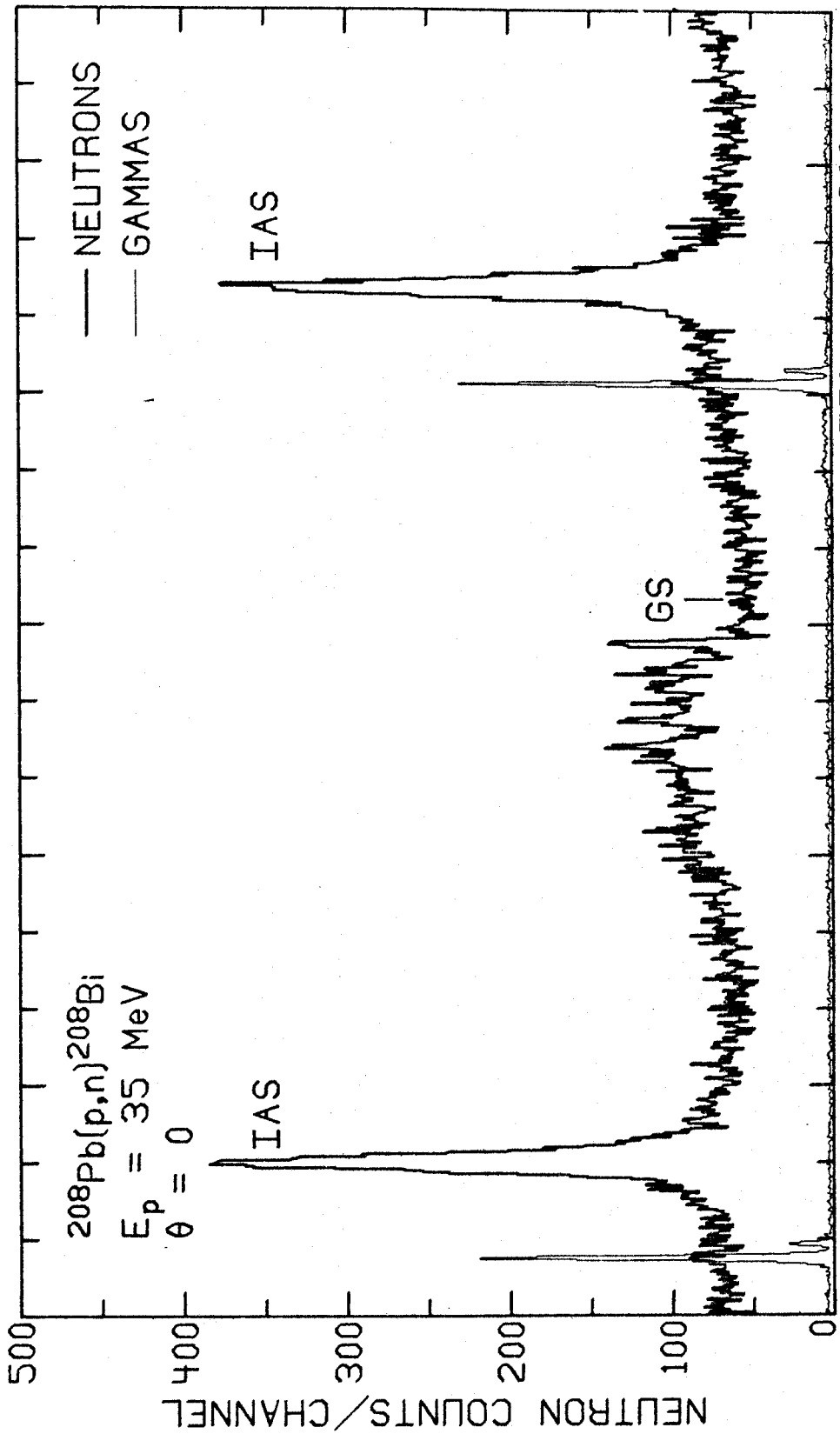

Figure 18. Neutron and Gamma-Ray TOF Spectra at 0° for 35-MeV Protons on ^{208}Pb

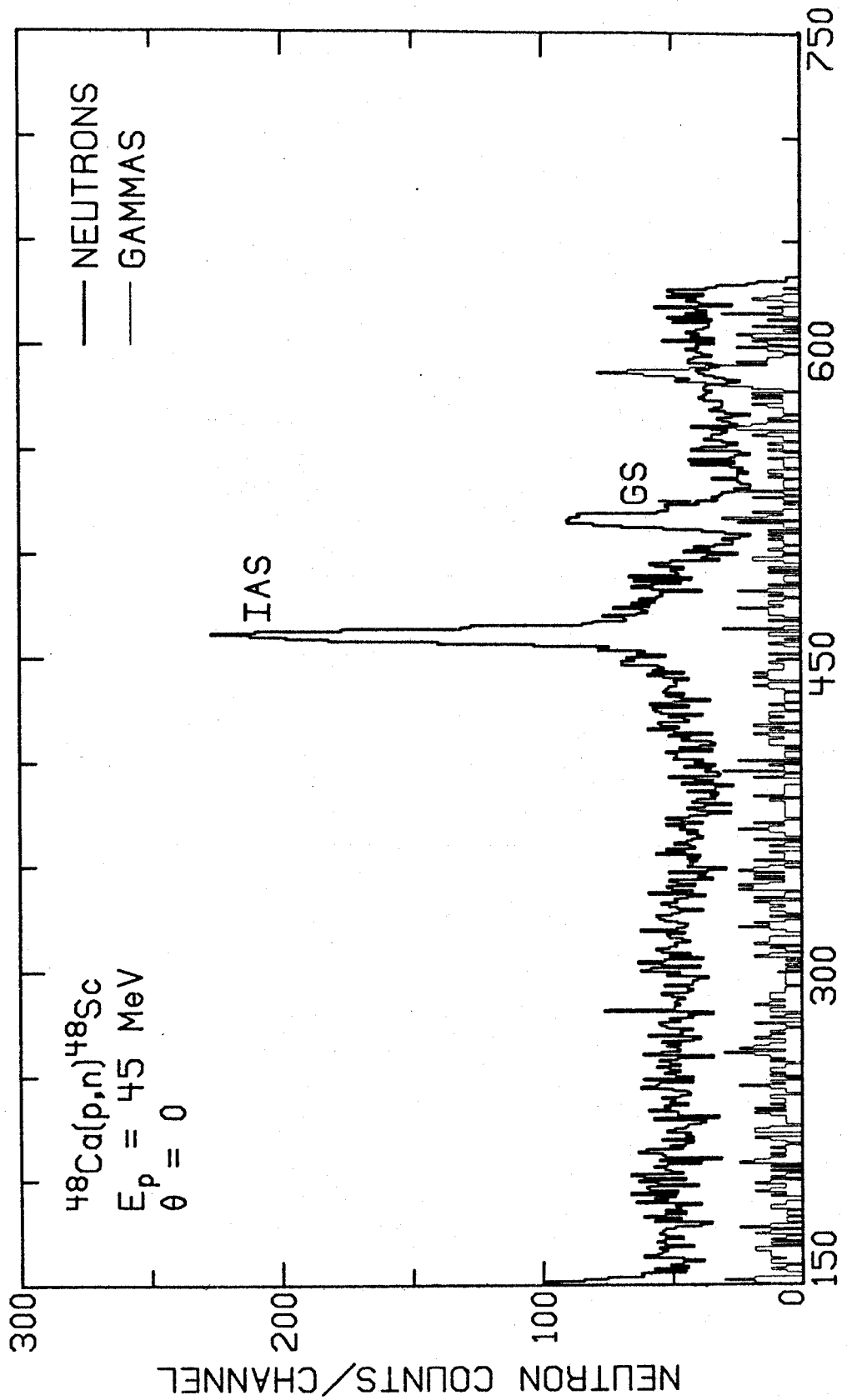

Figure 19. Neutron and Gamma-Ray TOF Spectra at 0° for 45-MeV Protons on ^{48}Ca

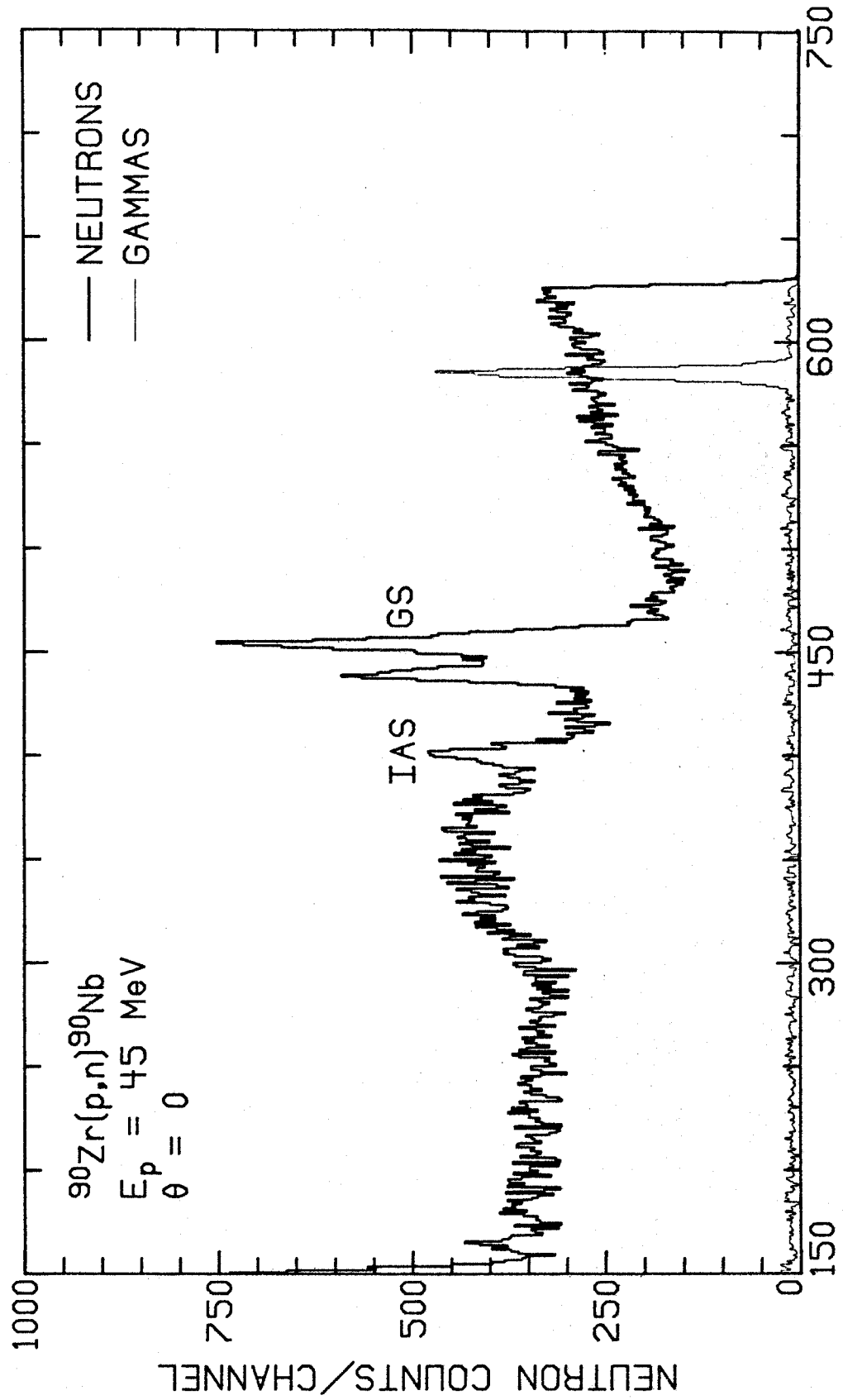

Figure 20. Neutron and Gamma-Ray TOF Spectra at 0° for 45-MeV Protons on ^{90}Zr

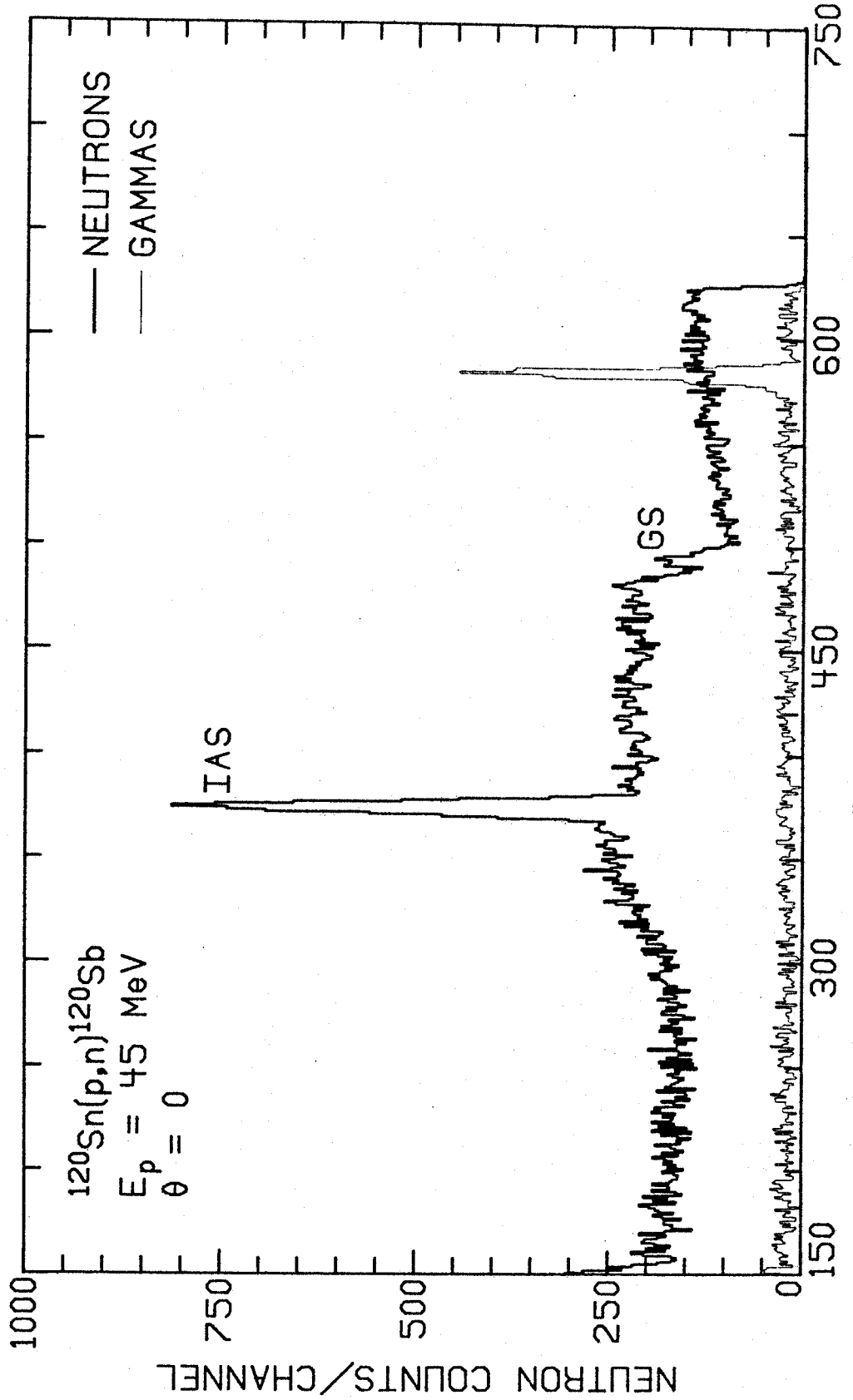

Figure 21. Neutron and Gamma-Ray TOF Spectra at 0° for 45-MeV Protons on ^{120}Sn

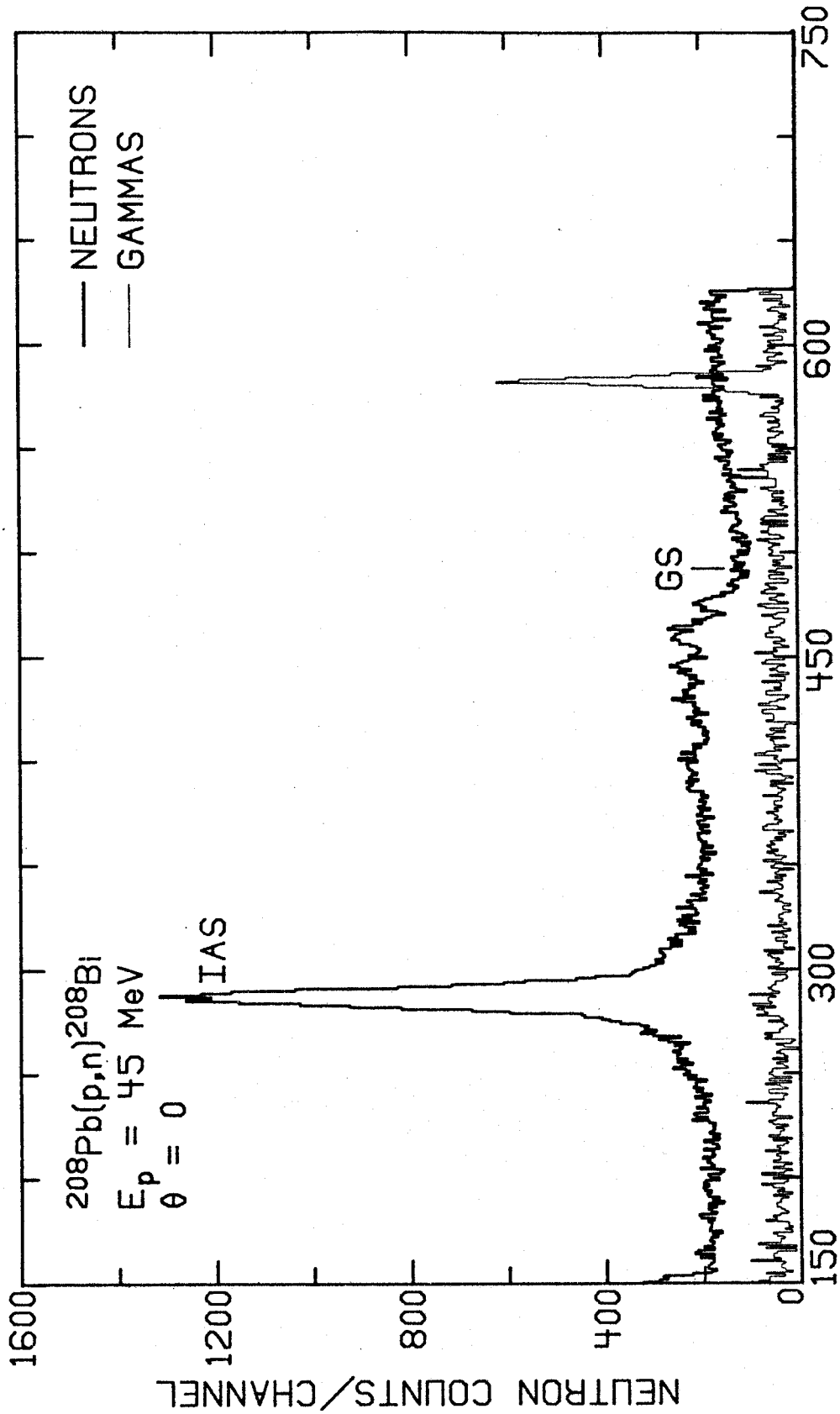

Figure 22. Neutron and Gamma-Ray TOF Spectra at 0° for 45-MeV Protons on ^{208}Pb

neutron and gamma-ray spectra. For the ^{120}Sn and ^{208}Pb targets at 25 MeV, this ratio is approximately 0.01, which is about average for the present experiment. Deviations of more than a factor of two from this value have rarely been observed. This level of discrimination from the PSD system, coupled with the simplicity of the gamma-ray spectra, generally results in only small, flat, gamma-ray contributions to the background under peaks of interest in the neutron spectra. At some scattering angles, additional structure appears in the gamma-ray spectra from protons striking various obstacles along the beam line, especially the graphite aperture at the end of the scattering chamber. Peaks resulting from such localized sources are easily eliminated with lead shielding. The stray protons also produce unwanted sources of neutrons. The aforementioned aperture is followed by graphite tubing with a 3-mm-thick wall which lines the beam pipe through the quadrupole triplet. The natural carbon in the graphite is 98.89% ^{12}C, which has the exceptionally high (p,n) threshold of 19.67 MeV. Thus, protons not transmitted by the triplet mostly produce neutrons with energies less than those from the analogs of target ground states. Neutrons and gamma rays from this potential source of background have also been attenuated with about as many water-filled boxes and lead bricks as the scattering angle would allow.

In some cases, gamma-ray feed-through peaks cannot be conveniently eliminated with shielding. For example, it is impossible to shield against the target gamma-ray burst without also attenuating neutrons of interest. However, it is possible to shift gamma-ray peaks relative to neutron peaks in the TOF spectra by changing the flight path, since the gamma rays are much faster than any of the neutrons. Figures 23 through 25 give arrival time at the detector vs. flight path for IAS neutrons and gamma rays from the targets used in this experiment at proton bombarding energies of 25, 35, and 45 MeV, respectively. These graphs have been useful in selecting flight paths at which gamma rays from the targets would not arrive in coincidence with the neutrons of primary interest. In particular, Figures 24 and 25 indicate that the 4.25-m flight path employed for the angular distributions from 10° to 160° with 35- and 45-MeV protons should keep target gamma-ray bursts at least 4 nsec (40 channels) away from IAS neutrons from any of the targets.

Several factors limit the dynamic range obtainable in the TOF spectra. Since a zero-crossing discriminator sends a stop signal to the TOF TAC once every RF period (T_{RF}), intervals longer than T_{RF} are never converted. Figure 26 gives the recommended operating frequencies of the Michigan State University Cyclotron. The values for proton beams of 25, 35, and 45 MeV correspond to T_{RF}=67.4,

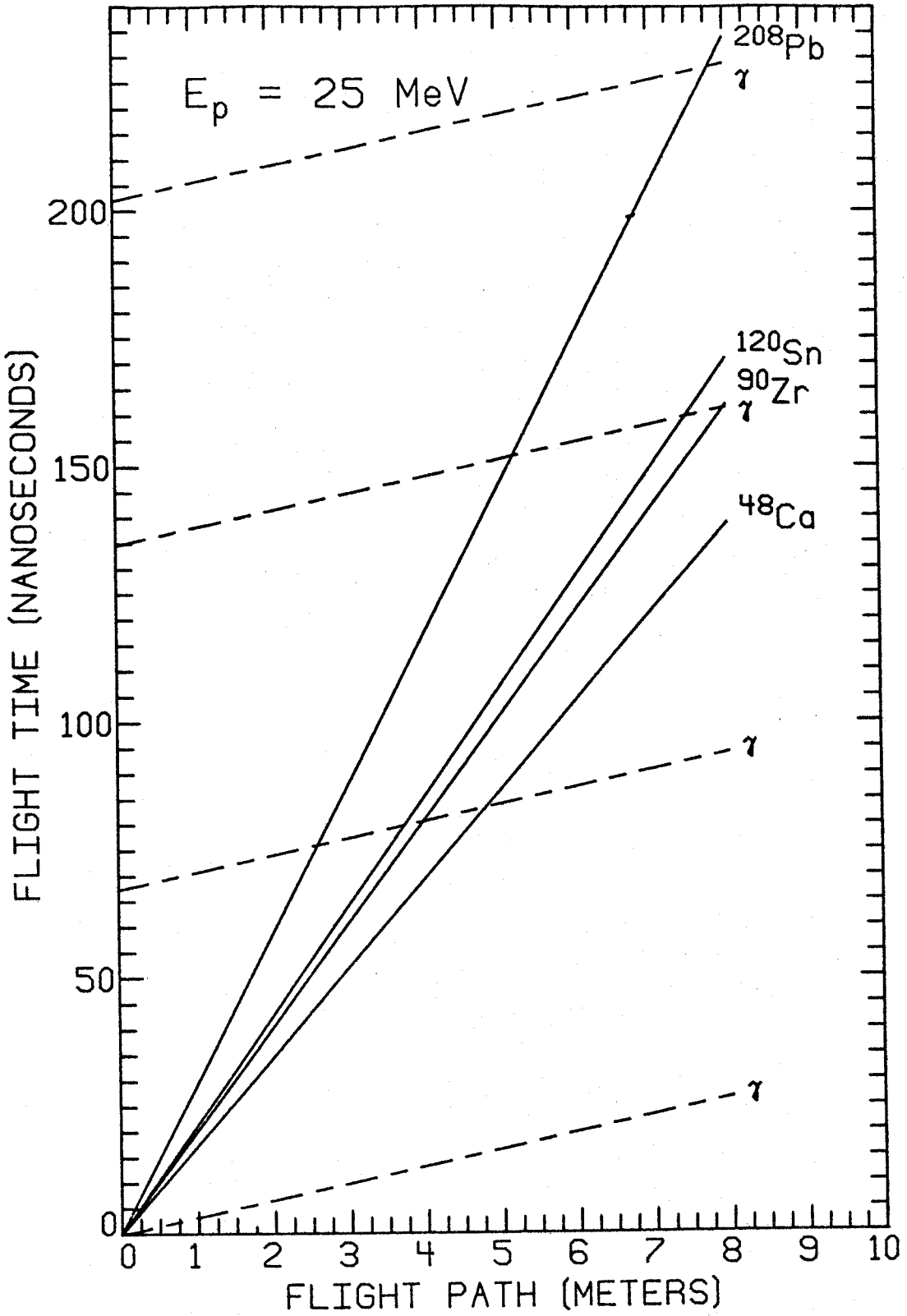

Figure 23. IAS-Neutron and Gamma-Ray Arrival Times for E_p=25 MeV

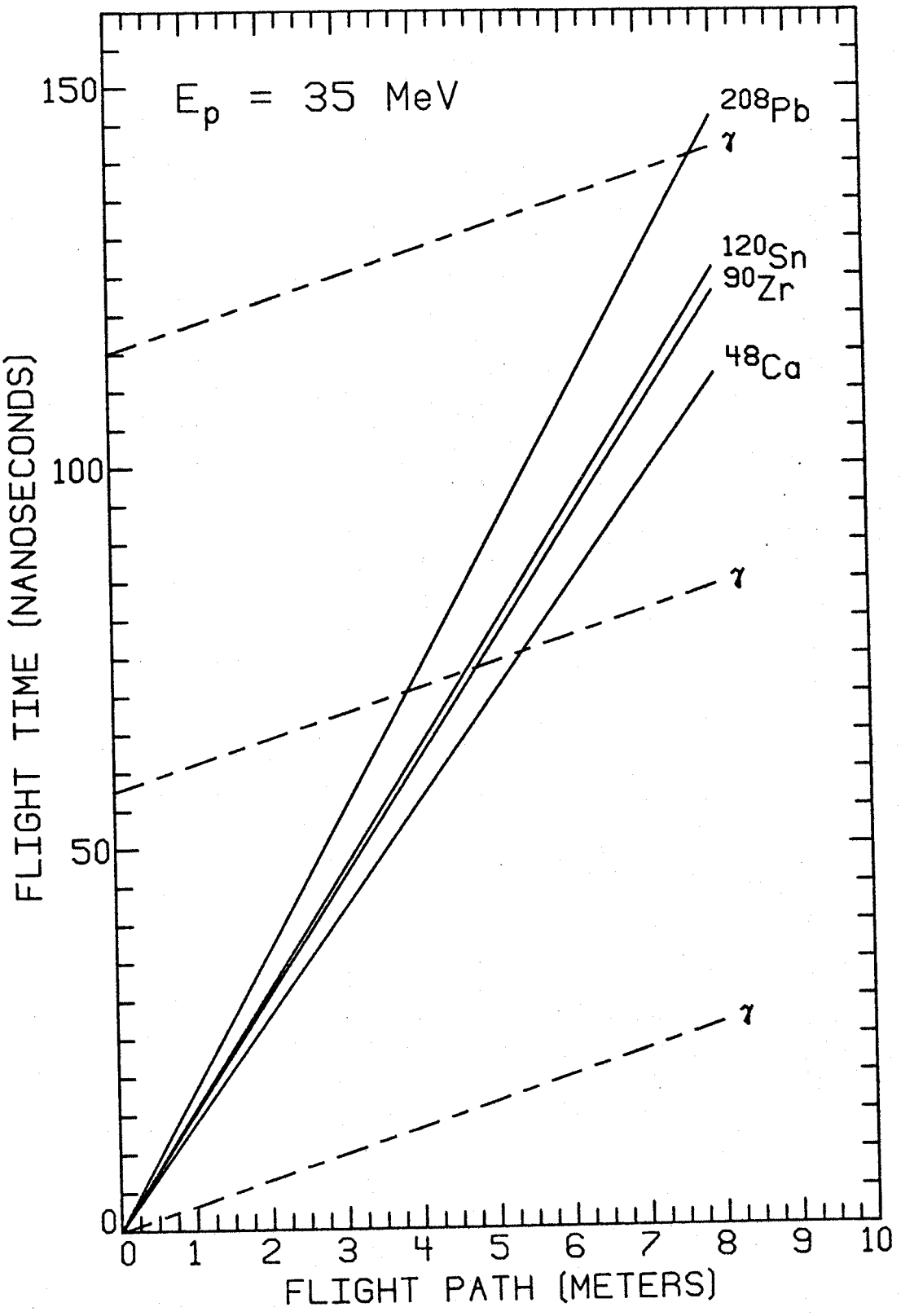

Figure 24. IAS-Neutron and Gamma-Ray Arrival Times for E_p=35 MeV

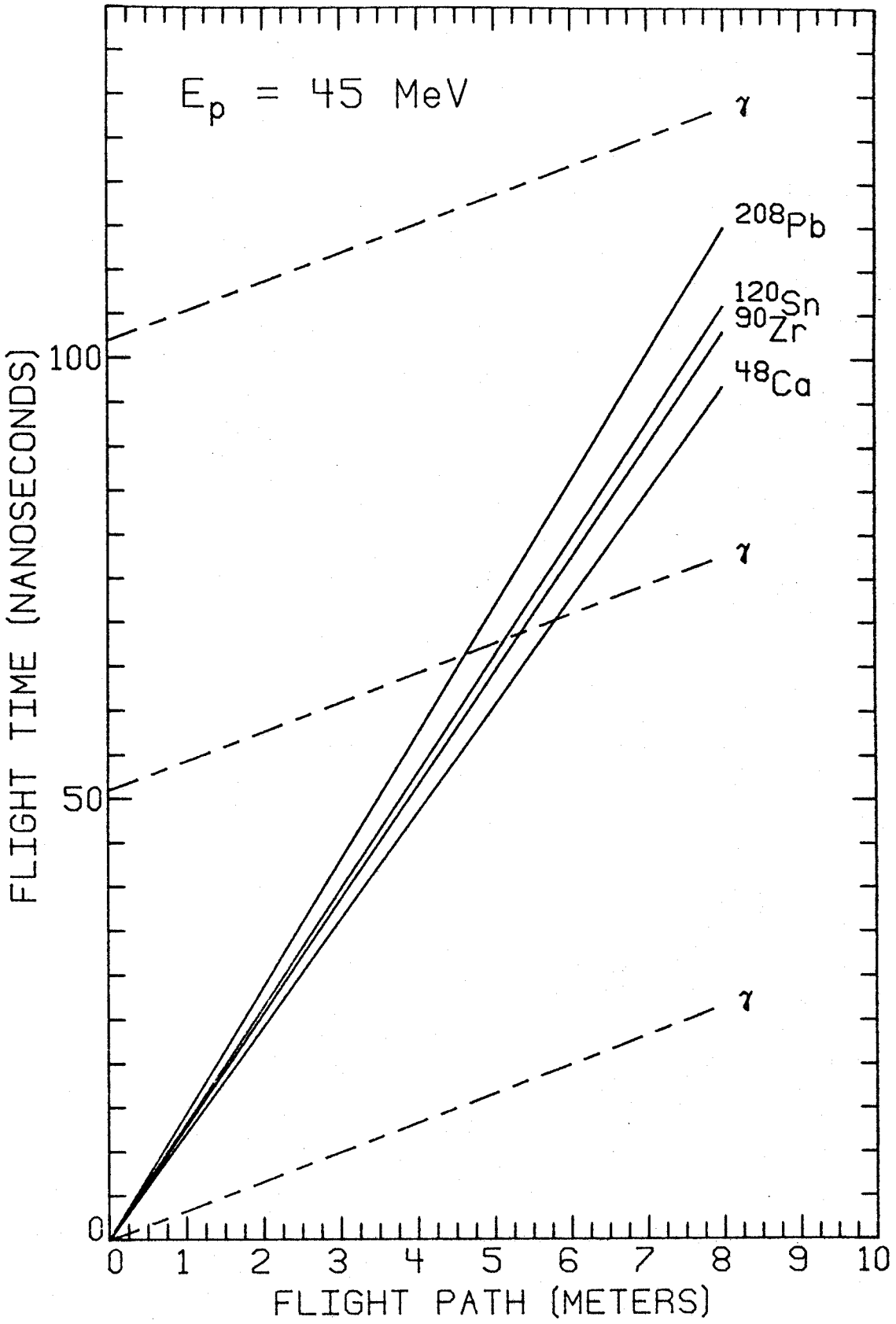

Figure 25. IAS-Neutron and Gamma-Ray Arrival Times for E_p=45 MeV

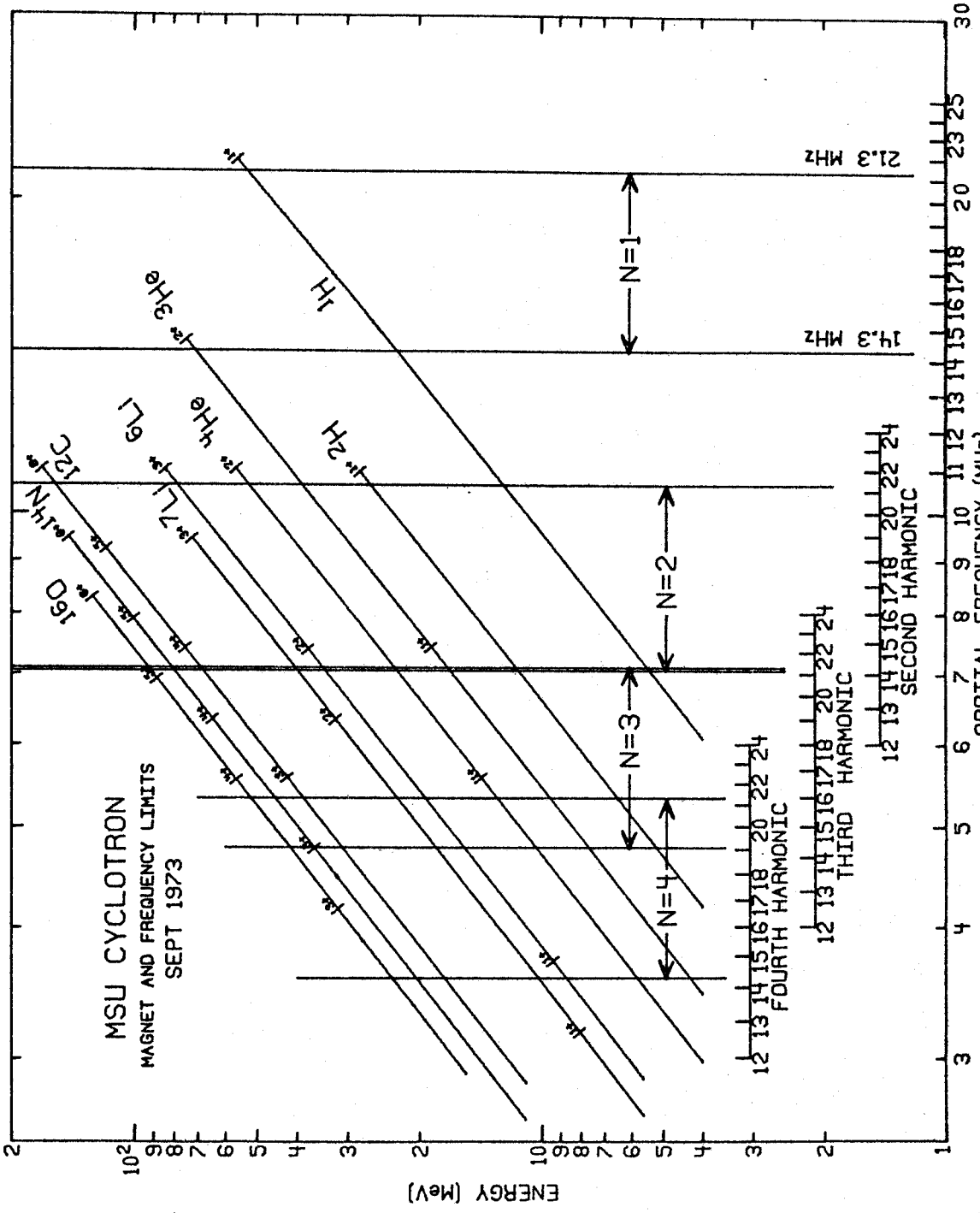

Figure 26. Energy vs. RF for the M.S.U. Cyclotron

57.6, and 51.0 nsec, respectively. Thus, most of the TOF spectra in Figures 11 through 22 cut off abruptly at channel numbers between 500 and 700. Figures 15, 18, and 27 display "doubled" spectra for which this problem has been overcome by eliminating alternate stop signals with a divide-by-two scaler. However, since the proton beam bursts remain separated by T_{RF}, channel numbers still only correspond to flight times modulo T_{RF}. For all practical purposes, this ambiguity may be removed by raising the threshold on the TSCA to discriminate against slow neutrons from a given beam burst which are caught by the fastest neutrons from the following burst. The TSCA threshold for Figure 27 corresponds to a neutron energy of about 6 MeV. With this level, the neutron spectrum is sufficiently suppressed at high excitation in the residual nucleus to avoid overlap with the ground state. If a larger dynamic range is desired, it may only be obtained by eliminating all but one beam burst out of every N in succession. This technique is currently implemented with an external beam deflection system known as the "beam sweeper." Unfortunately, throwing away beam bursts reduces the current on target. Raising the TSCA threshold also cuts down the counting rate, even for high-energy neutrons, since neutrons of a given energy are potentially detectable via faint scintillations induced by recoil protons with much lower energies. Thus, it is generally necessary

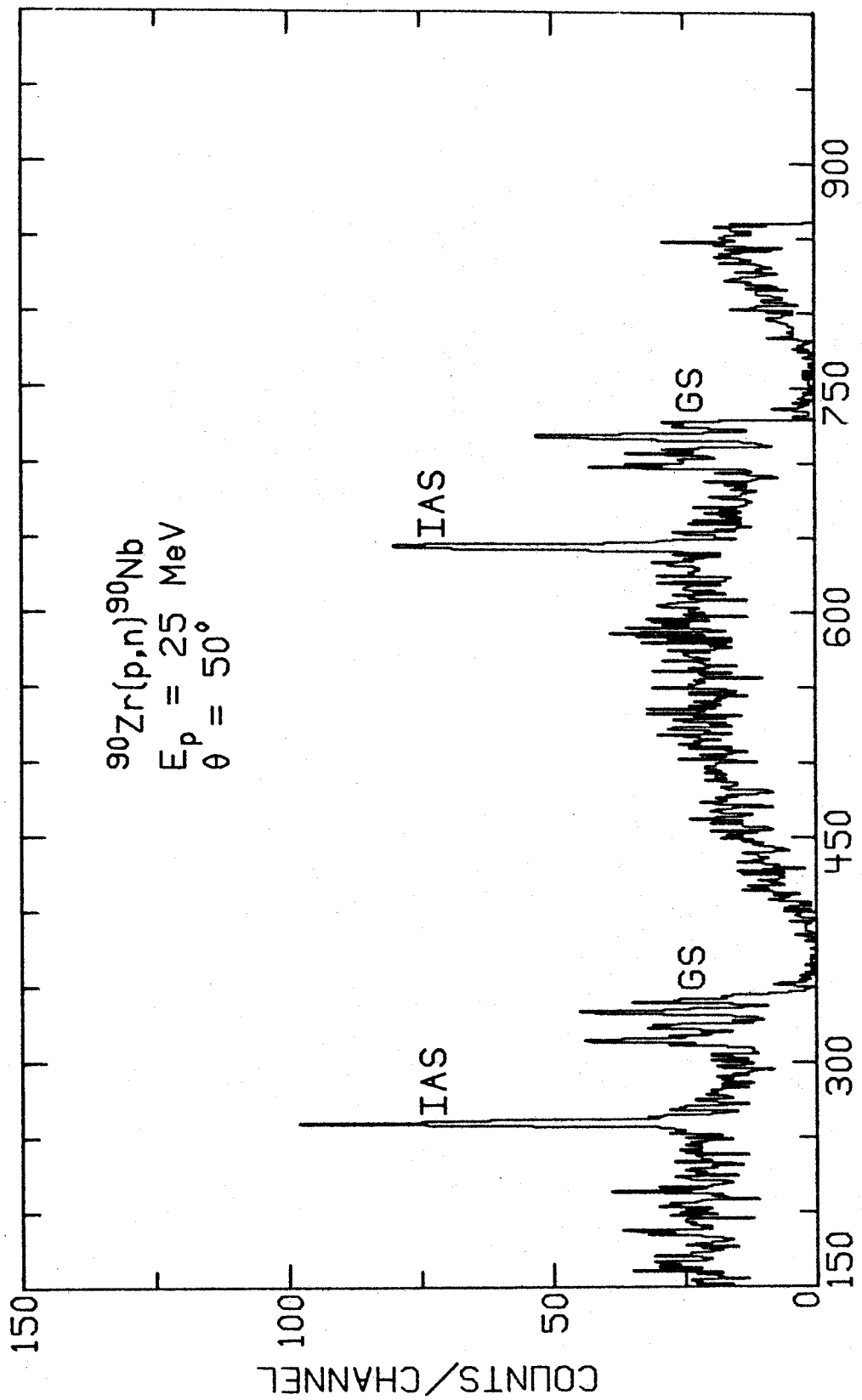

Figure 27. Doubled Neutron-TOF Spectrum

to sacrifice efficiency for dynamic range. Only IAS neutrons are of primary interest in the present experiment. Therefore, the TSCA threshold has always been set to give essentially zero detection efficiency for the low-energy neutrons from a given beam burst which would overlap with IAS neutrons from the next burst. In most cases, even the ground state of the residual nucleus has been relatively free from low-energy overlap. With the flight paths available for the present experiment, this technique has resulted in greater counting rates for the IAS neutrons than would have been obtained through preventing overlap to a comparable extent by using the beam sweeper and lowering the TSCA threshold. An additional advantage of the higher threshold is improved PSD performance, since the small-amplitude light pulses from protons and electrons are difficult to distinguish. However, if increasingly longer flight paths were employed, the beam sweeper would eventually become a necessary component of the TOF system.

Except for the analog of ^{48}Ca, every IAS observed in this experiment is proton unbound. In such cases, the IAS generally appears as an isolated peak on a relatively smooth continuum. Occasionally, the analog of an excited state of the target also emerges. The most prominent example of this in the present data is the analog of the first excited state of ^{120}Sn, which is visible in Figure 13. This $T_>$ state is also the closest to the analog of

the ground state of any target in this experiment. The separation in this case is 1.17 MeV, which represents a reasonable upper limit on the allowed energy resolution. Within such limits, achieving a particular resolution is not usually critical for observing the proton-unbound analog states. In contrast, the IAS of ^{48}Ca lies amidst a dense, fluctuating spectrum of $T_<$ excitations, which enhances the desirability of obtaining the best possible resolution.

Most of the neutron peaks in the TOF spectra have time spreads between 0.6 and 1.0 nsec (FWHM). The exceptions are almost entirely for back-angle spectra, where timing drifts have not always remained insignificant during runs lasting up to two hours, and the IAS of ^{208}Pb, which has an intrinsic width of about 200 KeV (Cr 72). Non-relativistically, the energy resolution obtained for neutrons with the TOF technique is given by

$$\Delta E = 27.7 \frac{E^{3/2}}{S} \Delta T \text{ KeV}, \qquad \text{(II-1)}$$

where E is the neutron energy in MeV, S is the flight path in meters, and ΔT is the time resolution in nanoseconds. Figure 28 displays ΔE vs. E for typical spectra obtained in this experiment. For this graph, ΔT and S have been fixed at 0.8 nsec and 4.25 m, respectively. This flight path has been used for all of the spectra taken from 10° to 160° with 35- and 45-MeV protons. At 25 MeV, this range

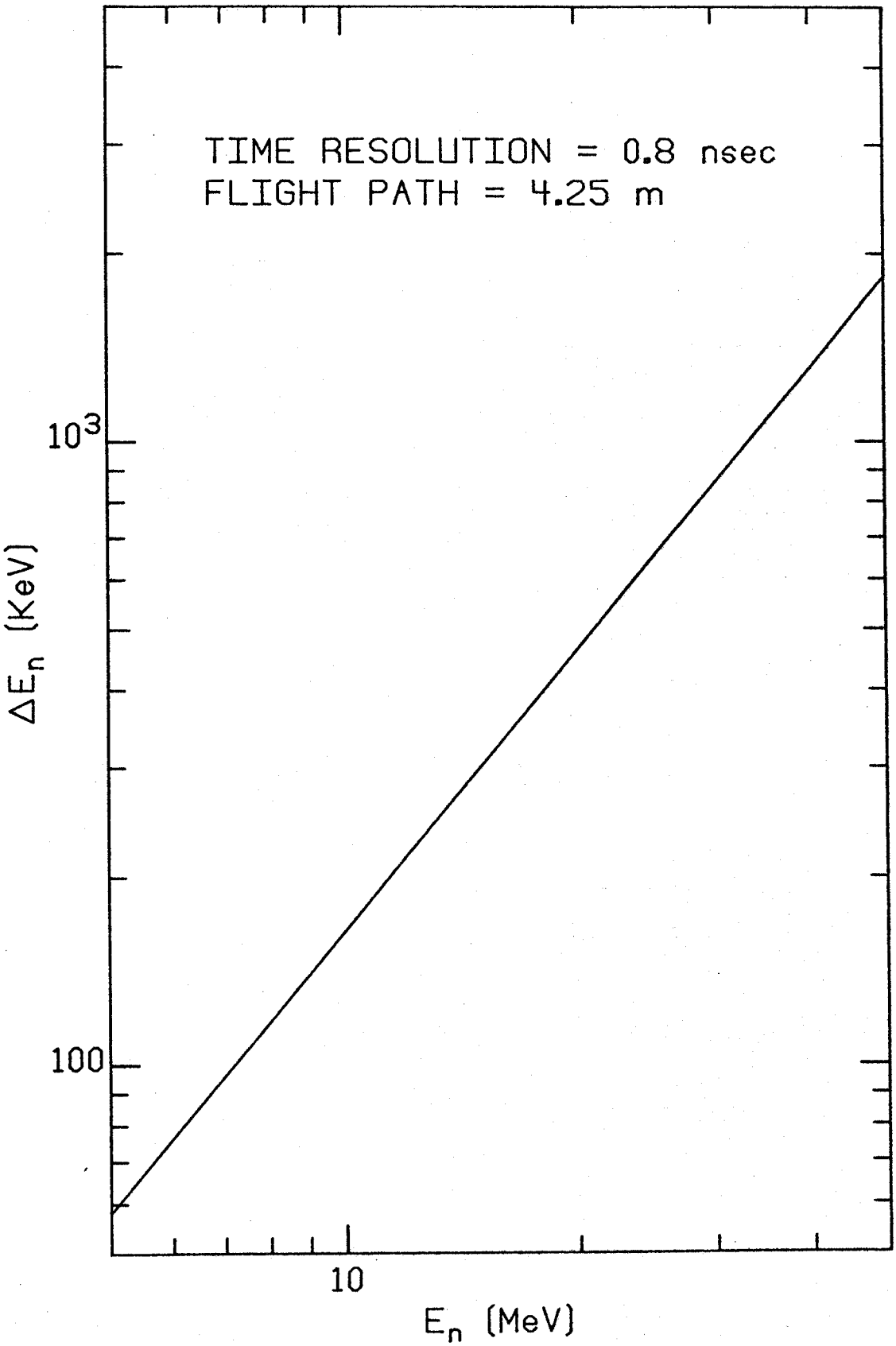

Figure 28. Typical Neutron-Energy Resolution

of the angular distributions for the ^{48}Ca, ^{90}Zr, ^{120}Sn, and ^{208}Pb targets has been obtained with S=4.01, 4.59, 4.63, and 3.02 m, respectively. The 0° spectra in Figures 11 through 22 have mostly been taken at a flight path of 7.22 m. Thus, they generally exhibit about the best energy resolution for each reaction and bombarding energy in the present experiment. For example, the IAS of ^{90}Zr in Figure 12 has an observed width of approximately 180 KeV (FWHM), even though the target thickness contributes an energy spread in excess of 100 KeV.

2. Monitor Spectra

The digitized amplitudes of signals from the monitor detector are stored in a 1024-channel array in the memory of the Sigma 7 computer with the data-acquisition code POLYPHEMUS (Au 70). One of the resulting proton energy spectra for $^{120}Sn(p,p')$ at a bombarding energy of 45 MeV is shown in Figure 29. This example displays the most difficult case in the present experiment for resolving the elastically scattered protons. The first excited state of ^{120}Sn is only 1.17 MeV above the ground state. The corresponding peaks in Figure 29 are 14 channels apart, which gives a calibration of 83.6 KeV/channel. The energy resolution in this spectrum is about 660 KeV, which is adequate for extracting the number of elastically scattered protons with a peak-fitting program (St 73).

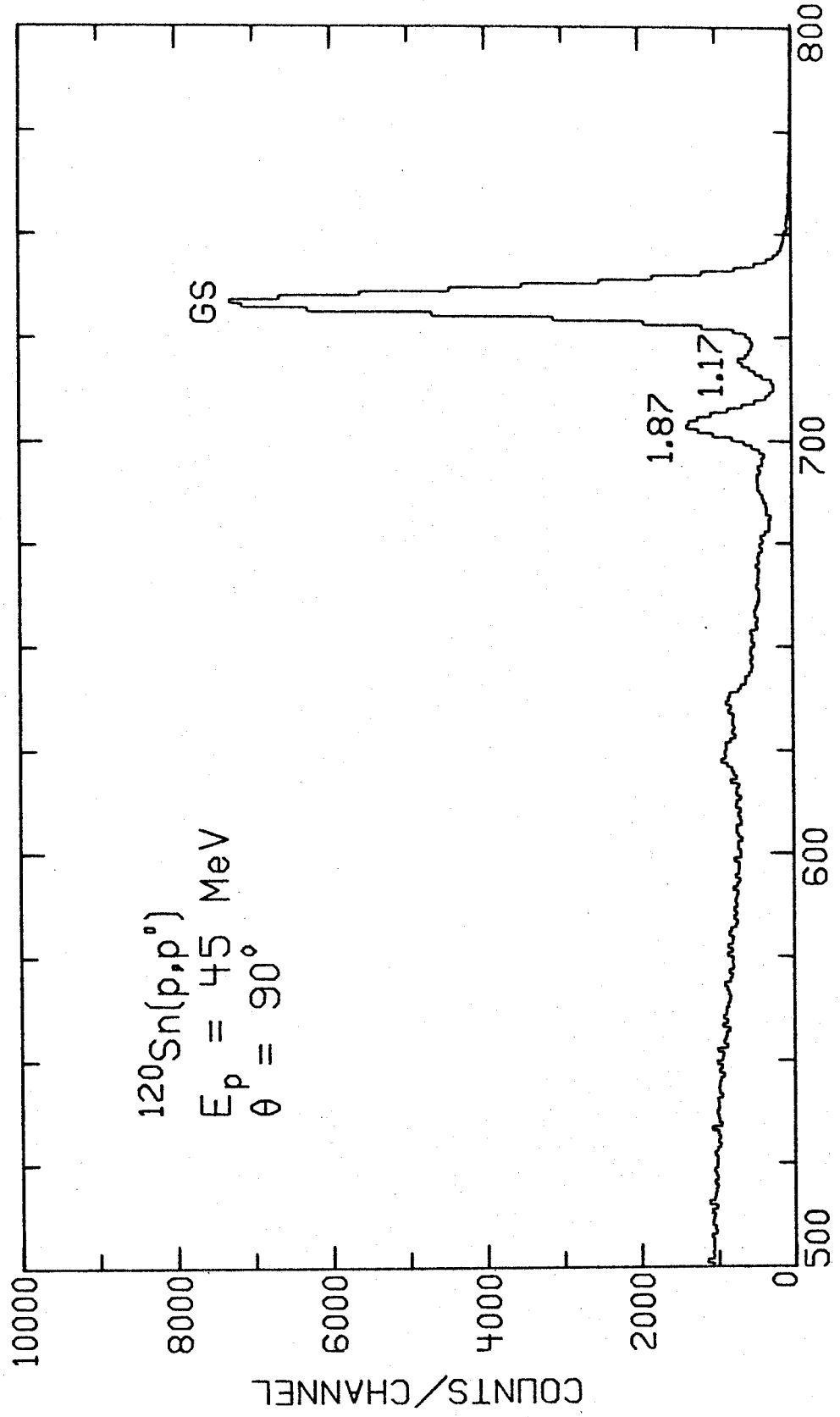

Figure 29. Proton-Monitor Spectrum Resolving the 1.87-MeV, 1.17-MeV, and Ground States of ^{120}Sn at E_p=45 MeV

3. Charge Collection

Compared to the best charged-particle detectors, the present neutron TOF system affords poor energy resolution and detection efficiency. Thus, relatively thick targets (about 10 mg/cm^2) have been used in this experiment to compensate for the lack of efficiency with little sacrifice of resolution. Another difference with typical charged-particle experiments is the relatively large distance between the target location and the beam dump, which reduces the neutron background from the dump for most scattering angles. Unfortunately, the thick targets scatter a lot of the beam, making charge collection in the distant Faraday cup incomplete. The quadrupole triplet following the scattering chamber refocusses much of the scattered beam into the dump Faraday cup, but the acceptance of the magnetic lens is limited (see Section II.A.2). For the worst case in this experiment, 45-MeV protons incident on a 30-mg/cm^2 ^{208}Pb target, multiple-scattering calculations indicate that almost 20% of the beam would not be transmitted to the dump. Therefore, a secondary Faraday cup has been created by insulating the beam pipe between the scattering chamber and the dump. From the target, it subtends 0.050 radians out from the beam-pipe axis, which is approximately twice the angular acceptance of the quadrupole triplet. At 50 milliradians, single Rutherford scattering is more than an order of magnitude

more probable than multiple scattering of 45-MeV protons from the 30 mg/cm^2 ^{208}Pb target. Even for this extreme case, less than 2% of the beam is scattered beyond the acceptance of the total charge-collection system. Current from the beam-dump Faraday cup is integrated and scaled with an Ortec 439 Current Digitizer coupled to a Tennelec TC 555P Dual Counter/Timer. The same functions are performed for current from the beam-pipe Faraday cup with an Elcor A310B Current Indicator and Integrator.

4. Dead-Time Measurement

Several components of the TOF system have processing times for electronic signals during which they are unresponsive to additional input. The data-acquisition code TOOTSIE and the TOF TAC have minimum processing times of approximately 60 and 5 microseconds, respectively, which introduce the only significant dead times into this experiment. The fraction of input signals converted by the TOF TAC is measured directly by counting positive logic signals from the time-pickoff control and the true-start output of the TAC with Ortec 430 Scalers. Similarly, the ratio of events stored with TOOTSIE to the number input is given by the quotient of the charge counts recorded in the Channel-Zero register of TOOTSIE and the beam-dump scaler.

During this experiment, the CFPHT-circuit triggering rate was monitored by an Ortec 441 Ratemeter and

maintained at less than 10 kHz, which kept the total dead time of the system under 15%.

F. Data Reduction

1. Spectrum Calibration

To calibrate a TOF spectrum, it is necessary to ascertain the time interval per channel (T_C) and the flight time corresponding to channel number 0 (T_0). T_C is conveniently determined by taking a doubled spectrum and dividing the interval between successive gamma-ray bursts from the target by the cyclotron RF period. The result is input to the spectrum-calibration and peak-fitting code ANNIE (Do 73), along with TOF spectra and additional data acquired from a subsequent series of runs.

The program first performs a non-linear least-squares fit to the gamma-ray burst from the target with the function

$$F(T) = \tfrac{1}{2}A(\mathrm{erf}(T_+) - \mathrm{erf}(T_-))/D_T + B, \qquad \text{(II-2)}$$

where

$$T_\pm = 2^{-\frac{1}{2}}(S/C - T \pm \tfrac{1}{2}D_T)/S_G,$$

$$T = T_{G0} - T_C I,$$

$$D_T = (n-1)D_S/C,$$

$$B = B_0 + B_1(I-I_0) + B_2(I-I_0)^2,$$

C is the speed of light in vacuum, I is channel number in the gamma-ray TOF spectrum, I_0 is the center of the fit interval, and n and D_S are the refractive index and thickness of the scintillator, respectively. Apart from the quadratic background (B), this function is the convolution of a Gaussian time distribution representing electronic plus beam-pulse time spread with a rectangular distribution resulting from the speed difference between gamma radiation and visible light in the scintillator. The refractive index of NE 213 is 1.508. Thus, light pulses from molecular de-excitation traverse the scintillator only about 2/3 as fast as incident gamma rays. The search parameters are the area (A) and standard deviation (S_G) of the Gaussian distribution, the gamma-ray flight time corresponding to channel number 0 (T_{G0}), and the average magnitude (B_0), slope (B_1), and curvature (B_2) of the background.

In general, the neutron flight time for channel number 0 is given by

$$T_{N0} = T_{G0} + NT_{RF}, \qquad \text{(II-3)}$$

where N is the number of RF periods between beam bursts responsible for simultaneously observed neutrons and gamma rays from the target. Thus, the neutron flight time

corresponding to channel number I is given by

$$T_N = T_{N0} - T_C I. \qquad \text{(II-4)}$$

The relativistic relationship between flight time (T) and kinetic energy (E) is

$$T = S(1 - (1 + E/E_0)^{-2})^{-\frac{1}{2}}/C \qquad \text{(II-5)}$$

for a particle with rest energy E_0. This is evaluated for neutrons from the IAS of the target, and the result is compared with flight times calculated with Equations II-3 and II-4 for the minimum and maximum channel numbers of interest and increasing values of N. Thus, for some N, the T_{N0} which calibrates the neutron TOF spectrum for the appropriate range of flight times is determined. Finally, the calibration is converted from flight time to neutron energy with

$$E = E_0((1 - (S/(CT))^2)^{-\frac{1}{2}} - 1), \qquad \text{(II-6)}$$

which is an inverted form of Equation II-5.

The program also calibrates the gamma-ray TOF spectrum in terms of distance along the beam line to potential sources arising from protons striking the pipe. This is often a useful diagnostic for aligning the beam or placing local shielding.

2. Peak Fitting

In addition to calibration, ANNIE is used for extracting the areas, widths, and centroids of peaks in the neutron TOF spectra. As for the gamma-ray fit, the search routine CURFIT (Be 69A) is employed to vary a parameterized peak-plus-background function until the quantity defined by

$$\chi^2 = \sum_{i=1}^{N} (Y_i - F_i)^2/Y_i \qquad \text{(II-7)}$$

is minimized to the extent of not changing by more than a specified convergence criterion between successive iterations of the search. In this definition, i labels the channels within the selected interval where the experimental yield per channel (Y_i) is to be fit with the theoretical function (F_i). CURFIT is based on a very efficient algorithm (Ma 63) which essentially starts with a gradient search and then smoothly switches to an analytical search (linearizing the fitting function) as the minimum value of χ^2 in the parameter space is approached.

The neutron peaks are fit with a fairly complicated function, which results from attempting to realistically account for all conceivably significant contributions to the observed line shape. The sources and assumed forms of these contributions are listed in Table 1. The total fitting function consists of a quadratic background plus

Table 1 Neutron Resolution Function

Component Source	Assumed Distribution
(1) Electronic plus Beam Burst Time Spread	Gaussian
(2) Scintillator Transit Time	Rectangular
(3) Target Energy Loss	Rectangular
(4) Target Energy Straggling	Gaussian
(5) Beam Energy Spread	Gaussian
(6) Kinematic Broadening	Rectangular
(7) Intrinsic State Width	Lorentzian

a seven-fold integral over these individual distributions, four dimensions of which have been integrated analytically. The remaining three-dimensional integral for the neutron resolution function is evaluated numerically.

The primary need for such a program results from the assumed Lorentzian (Breit-Wigner) intrinsic line shape of the isobaric analog resonances (La 69). The normalized Lorentzian distribution is

$$L(X) = \frac{1}{\pi} \frac{\Gamma/2}{(X-X_0)^2 + (\Gamma/2)^2}, \qquad \text{(II-8)}$$

where X_0 is the centroid and Γ is the width (FWHM). The tails of this function fall off as X^{-2} and are generally indistinguishable from a quadratic background. This is demonstrated in Figure 30, which shows a Gaussian peak (upper line) plus a quadratic background (lower line) fit to a Lorentzian distribution on a constant background. A good fit is obtained, but the Gaussian width and area parameters determined by the search are only 80% and 38%, respectively, of their counterparts for the Lorentzian "data." In this example, the fit interval encompasses 1.5Γ out from the centroid. As this interval is extended, the discrepancy gradually diminishes. By 5Γ, the Gaussian-plus-quadratic fit gives 62% of the Lorentzian area. The increase results from an improved determination of the background. However, a clear fit interval of even $\pm 5\Gamma$ is often unavailable in actual

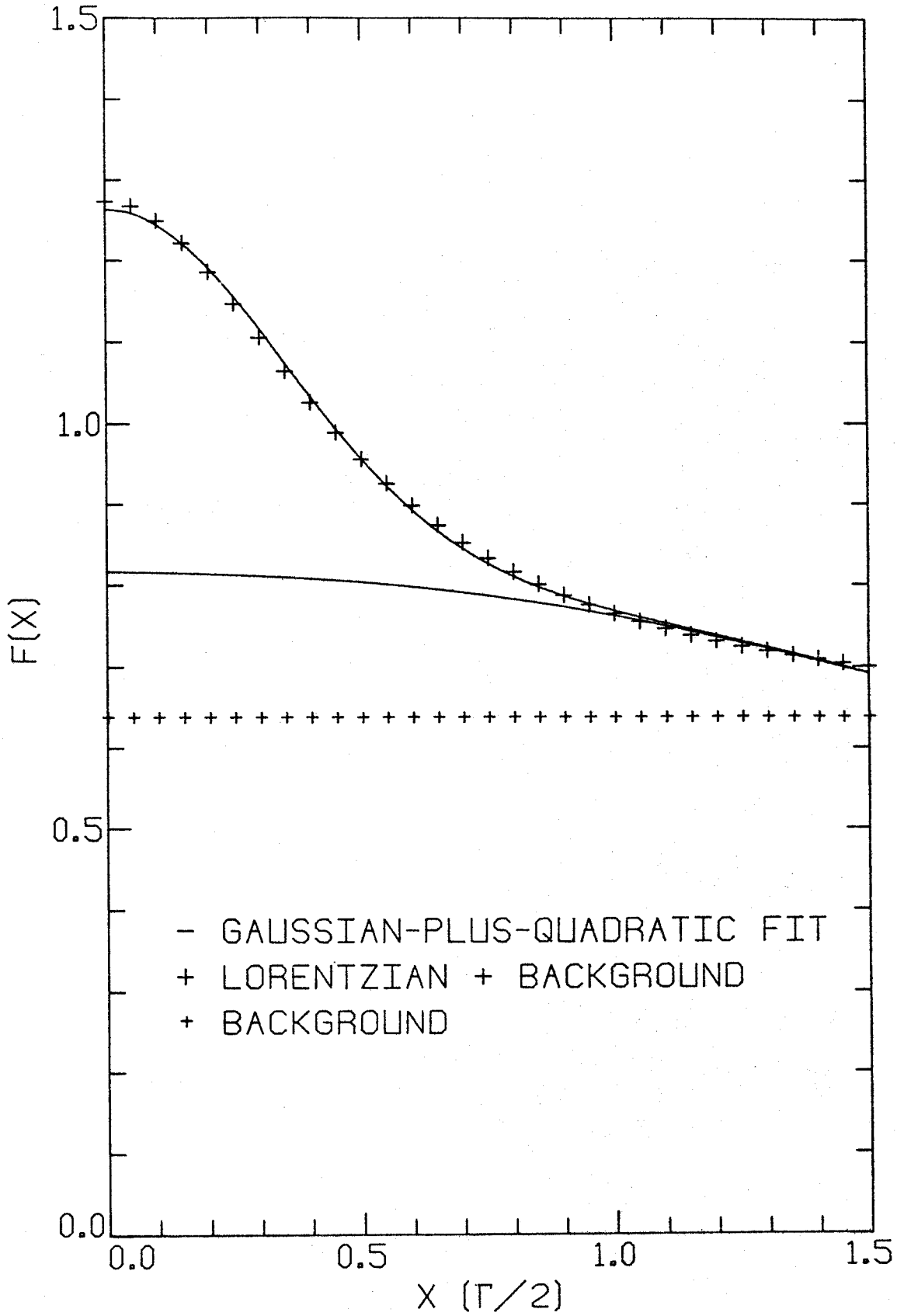

Figure 30. Gaussian-Plus-Quadratic Fit to a Lorentzian Peak

spectra. Furthermore, even if the background in the vicinity of the centroid were exactly known, there would remain a large uncertainty in the area contributed by the tails. This is due to the fact that only 80% of the area of a Lorentzian distribution is within $\pm 1.5\Gamma$ of the centroid, whereas the comparable figure for a Gaussian distribution is over 99.9%

The most significant improvement resulting from the inclusion of a Lorentzian intrinsic line shape in searches on the present data is obtained for the IAS of ^{208}Pb, since it has the largest natural width. Figure 31 displays a pair of fits determined with ANNIE for this state. The fit incorporating a Lorentzian intrinsic shape gives 50% more area above its background than the one based on a Gaussian line shape. Total cross sections of 7.1 ± 0.8 and 9.2 ± 1.0 mb have been obtained from IAS peak areas extracted by hand and with ANNIE, respectively, for ^{208}Pb(p,n)^{208}Bi at 25 MeV. Only the latter value is in agreement with the corresponding (p,n$\bar{p}$) cross section of 10.0 ± 1.0 mb (Cr 74).

3. Neutron Detection Efficiency

The efficiency of the neutron detector described in Section II.C.2 has been calculated with a modified version of the code TOTEFF (Ku 64). Basically this program evaluates probabilities that an incident neutron

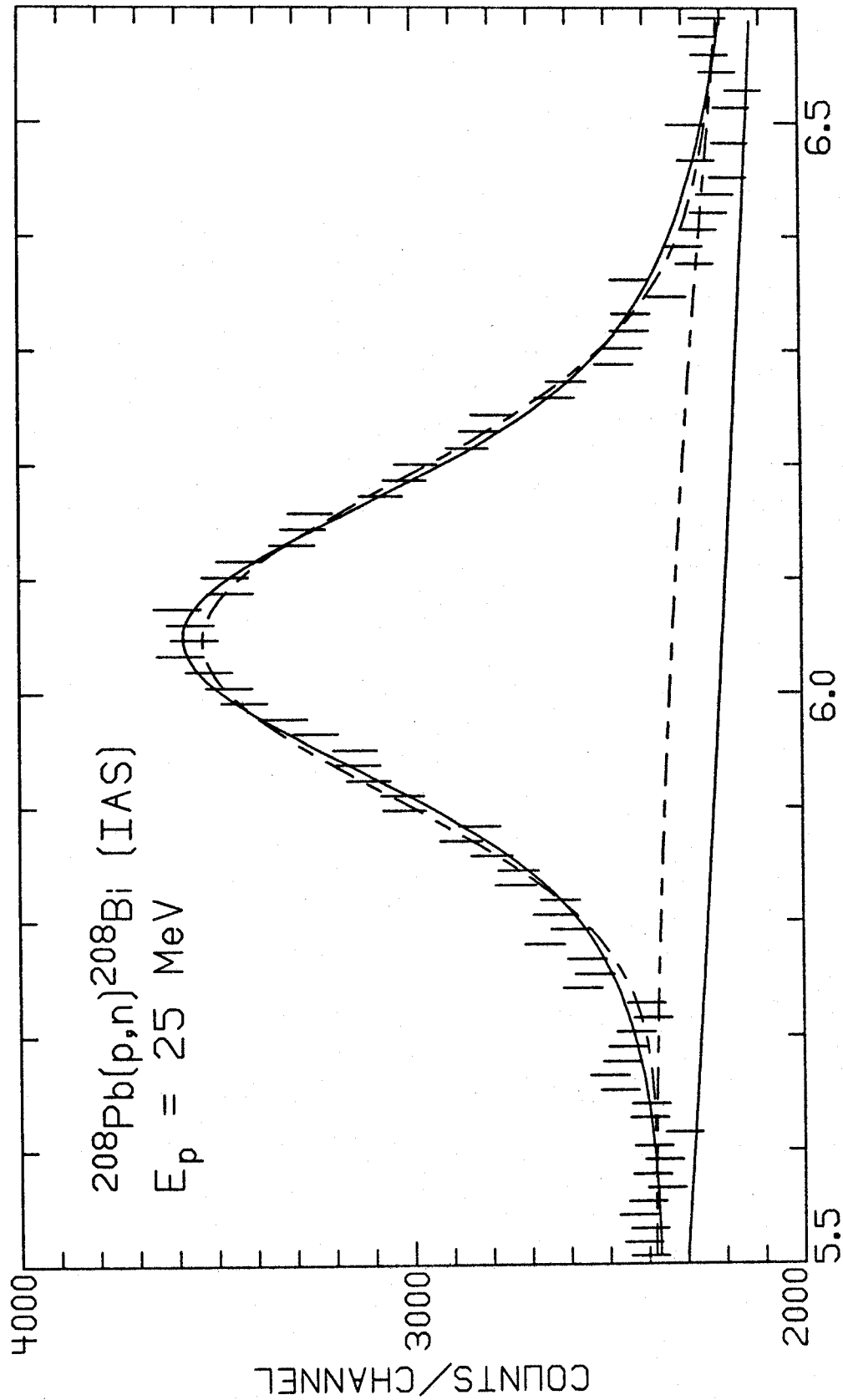

Figure 31. IAS of ^{208}Pb Fit with Lorentzian (solid) and Gaussian (dashed) Peaks Plus Quadratic Backgrounds

of a given energy will induce nuclear reactions whose charged products create more than a specified amount of light. The quantity of light produced in a particular scintillator by an electron losing 1 MeV is the "Light Unit" (L.U.) used in TOTEFF.

The light threshold is controlled with the TSCA. Thus, it is necessary to calibrate the TSCA discriminator dial in Light Units. This has been accomplished in two stages. First, light pulse-height spectra have been taken for the gamma-ray sources listed in Table 2. Only Compton edges are prominent in gamma-ray spectra obtained with such a low-Z scintillator. The Compton edges have been fit with electron-recoil spectra derived from the Klein-Nishina formula (Da 65) and folded with a centrally-Gaussian light-resolution function with exponential tails. A typical fit is displayed in Figure 32. The search parameters are a normalization factor, the energy per spectrum channel, and the standard deviation of the Gaussian distribution. The latter is used to determine the fractional light-energy resolution at the Compton edge, which should be inversely proportional to the square root of the energy loss in the scintillator, as previously discussed for the monitor detector (see Section II.C.1). This is plotted in Figure 33 for each Compton edge and each voltage applied to the PM tube. Since the maximum proton recoil energy in the

Table 2 Gamma-Ray Sources for Neutron Detector Calibration

Source	Gamma-Ray Energies (MeV)
^{22}Na	0.511, 1.275
^{137}Cs	0.662
^{228}Th	2.615
^{239}Pu-^{9}Be	4.440

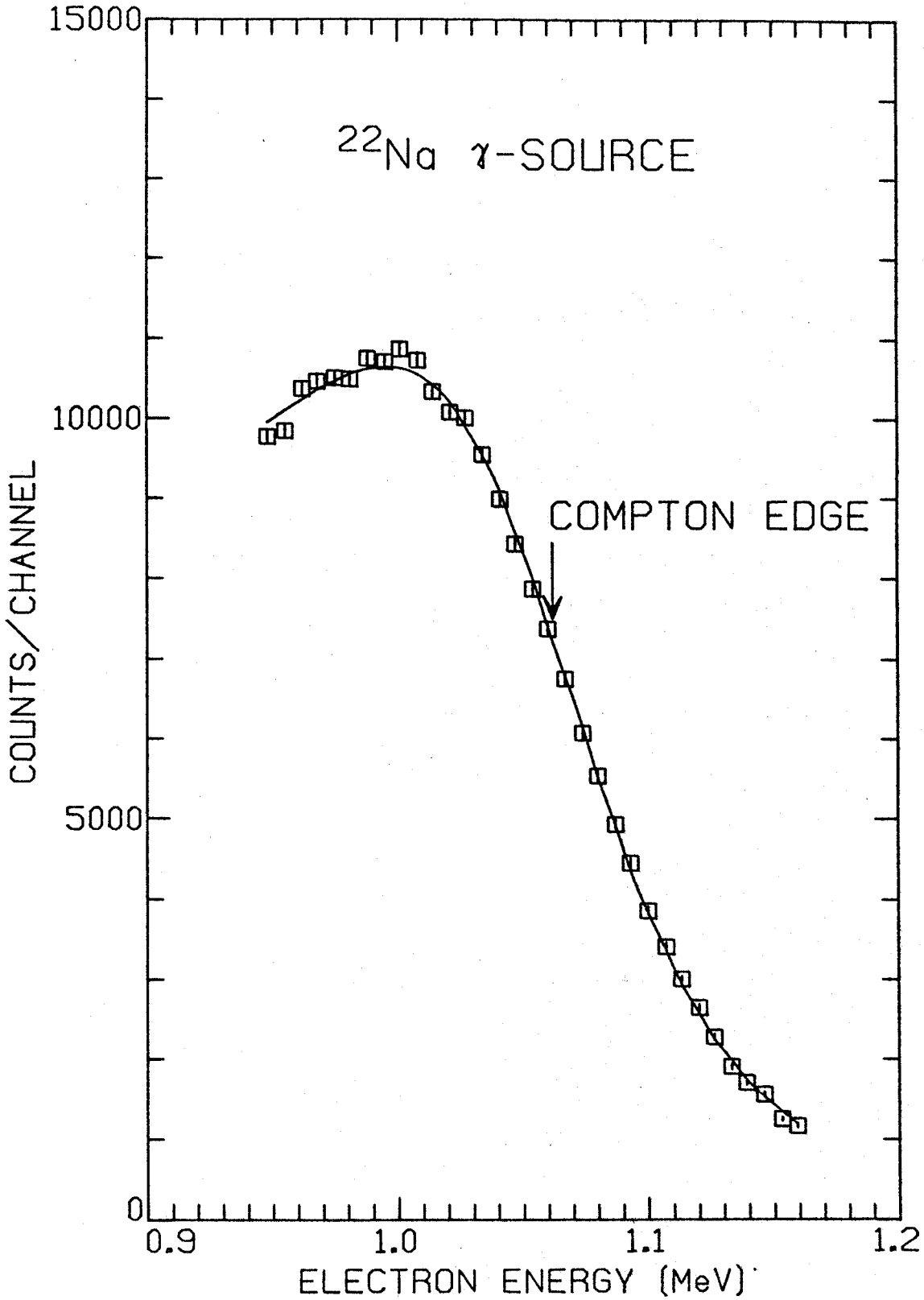

Figure 32. Fit to the Compton Edge for 1.275-MeV Gamma Rays from ^{22}Na

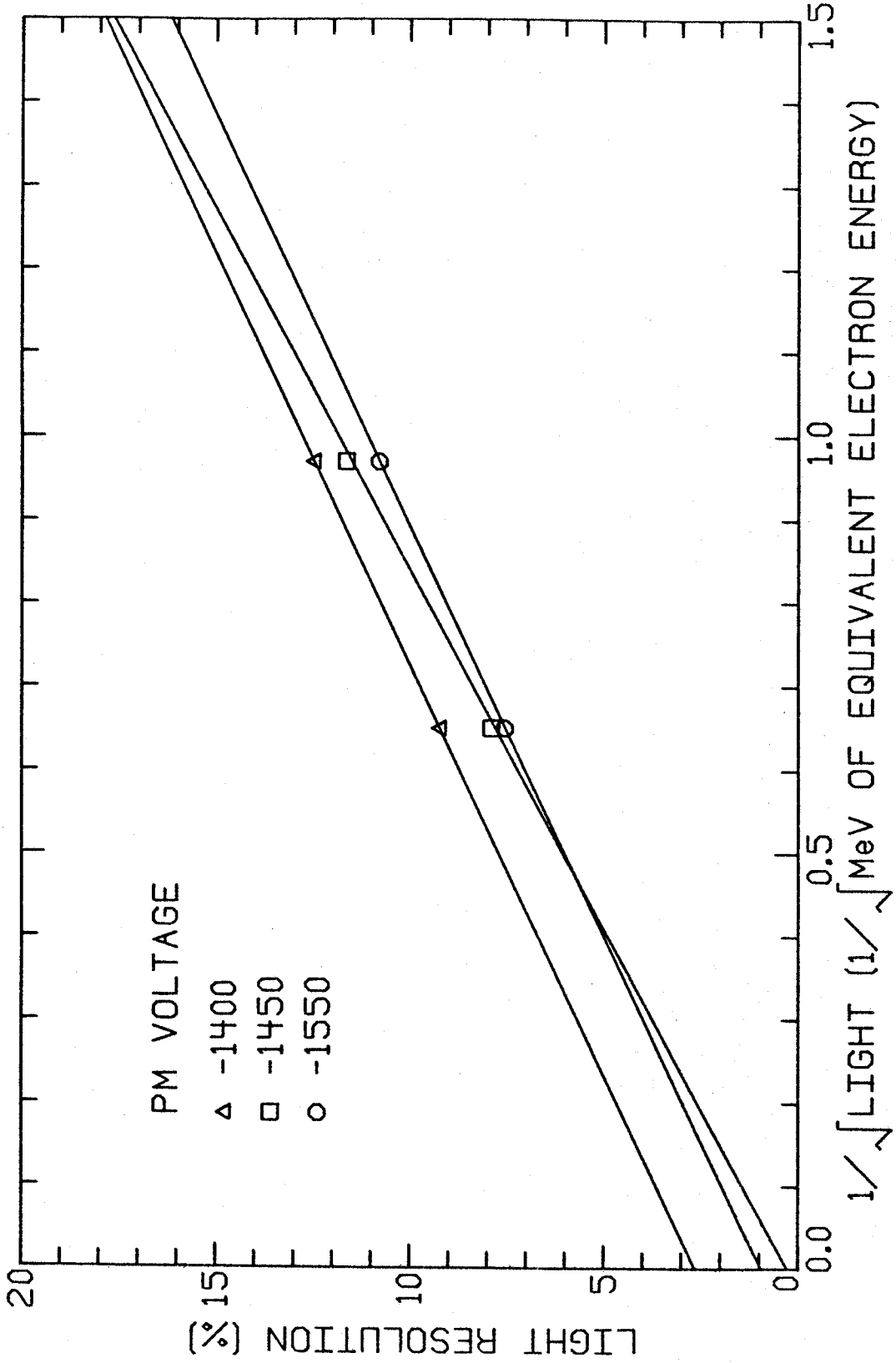

Figure 33. Light Resolution of the Neutron Detector

scintillator increases with the proton energy on the target, it is necessary to lower the PM voltage to avoid saturation of the detector output as the bombarding energy is raised. In this experiment, the PM tube has been operated at 1550, 1450, and 1400 volts for proton energies of 25, 35, and 45 MeV, respectively, and a separate light-threshold calibration is required for each. Additional pulse-height spectra have been taken with a series of TSCA discriminator settings, which cut off the spectra at a set of corresponding channels. Since the channel-energy calibration has been previously determined by the fits to the first group of spectra, this second group completes the calibration of the TSCA discriminator dial in Light Units. The relation between dial setting and "equivalent electron energy" is plotted in Figure 34.

Since the neutron TOF spectra are gated by a band in the LIGHT-PSD plane which encompasses predominantly proton light pulses, only the probabilities for neutron-induced reactions producing protons in the scintillator have been summed to yield the total detector efficiency. The relevant nuclear reactions included in TOTEFF are n-p scattering and $^{12}C(n,p)^{12}B$. The probabilities that these reactions will be induced by final-state neutrons from $^{12}C(n,n'3\alpha)$ and n-p scattering are also considered in the total efficiency. Fortunately, the detection efficiencies calculated for the neutron energies in this

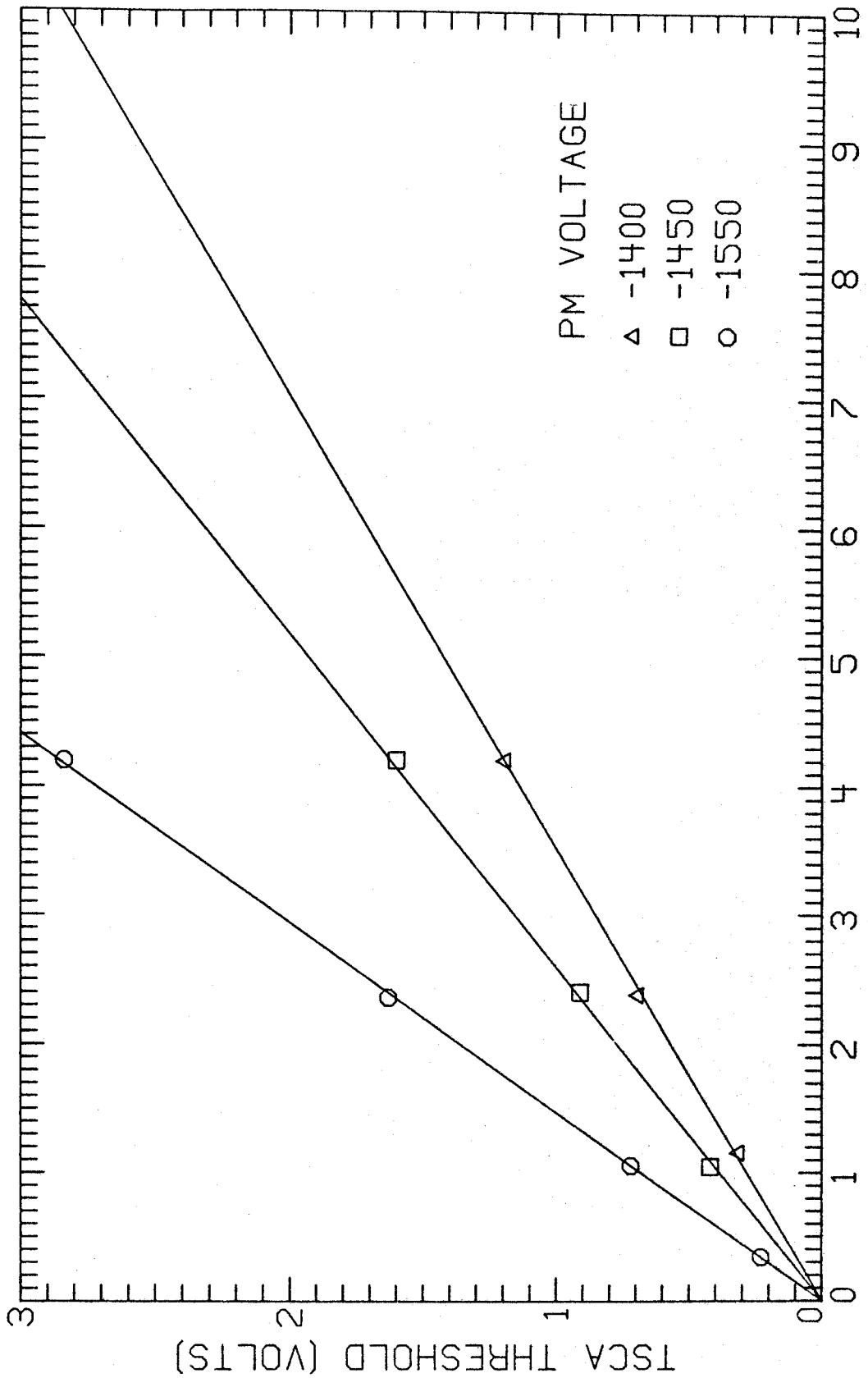

Figure 34. Light-Threshold Calibration of the Neutron Detector

experiment result almost exclusively from relatively well determined n-p scattering cross sections. The original n-p angular distributions in TOTEFF have been replaced with values derived from the Yale phase shifts (Ho 71). A few of the carbon reaction cross sections have also been adjusted to agree with recent measurements. The remaining significant differences between the original and present versions involve the properties of particular scintillators. The scintillator density, hydrogen-carbon ratio, and light response as a function of proton energy ("light-curve") have been replaced with appropriate values for NE 213. In particular, the proton light curve presently employed is

$$L(E) = 0.863E - 3.96(1 - \exp(-0.185E^{0.862})) \text{ L.U.}, \qquad \text{(II-9)}$$

where E is the proton energy in MeV. This function has been determined by fitting NE 213 data (Ve 68) with a parameterized form previously used for NE 102 (Go 60).

Figure 35 displays the efficiency of the detector discussed in Section II.C.2 as a function of incident neutron energy for the lowest and highest light thresholds used in this experiment. Although the efficiency tends to peak not far above threshold, the present data has been acquired in the region where the efficiency is less sensitive to small variations of energy and threshold.

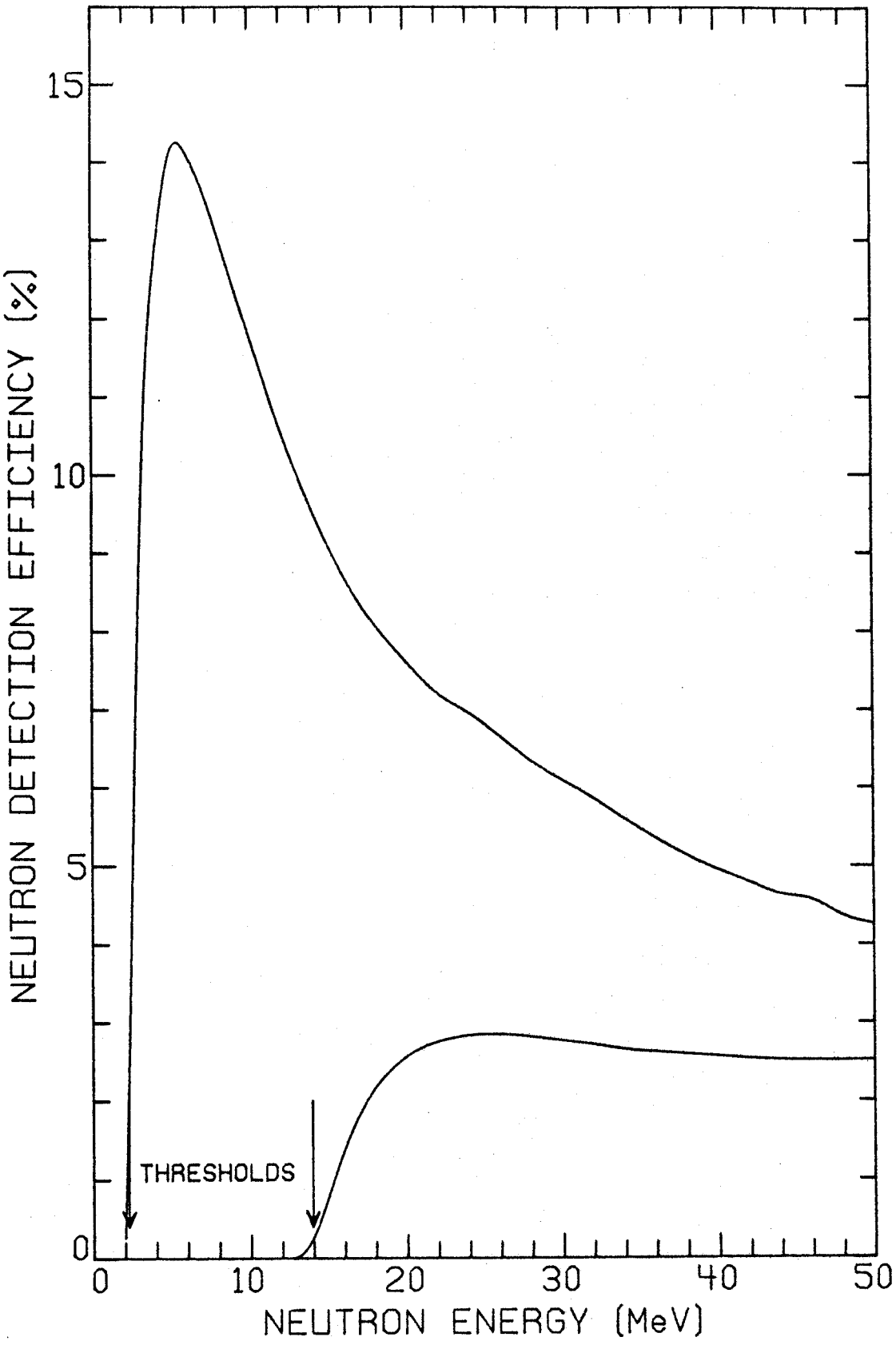

Figure 35. Efficiency of the Neutron Detector

4. Neutron Attenuation

The attenuation of a neutron beam traversing a compound medium is given by

$$I/I_0 = \exp(-0.602(D/W)\sum_i N_i \sigma_i), \qquad \text{(II-10)}$$

where I_0 and I are the initial and final intensities, D and W are the areal density in g/cm^2 and the molecular weight of the medium, and N_i and σ_i are the number of atoms per molecule and removal cross section in barns for the $i^{\underline{th}}$ nuclide in the medium.

In general, the removal cross section is less than the total neutron cross section since some neutrons may be elastically scattered into the beam. For the present geometry, this corresponds to neutrons from the target being scattered into the detector by, e.g. the air. The absorbers discussed in Sections II.B.1-2 (mylar, aluminum, lucite, and air) are generally several meters from the detector, and neutrons elastically scattered by them at all but very forward angles are attenuated by the shielding on the air cart and delayed by longer flight paths en route to the detector. Thus, the removal cross sections have been equated to the total neutron cross sections for these media. In contrast, elastic scattering from the materials immediately surrounding the scintillator (principally reflectance paint and glass;

see Section II.C.2) is not significantly attenuated or delayed with respect to neutrons incident directly from the target. Thus, only the nonelastic neutron cross sections have been used for these absorbers. All cross sections have been obtained from the Brookhaven National Laboratory Sigma Center compilations.

Table 3 lists individual neutron attenuation factors and their product for a typical run in the present experiment. In this case, the number of neutrons from the IAS of the target which reach the detector has been reduced approximately 10% by nuclear reactions occuring along the flight path. Values ranging from about 5% to 20% have been calculated for the other runs.

5. Targets

The ^{48}Ca, ^{90}Zr, ^{120}Sn, and ^{208}Pb targets used in this experiment are self-supporting, rolled foils with thicknesses of 1-30 mg/cm^2 and isotopic enrichments in excess of 96%. Detailed target properties are presented in Table 4. The average thicknesses have been determined directly from measured weights and areas. Uniformity has been checked by comparing the relative energy losses of 5.5-MeV alpha particles through several regions of the approximately 10-mg/cm^2 ^{120}Sn and ^{208}Pb targets. The central densities differ from the average values by less than 5%. The other targets are too thick to be

Table 3 Neutron Attenuation (E_n = 11.59 MeV)

Absorber	Thickness (cm)	I/I_0
Air	463.00	0.965
Aluminum	0.00	1.000
Glass	0.25	0.982
Lucite	0.32	0.963
Mylar	0.05	0.994
Paint	0.08	0.994
Total	--	0.900

Table 4 Target Data

Target	Areal Density (mg/cm^2)	Isotopic Enrichment (%)
^{48}Ca	1.08	96.25
^{90}Zr	2.00	97.80
^{90}Zr	3.00	97.80
^{90}Zr	10.19	98.66
^{90}Zr	10.03	98.66
^{120}Sn	9.90	98.40
^{120}Sn	9.58	98.40
^{208}Pb	5.40	99.14
^{208}Pb	10.22	99.14
^{208}Pb	9.26	99.14
^{208}Pb	30.00	99.14
^{208}Pb	10.05	99.14
^{208}Pb	30.20	99.14

measured with the alpha gauge, except for the ^{48}Ca target, which is maintained under vacuum to inhibit oxidation.

6. Cross Sections

For a reaction which may be asymptotically represented as two-body scattering, the differential cross section may be defined by

$$\sigma(\theta) = \frac{1}{nN} \frac{dY}{d\Omega}(\theta), \qquad \text{(II-11)}$$

where N is the number of particles in a beam incident upon a target with n scattering centers per unit area and Y is the number scattered through an angle θ into a solid angle Ω. For the present experiment, Equation II-11 is equivalent to

$$\sigma(\theta) = 2.66\times10^{-5} \frac{YM\cos(\alpha)}{PQDE(1-T)(1-A)\Omega} \text{ mb/sr}, \qquad \text{(II-12)}$$

where Y is the number of counts in the IAS peak in the neutron TOF spectrum taken at the scattering angle θ, M is the atomic mass of the target in amu, α is the angle between the normal to the target and the incident beam, P is the percent isotopic abundance of the target, Q is the time integral of the beam current in microcoulombs, D is the areal density of the target in mg/cm^2, E is the fractional efficiency of the detector for neutrons from

the IAS of the target, T is the fractional dead-time of the electronics and data-acquisition system, A is the fractional attenuation of neutrons along the flight path, and Ω is the solid angle subtended by the neutron detector.

Table 5 lists the IAS differential cross sections calculated with Equation II-12. Scattering angles and solid angles as measured in the center-of-mass (c.m.) coordinate system have been used. The dominant source of relative errors in the angular distributions is the neutron yield. The errors given in Table 5 result from combining in quadrature statistical and systematic uncertainties in the peak fitting. Since the IAS peak area (yield) is a search parameter, its variance is the corresponding diagonal element of an "error matrix" which is the inverse of the "curvature matrix" defined by

$$C_{jk} = \sum_{i=1}^{N} \frac{1}{Y_i} \frac{\partial F_i}{\partial P_j} \frac{\partial F_i}{\partial P_k} , \qquad \text{(II-13)}$$

where P_j is a search parameter and the remaining quantities are defined as in Section II.F.2 (Be 69A). In addition to these statistical errors in the yields, the search program has been used to evaluate the systematic errors due to uncertainties in the IAS intrinsic widths. The widths employed in the searches for the IAS yields are 20 ± 10 (Be 72), 30 ± 5 (Jo 65), and

Table 5. Measured Differential Cross Sections

48CA(P,N)48SC IAS

E = 25 MEV			E = 35 MEV			E = 45 MEV		
CM ANGLE (DEG)	CM CROSS SECTION (MB/SR)	ERROR (%)	CM ANGLE (DEG)	CM CROSS SECTION (MB/SR)	ERROR (%)	CM ANGLE (DEG)	CM CROSS SECTION (MB/SR)	ERROR (%)
.0	.277E 01	2.9	.0	.401E 00	19.3	.0	.476E 01	5.7
10.3	.232E 01	1.9	10.2	.696E 00	10.0	10.2	.301E 01	5.5
15.4	.196E 01	3.4	15.4	.188E 01	4.3	15.4	.347E 01	5.0
20.5	.175E 01	3.1	20.5	.364E 01	2.4	20.5	.482E 01	4.0
25.6	.175E 01	3.8	25.6	.467E 01	2.5	25.6	.527E 01	3.8
30.7	.162E 01	2.4	30.7	.438E 01	2.5	30.7	.442E 01	3.9
35.8	.143E 01	4.1	35.8	.321E 01	3.3	35.8	.251E 01	9.8
40.9	.127E 01	2.8	40.9	.196E 01	4.6	40.9	.152E 01	18.0
46.0	.118E 01	3.6	46.0	.140E 01	5.7	46.0	.111E 01	11.1
51.1	.127E 01	2.9	51.1	.142E 01	6.9	51.0	.960E 00	12.7
56.2	.132E 01	2.9	56.1	.158E 01	5.5	56.1	.998E 00	19.8
61.3	.125E 01	2.7	61.2	.137E 01	6.1	61.2	.654E 00	12.3
66.3	.118E 01	3.1	66.3	.103E 01	6.9	66.2	.314E 00	38.5
71.4	.109E 01	2.8	71.3	.669E 00	8.7	71.3	.190E 00	25.6
76.4	.105E 01	3.4	76.3	.401E 00	11.1	76.3	.175E 00	14.3
81.4	.906E 00	3.3	81.4	.280E 00	10.4	81.3	.221E 00	37.0
86.5	.796E 00	4.1	86.4	.320E 00	9.1	86.4	.130E 00	35.1
91.5	.586E 00	4.4	91.4	.334E 00	8.3	91.4	.104E 00	28.5
96.5	.416E 00	5.5	96.4	.303E 00	9.4	96.4	.914E-01	24.0
101.4	.446E 00	5.6	101.4	.196E 00	11.3	101.3	.609E-01	35.7
106.4	.463E 00	5.2	106.3	.120E 00	16.6	111.3	.307E-01	67.7
111.4	.566E 00	4.3	111.3	.115E 00	17.7	121.2	.178E-01	58.6
116.3	.624E 00	4.8	116.3	.110E 00	14.9	131.0	.442E-01	35.2
121.3	.494E 00	4.8	121.2	.123E 00	13.8	140.9	.311E-01	51.2
126.2	.357E 00	5.9	126.1	.117E 00	16.1	150.7	.618E-01	107.3
131.1	.210E 00	8.2	131.1	.848E-01	18.2			
136.0	.130E 00	10.1	136.0	.275E-01	67.5			
140.9	.236E 00	7.1	140.9	.324E-01	42.9			
145.8	.380E 00	4.6	145.8	.500E-01	31.7			
150.7	.517E 00	3.8	150.7	.166E 00	13.7			
155.6	.636E 00	3.3	155.6	.164E 00	11.4			
160.5	.536E 00	4.0	160.5	.140E 00	10.2			

Table 5. (cont'd.)

90ZR(P,N)90NB IAS

E = 25 MEV			E = 35 MEV			E = 45 MEV		
CM ANGLE (DEG)	CM CROSS SECTION (MB/SR)	ERROR (%)	CM ANGLE (DEG)	CM CROSS SECTION (MB/SR)	ERROR (%)	CM ANGLE (DEG)	CM CROSS SECTION (MB/SR)	ERROR (%)
.0	.602E 01	3.2	.0	.266E 01	3.9	.0	.487E 00	14.8
10.2	.412E 01	3.5	10.1	.245E 01	3.3	10.1	.119E 01	4.6
15.2	.291E 01	3.7	15.2	.190E 01	4.0	15.2	.226E 01	3.9
20.3	.174E 01	4.1	20.3	.144E 01	5.1	20.3	.290E 01	2.4
25.4	.109E 01	4.8	25.3	.938E 00	6.0	25.3	.246E 01	2.5
30.5	.895E 00	5.2	30.4	.829E 00	5.3	30.4	.155E 01	4.2
35.5	.947E 00	4.9	35.5	.781E 00	5.4	35.4	.112E 01	5.9
40.6	.884E 00	5.1	40.5	.863E 00	4.8	40.5	.112E 01	4.0
45.6	.801E 00	5.3	45.6	.101E 01	4.2	45.6	.107E 01	5.0
50.7	.715E 00	5.5	50.6	.860E 00	4.3	50.6	.739E 00	5.5
55.7	.554E 00	5.1	55.7	.666E 00	5.3	55.6	.344E 00	7.8
60.8	.480E 00	5.3	60.7	.477E 00	6.8	60.7	.241E 00	10.5
65.8	.429E 00	5.6	65.7	.338E 00	8.3	65.7	.260E 00	8.1
70.9	.431E 00	5.4	70.8	.379E 00	8.5	70.7	.221E 00	7.1
75.9	.424E 00	5.3	75.8	.386E 00	6.4	75.8	.155E 00	8.5
80.9	.373E 00	5.8	80.8	.422E 00	6.7	80.8	.413E-01	28.3
85.9	.353E 00	6.0	85.8	.214E 00	9.6	85.8	.533E-01	16.0
90.9	.363E 00	5.6	90.8	.161E 00	15.9	90.8	.574E-01	15.7
95.9	.365E 00	4.6	95.8	.116E 00	11.5	95.8	.511E-01	19.0
100.9	.350E 00	4.6	100.8	.159E 00	12.3	100.8	.601E-01	20.4
105.9	.314E 00	4.8	105.8	.135E 00	9.2	105.8	.209E-01	26.4
110.9	.225E 00	5.4	110.8	.128E 00	9.6	110.7	.224E-01	33.6
115.8	.177E 00	6.1	115.7	.731E-01	13.1	115.7	.244E-01	28.8
120.8	.200E 00	5.8	120.7	.457E-01	19.8	120.7	.164E-01	38.8
125.7	.269E 00	4.9	125.7	.492E-01	18.2	125.6	.191E-01	32.0
130.7	.329E 00	4.5	130.6	.792E-01	11.4	130.6	.125E-01	36.2
135.6	.275E 00	4.8	135.6	.903E-01	12.6	135.6	.237E-01	58.0
140.6	.200E 00	5.7	140.5	.787E-01	19.2	140.5	.227E-01	22.8
145.5	.122E 00	7.5	145.5	.177E-01	38.9	145.4	.195E-01	35.2
150.5	.173E 00	6.0	150.4	.274E-01	36.2	150.4	.124E-01	25.2
155.4	.365E 00	4.4	155.3	.645E-01	11.2	155.3	.196E-01	26.6
160.3	.579E 00	3.8	160.3	.106E 00	7.4	160.3	.178E-01	27.3

Table 5. (cont'd.)

**********	^{120}SN(P,N)^{120}SB IAS	**********
E = 25 MEV	E = 35 MEV	E = 45 MEV

CM ANGLE (DEG)	CM CROSS SECTION (MB/SR)	ERROR (%)	CM ANGLE (DEG)	CM CROSS SECTION (MB/SR)	ERROR (%)	CM ANGLE (DEG)	CM CROSS SECTION (MB/SR)	ERROR (%)
.0	.665E 01	1.9	.0	.128E 02	2.1	.0	.570E 01	3.1
10.1	.432E 01	2.4	10.1	.672E 01	1.5	10.1	.385E 01	2.2
15.2	.330E 01	3.1	15.2	.324E 01	2.5	15.2	.351E 01	2.4
20.2	.235E 01	3.5	20.2	.115E 01	6.0	20.2	.281E 01	2.9
25.3	.251E 01	3.5	25.3	.588E 00	10.3	25.3	.161E 01	4.3
30.4	.254E 01	3.3	30.3	.689E 00	8.0	30.3	.129E 01	6.2
35.4	.248E 01	3.3	35.4	.109E 01	4.2	35.3	.175E 01	3.5
40.5	.210E 01	3.6	40.4	.128E 01	3.7	40.4	.190E 01	2.9
45.5	.147E 01	4.5	45.4	.104E 01	3.9	45.4	.118E 01	4.8
50.6	.844E 00	6.4	50.5	.653E 00	6.1	50.5	.564E 00	8.7
55.6	.512E 00	9.0	55.5	.441E 00	8.8	55.5	.610E 00	8.4
60.6	.441E 00	10.0	60.5	.431E 00	7.0	60.5	.613E 00	8.2
65.7	.492E 00	8.4	65.6	.559E 00	5.8	65.5	.521E 00	10.3
70.7	.542E 00	8.2	70.6	.504E 00	6.5	70.6	.253E 00	10.7
75.7	.589E 00	6.8	75.6	.336E 00	6.2	75.6	.156E 00	13.0
80.7	.532E 00	8.0	80.6	.180E 00	9.5	80.6	.153E 00	13.1
85.7	.385E 00	9.1	85.6	.151E 00	12.5	85.6	.127E 00	17.6
90.7	.223E 00	10.4	90.6	.188E 00	9.4	90.6	.111E 00	18.6
95.7	.168E 00	8.7	95.6	.165E 00	9.1	95.6	.585E-01	21.5
100.7	.224E 00	7.1	100.6	.149E 00	10.3	100.6	.582E-01	22.1
105.7	.264E 00	6.7	105.6	.923E-01	14.1	105.6	.381E-01	37.2
110.7	.243E 00	6.6	110.6	.905E-01	12.3	110.6	.228E-01	23.9
115.7	.193E 00	7.3	115.6	.908E-01	13.4	115.5	.297E-01	35.6
120.6	.164E 00	9.8	120.5	.564E-01	17.0	120.5	.260E-01	37.1
125.6	.148E 00	12.2	125.5	.630E-01	29.7	125.5	.202E-01	87.3
130.6	.148E 00	8.6	130.5	.580E-01	14.2	130.5	.168E-01	54.5
135.5	.193E 00	8.5	135.4	.905E-01	13.8	135.4	.253E-01	39.1
140.5	.152E 00	9.3	140.4	.626E-01	24.5	140.4	.126E-01	60.9
145.4	.139E 00	11.2	145.4	.299E-01	17.7	145.3	.882E-02	141.3
150.4	.107E 00	10.9	150.3	.141E-01	41.3	150.3	.213E-02	202.0
155.3	.227E 00	7.1	155.3	.391E-01	14.5	155.3	.123E-01	41.2
160.2	.302E 00	5.8	160.2	.897E-01	9.5	160.2	.205E-01	28.4

Table 5. (cont'd.)

********** ^{208}PB(P,N)^{208}BI IAS **********

E = 25 MEV			E = 35 MEV			E = 45 MEV		
CM ANGLE (DEG)	CM CROSS SECTION (MB/SR)	ERROR (%)	CM ANGLE (DEG)	CM CROSS SECTION (MB/SR)	ERROR (%)	CM ANGLE (DEG)	CM CROSS SECTION (MB/SR)	ERROR (%)
.0	.234E 01	9.7	.0	.839E 01	7.0	.0	.203E 02	4.2
10.1	.238E 01	7.4	10.1	.438E 01	5.6	10.1	.653E 01	3.8
15.1	.253E 01	7.4	15.1	.279E 01	7.3	15.1	.204E 01	5.6
20.2	.238E 01	7.5	20.1	.362E 01	6.4	20.1	.102E 01	11.0
25.2	.213E 01	7.4	25.2	.385E 01	5.9	25.2	.135E 01	6.6
30.3	.170E 01	7.8	30.2	.300E 01	7.1	30.2	.157E 01	5.4
35.3	.136E 01	8.8	35.2	.139E 01	10.9	35.2	.112E 01	6.3
40.4	.116E 01	8.5	40.3	.563E 00	13.0	40.2	.541E 00	9.5
45.4	.123E 01	8.2	45.3	.558E 00	16.3	45.3	.577E 00	10.2
50.4	.147E 01	7.9	50.3	.746E 00	10.4	50.3	.871E 00	7.1
55.5	.161E 01	7.7	55.3	.733E 00	9.5	55.3	.679E 00	7.7
60.5	.136E 01	7.9	60.4	.519E 00	11.6	60.3	.354E 00	12.4
65.5	.106E 01	8.5	65.4	.219E 00	17.2	65.3	.268E 00	17.0
70.5	.765E 00	9.1	70.4	.218E 00	28.5	70.4	.435E 00	11.1
75.5	.543E 00	9.7	75.4	.232E 00	18.1	75.4	.294E 00	11.7
80.6	.583E 00	10.1	80.4	.326E 00	12.6	80.4	.172E 00	15.0
85.6	.560E 00	9.5	85.4	.226E 00	11.0	85.4	.136E 00	23.5
90.6	.543E 00	10.1	90.4	.143E 00	18.5	90.4	.113E 00	15.6
95.6	.529E 00	9.6	95.4	.915E-01	15.6	95.4	.109E 00	14.6
100.6	.366E 00	11.1	100.4	.116E 00	14.2	100.4	.642E-01	18.2
105.5	.293E 00	13.4	105.4	.192E 00	8.2	105.4	.638E-01	25.4
110.5	.238E 00	14.6	110.4	.136E 00	16.2	110.4	.659E-01	25.0
115.5	.229E 00	15.8	115.4	.935E-01	13.5	115.3	.741E-01	23.3
120.5	.248E 00	13.9	120.4	.697E-01	16.9	120.3	.295E-01	29.1
125.5	.278E 00	13.7	125.3	.944E-01	11.3	125.3	.357E-01	31.1
130.4	.195E 00	20.3	130.3	.719E-01	18.4	130.3	.403E-01	27.2
135.4	.220E 00	16.3	135.3	.532E-01	14.9	135.3	.262E-01	37.9
140.4	.225E 00	20.5	140.3	.761E-01	14.4	140.2	.219E-01	45.2
145.3	.166E 00	20.5	145.2	.134E 00	9.5	145.2	.391E-01	25.7
150.3	.178E 00	25.6	150.2	.757E-01	13.2	150.2	.468E-01	22.4
155.2	.133E 00	25.0	155.2	.327E-01	30.9	155.2	.880E-02	117.8
160.2	.183E 00	19.1	160.1	.103E 00	13.0	160.1	.165E-01	65.4

220 ± 20 KeV (Le 68) for the analogs of ^{90}Zr, ^{120}Sn, and ^{208}Pb, respectively. Additional searches have also been performed with the largest widths consistent with these values. The resulting differences in yields have been used as the appropriate systematic errors.

The principal error in the absolute magnitude of the cross sections is the estimated ±10% reliability of the neutron detection efficiency calculations (Ku 64 and Th 71). There are also small uncertainties in target thickness, beam current integration, and neutron attenuation along the flight path, which may introduce additional systematic errors estimated to be less than 5%.

The differential cross sections in Table 5 have been integrated over scattering angle to yield the total cross sections listed in Table 6. The corresponding errors have been obtained by adding the aforementioned relative and absolute errors in quadrature.

Table 6 (p,n)-IAS Total Cross Sections

Target	E_p (MeV)	σ_T (mb)
^{48}Ca	25	10.6 ± 1.2
	35	10.2 ± 1.1
	45	8.4 ± 1.0
^{90}Zr	25	6.7 ± 0.8
	35	4.8 ± 0.5
	45	4.4 ± 0.5
^{120}Sn	25	8.5 ± 1.0
	35	5.6 ± 0.6
	45	5.8 ± 0.7
^{208}Pb	25	9.2 ± 1.0
	35	6.7 ± 0.8
	45	5.3 ± 0.6

III. DATA ANALYSIS

A. Calculations

Except for the presence of an effective two-body scattering operator rather than the free two-body potential, the direct scattering amplitude in the single-inelastic-scattering approximation (Equation I-14) is equivalent to the corresponding DWBA amplitude (Equation I-12). Thus, if the effective interaction defined by Equation I-13 may be represented by a local pseudopotential such as in Equation I-16, conventional DWBA programs may be used to compute the cross sections.

The theoretical angular distributions in Figure 36 have been calculated with the code DWBA70 (Sc 70), which incorporates the helicity formalism developed by Raynal (Ra 67). This program is applicable to inelastic scattering and charge-exchange reactions in which the state of the residual nucleus may be expressed as a sum of particle-hole pairs with respect to the target ground state. Thus, the scattering amplitude is decomposed into a series of terms each representing the creation of a particle-hole pair with a spectroscopic amplitude (Ma 66) defined by

$$Z_J(n_p,n_h) = (2J+1)^{-\frac{1}{2}}(2J_I+1)^{-\frac{1}{2}}\langle\Phi_F|A_J^+(n_p,n_h)|\Phi_I\rangle\ , \qquad \text{(III-1)}$$

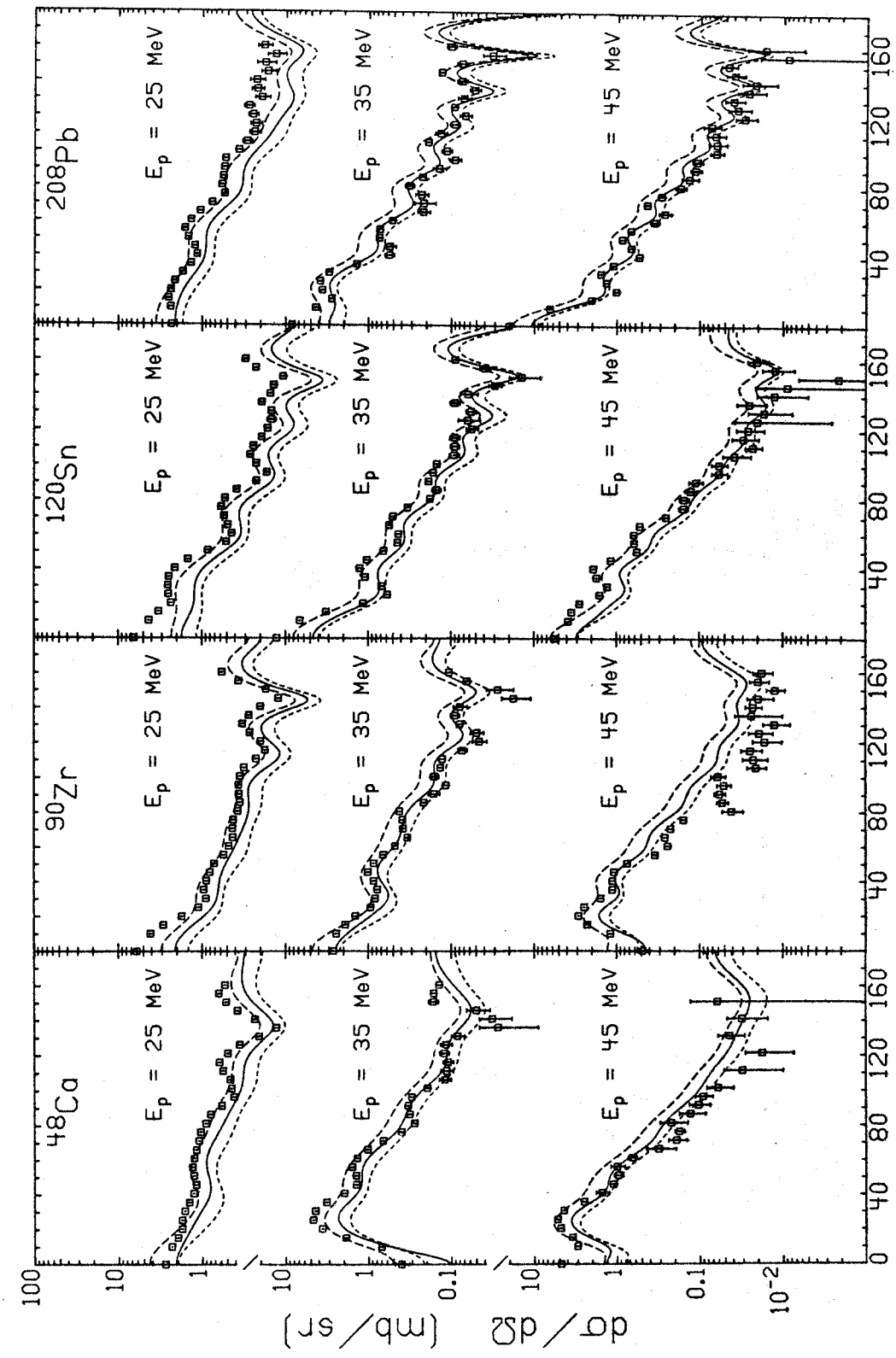

Figure 36. Comparison of Experimental and Theoretical (p,n)-IAS Angular Distributions

where J is the total angular momentum transferred, J_I is the spin of the target, and $A_J^+(n_p,n_h)$ is the creation operator for a particle in a state labeled by n_p and a hole in state n_h, with their angular momenta coupled to J. For charge-exchange transitions between $J^\pi=0^+$ analog states, Equation III-1 may be reduced with the aid of Equation I-18 to

$$Z_0(n) = (2j_n+1)^{-\frac{1}{2}}(2T_>)^{-\frac{1}{2}} \sum_m |C_m|^2 (T_{mn}(T_{mn}+1)-T_{mn}^z(T_{mn}^z-1)), \qquad \text{(III-2)}$$

where

$$\Phi_I = \Phi_{GS}(T=T_>) = \sum_m C_m \left| \prod_n \Phi_n \right\rangle_m,$$

Φ_n is a "single-particle orbit" (Bo 69) with quantum numbers labeled by n (e.g., its angular momentum j_n), m labels the occupation numbers for the orbits and the couplings required to complete the specification of a particular term in the target wavefunction, and T_{mn} is the combined isospin of the nucleons in the n^{th} orbit for the m^{th} term. For the present analysis, the ground state of ^{120}Sn has been represented by a BCS wavefunction based on average occupation probabilities derived from phenomenological values for ^{119}Sn and ^{121}Sn (Gi 67). Elementary shell-model configurations have been assumed for the other targets: $(1f_{7/2})^8$, $0.8(1g_{9/2})^{10} + 0.6(1g_{9/2})^8(2p_{1/2})^2$, and $(1h_{9/2})^{10}(2f_{7/2})^8(1i_{13/2})^{14}$

$(3p_{3/2})^4(2f_{5/2})^6(3p_{1/2})^2$ for the excess neutrons in ^{48}Ca, ^{90}Zr, and ^{208}Pb, respectively. The single-particle wavefunctions have been calculated in a potential well of the form

$$U(r) = -U_0 f(r) + U_{so} \lambda\!\!\!^{-2} \frac{1}{r} \frac{d}{dr} f(r) \underline{l}\cdot\underline{\sigma} , \quad \text{(III-3)}$$

where

$$f(r) = \left(1 + \exp\left(\frac{r - r_0 A^{1/3}}{a_0}\right)\right)^{-1};$$

$$\underline{l}\cdot\underline{\sigma} = j(j+1) - l(l+1) - s(s+1);$$

r_0=1.3 F, a_0=0.7 F, $\lambda\!\!\!^{-}$=2.0 F, U_{so}=6 MeV, A is the mass number of the target; l, s, and j are the orbital, spin, and total angular momentum quantum numbers, respectively, of the bound nucleon; and U_0 has been adjusted to reproduce the observed binding energies (except for the unbound IAS protons in ^{90}Nb, ^{120}Sb, and ^{208}Bi, which DWBA70 treats as bound by 0.01 MeV). The binding energy of a neutron in a particular target orbit is the separation energy of the least bound neutron (Wa 71) plus the excitation energy of the corresponding neutron-hole state in the isotope of the target element with mass number A-1. The binding energy of a proton in the "analog" orbit is reduced from the neutron value by the amount of kinetic energy converted into mass by the (p,n)-IAS reaction, which is 7.175 MeV for a ^{48}Ca target (Ra 70), 12.03 MeV for ^{90}Zr (Ca 72), 13.41 MeV for ^{120}Sn

(Ca 72), and 18.82 MeV for ^{208}Pb (Cr 72). The optical-model potentials used for the proton and neutron distorted waves have been taken from the "Coulomb-corrected" analysis of Becchetti and Greenlees (Be 69). If the optical-model and bound-state potentials were the same, the exchange scattering amplitude in Equation I-4 would reduce to the "knockon" amplitude (Au 70A), which is evaluated by DWBA70 without a local approximation (Pe 70).

The dashed curves in Figure 36 result from phenomenological nucleon-nucleon forces consistent with Austin's analysis (Au 72). In particular, the effective interaction has been taken to have the form given in Equation I-16, with a 1.0-F-Yukawa radial dependence and V_0=-27 MeV, V_σ=$V_{\sigma\tau}$=12 MeV, and V_τ=12 and 18 MeV. The solid curves have been calculated with a realistic force derived from the Reid soft-core potential (Re 68) by Bertsch (Be 72B), who employed the method of Barrett, Hewitt, and McCarthy (Ba 71) to solve for the corresponding G-matrix in a harmonic-oscillator basis. For compatibility with DWBA70, a superposition of four Yukawa potentials (with ranges of 0.2, 0.4, 0.5, and 0.7 F) has been determined by fitting harmonic-oscillator matrix elements to the original G-matrix (Bo 74). Only the central, even-state terms have been retained for the present calculations,

since the central, odd interaction appears to be weak (Bo 74).

B. Results

Both the phenomenological and realistic forces yield angular distributions which follow the data but are somewhat smoother. The similarity in shape of the dashed and solid curves in Figure 36 results from the $0^+ \rightarrow 0^+$ IAS transition being dominated by the monopole component of $V_\tau g_\tau(r_{ij})$. With the 1.0-F-Yukawa form for g_τ, the average values of V_τ required to reproduce the (p,n)-IAS total cross sections (Table 6) measured at proton energies of 25, 35, and 45 MeV are 19.6, 15.3, and 13.3 MeV, respectively. The spread for individual targets combined with the experimental errors (Section II.F.6) indicates that these values are reliable within about $\pm$2 MeV, which suggests that V_τ is now determined in this energy range at least as well as V_0 and $V_{\sigma\tau}$ (Au 72).

The present phenomenological values of V_τ are consistent with the microscopic analysis of Batty et al. for (p,n)-IAS reactions on ^{27}Al, ^{54}Fe, and ^{56}Fe at 30 and 50 MeV (Ba 68). There is also agreement with the isospin-flip strength extracted by Clough et al. from (p,n)-IAS transitions in 1p-shell nuclei at 50 MeV (Cl 70). However, their value of V_τ at 30 MeV, even

when corrected for the lack of an exchange amplitude in their calculations (Au 72), is about 50% larger than that indicated by the present study. This discrepancy may simply reflect the greater sensitivity which they observe to the selection of optical-model potentials for the calculations at 30 MeV coupled with the relatively large uncertainty in this choice for such light nuclei (Gr 68, Ho 71A).

The G-matrix interaction produces nearly the same cross sections for the reactions investigated in this work as a 1.0-F-Yukawa potential with V_t=14 MeV. Thus, it accounts for the data quite well at 45 MeV and fairly well at 35 MeV. However, the experimental cross sections at 25 MeV are consistently larger than predicted. Love and Satchler have found the same difficulty for ^{90}Zr(p,n)^{90}Nb(IAS) at 18.5 MeV in a study employing another realistic effective interaction (Lo 70), the long-range part of the Hamada-Johnston potential (Ha 62). The volume integrals of the isospin-flip components of this potential and the long-range part of the Kallio-Kolltveit potential (Ka 64) are the same as for 1.0-F Yukawas with $V_t \approx 12$ and 14 MeV, respectively (Au 72), in close agreement with the monopole charge-exchange strength of the G-matrix for the Reid soft-core potential.

The great similarity of the IAS and ground state wavefunctions generally produces large (p,n)-IAS cross sections which are relatively insensitive to details of the DWBA calculations other than an approximate proportionality to V_τ^2. In particular, additional calculations have been performed for $^{90}Zr(p,n)^{90}Nb(IAS)$ at 35 MeV with $\Phi_{GS}=(1g_{9/2})^{10}$, $r_0=1.25$ and $a_0=0.65$, the Becchetti-Greenlees "best-fit" optical-model potential (Be 69), and noncentral (spin-orbit and tensor) components of the G-matrix interaction (Bo 74), all with very little effect on the resulting angular distributions. Unfortunately, the M.S.U. version of DWBA70 has no provision for including an imaginary term in the effective interaction, the influence of which would also be interesting to investigate. For (p,p') reactions, it has been noted that a complex force generally yields a relative increase of the forward-angle cross sections and enhances the overall oscillatory structure of the angular distributions (Sa 72), both of which would improve the agreement of the theoretical curves in Figure 36 with the data.

The phenomenological values for $V_\tau(E_p)$ obtained in the present study give slopes of -0.4 and -0.2 for the ranges 25-35 and 35-45 MeV, respectively, in contrast to a corresponding number of about -0.83 for 30-50 MeV (-0.75 with exchange corrections (Au 72)) derived from the previous work of Clough et al. (Cl 70). Thus,

although the isospin-flip component of the effective nucleon-nucleon interaction appears to be stronger at low energies than the theoretical predictions, the present results indicate that V_τ is leveling off as the bombarding energy increases. Furthermore, for proton energies from about 35 to at least 45 MeV, the isospin-flip strengths of realistic forces are consistent with the (p,n)-IAS data.

LIST OF REFERENCES

LIST OF REFERENCES

Al 61 K. Alexander and F. Goulding, Nucl. Instr. Meth. 13, 244 (1961).

An 61 J.D. Anderson and C. Wong, Phys. Rev. Lett. 7, 250 (1961).

An 64 J.D. Anderson, C. Wong, J.W. McClure, and B.D. Walker, Phys. Rev. 136, 118 (1964).

Au 70 R. Au, Michigan State University Cyclotron Laboratory SIGMA-7 Program Description #12, unpublished (1970).

Au 70A N. Austern, Direct Nuclear Reaction Theories (New York, John Wiley & Sons, 1970).

Au 72 S.M. Austin, "The Effective Two-Nucleon Interaction from Inelastic Proton Scattering," in The Two-Body Force in Nuclei, ed. by S.M. Austin and G.M. Crawley (New York, Plenum Press, 1972).

Ba 68 C.J. Batty, B.E. Bonner, E. Friedman, C. Tschalar, L.E. Williams, A.S. Clough, and J.B. Hunt, Nucl. Phys. A116, 643 (1968).

Ba 71 B.R. Barrett, R.G.L. Hewitt, and R.J. McCarthy, Phys. Rev. C3, 1137 (1971).

Ba 71A D.L. Bayer, Michigan State University Cyclotron Laboratory Report MSUCL-34, unpublished (1971).

Ba 72 B.R. Barrett, "The Effective Two-Body Interaction in Finite Nuclei and its Calculation," in The Two-Body Force in Nuclei, ed. by S.M. Austin and G.M. Crawley (New York, Plenum Press, 1972).

Ba 73 B.R. Barrett and M.W. Kirson, "The Microscopic Theory of Nuclear Effective Interactions and Operators," in Advances in Nuclear Physics, Vol. 6, ed. by M. Baranger and E. Vogt (New York, Plenum Press, 1973).

Be 69 F.D. Becchetti, Jr., and G.W. Greenlees, Phys. Rev. 182, 1190 (1969).

Be 69A P.R. Bevington, Data Reduction and Error Analysis for the Physical Sciences (New York, McGraw-Hill Book Company, 1969).

Be 72 G.F. Bertsch and A. Mekjian, Ann. Rev. Nucl. Sci. 22, 25 (1969).

Be 72A H.A. Bethe, "An Effective Reaction Matrix Derived from Nuclear Matter Calculations," in The Two-Body Force in Nuclei, ed. by S.M. Austin and G.M. Crawley (New York, Plenum Press, 1972).

Be 72B G.F. Bertsch, The Practitioner's Shell Model (Amsterdam, North-Holland Publishing Co., 1972).

Bo 69 A. Bohr and B.R. Mottelson, Nuclear Structure, Vol. 1, (New York, W.A. Benjamin, 1969).

Bo 74 J. Borysowicz, H. McManus, and G. Bertsch, Michigan State University Cyclotron Laboratory Report, and to be published (1974).

Ca 72 J.D. Carlson, Ph.D. Thesis, University of Colorado, unpublished (1972).

Cl 70 A.S. Clough, C.J. Batty, B.E. Bonner, and L.E. Williams, Nucl. Phys. A143, 385 (1970).

Cr 72 G.M. Crawley, P.S. Miller, A. Galonsky, T. Amos, and R. Doering, Phys. Rev. C6, 1890 (1972).

Cr 74 G.M. Crawley, P.S. Miller, R. Doering, A. Galonsky, and D. Patterson, to be published.

Da 65 C.M. Davisson, "Interaction of Gamma Radiation with Matter," in Alpha-, Beta-, and Gamma-Ray Spectroscopy, Vol. 1, ed. by K. Siegbahn, (Amsterdam, North-Holland Publishing Co., 1965).

De 61 T.J. Devlin, University of California Report UCRL-9727, unpublished (1961).

De 72 N.B. DeTakacsy, Phys. Lett. 42B, 1 (1972).

Fa 72 W.L. Fadner, J.J. Kraushaar, and S.I. Hayakawa, Phys. Rev. C5, 859 (1972).

Fe 62 R.P. Feynman, Theory of Fundamental Processes (New York, W.A. Benjamin, 1962).

Gi 67 V. Gillet, B. Giraud, and M. Rho, Nucl. Phys. A103, 257 (1967).

Go 60 J. Gooding and H. Pugh, Nucl. Instr. Meth. 58, 253 (1968).

Go 64 M.L. Goldberger and K.M. Watson, Collision Theory (New York, John Wiley & Sons, 1964).

Gr 68 A.E.S. Green, T. Sawada, and D.S. Saxon, The Nuclear Independent Particle Model (New York, Academic Press, 1968).

Ha 62 T. Hamada and I.D. Johnston, Nucl. Phys. 34, 382 (1962).

Hi 72 R.A. Hinrichs and D.L. Show, Phys. Rev. C6, 1257 (1972).

Ho 71 J.C. Hopkins and G. Breit, Nucl. Data Tables 9, 137 (1971).

Ho 71A P.E. Hodgson, Nuclear Reactions and Nuclear Structure (Oxford, Clarendon Press, 1971).

Jo 65 C.H. Johnson and R.L. Kernell, Oak Ridge National Laboratory Physics Division Annual Progress Report ORNL-3778, unpublished (1965).

Jo 73 R.K. Jolly, T.M. Amos, A. Galonsky, R. Hinrichs, and R. St. Onge, Phys. Rev. C7, 1903 (1973).

Ka 64 A. Kallio and K. Kolltveit, Nucl. Phys. 53, 87 (1964).

Ke 59 A.K. Kerman, H. McManus, and R.M. Thaler, Ann. Phys. 8, 551 (1959).

Ku 64 R. Kurz, University of California Report UCRL-11339, unpublished (1964).

La 68 A. Langsford, P.H. Bowen, G.C. Cox, and M.J.M. Saltmarsh, Nucl. Phys. A113, 433 (1968).

La 69 A.M. Lane, "Fine Structure in Analogue States," in Isospin in Nuclear Physics, ed. by D.H. Wilkinson (Amsterdam, North-Holland Publishing Co., 1969).

Le 68 G.H. Lenz and G.M. Temmer, Nucl. Phys. A112, 625 (1968).

Lo 70 W.G. Love and G.R. Satchler, Nucl. Phys. A159, 1 (1970).

Ma 63 D.W. Marquardt, J. Soc. Ind. Appl. Math. 11, 431 (1963).

Ma 66 V.A. Madsen, Nucl. Phys. 80, 177 (1966).

Ma 70 P. Marmier and E. Sheldon, Physics of Nuclei and Particles, Vol. 2, (New York, Academic Press, 1970).

Mc 68 W.J. McDonald and D.A. Gedcke, "Electronics for Fast Neutron Work," in Proceedings of the International Symposium on Nuclear Electronics, Versailles (1968).

Ne 87 I. Newton, Principia Mathematica (1687).

Ok 58 S. Okubo and R.E. Marshak, Ann. Phys. 4, 166 (1958).

Pe 70 F. Petrovich, Ph.D. Thesis, Michigan State University, unpublished (1970);
F. Petrovich, H. McManus, V.A. Madsen, and J. Atkinson, Phys. Rev. Lett. 22, 895 (1969).

Ra 67 J. Raynal, Nucl. Phys. A97, 572 (1967).

Ra 70 J. Rapaport, Nuclear Data Sheets B4, 351 (1970).

Re 68 R. Reid, Ann. Phys. 50, 411 (1968).

Ri 73 L.D. Rickertsen and P.D. Kunz, Phys. Lett. 47B, 11 (1973).

Ro 64 M. Roush, M. Wilson, and W. Hornyak, Nucl. Instr. Meth. 31, 112 (1964).

Ro 67 R.R. Roy and B.P. Nigan, Nuclear Physics (New York, John Wiley & Sons, 1967).

Ro 67A L.S. Rodberg and R.M. Thaler, Introduction to the Quantum Theory of Scattering (New York, Academic Press, 1967).

Sa 67 G.R. Satchler, Nucl. Phys. A95, 1 (1967).

Sa 72 G.R. Satchler, Comm. Nucl. Part. Phys. A5, 39 (1972).

Sc 70 R. Schaeffer, Center for Nuclear Studies of Saclay Report CEA-R-4000, unpublished (1970).

Se 64 E. Segre, Nuclei and Particles (New York, W.A. Benjamin, 1964).

Sl 68 D. Slanina and H. McManus, Nucl. Phys. A116, 271 (1968).

So 69 J.M. Soper, "Isospin Purity of Low-Lying Nuclear States," in Isospin in Nuclear Physics, ed. by D.H. Wilkinson (Amsterdam, North-Holland Publishing Co., 1969).

St 73 W.F. Steele, Michigan State University Cyclotron Laboratory Computer Program, unpublished (1973).

Ta 73 H. Tawara and A. Russek, Rev. Mod. Phys. 45, 178 (1973).

Th 71 S.T. Thornton and J.R. Smith, Nucl. Instr. Meth. 96, 551 (1971).

Ve 68 V.V. Verbinski, W.R. Burrus, T.A. Love, W. Zobel, and N.W. Hill, Nucl. Instr. Meth. 65, 8 (1968).

Vo 68 E. Vogt, "The Statistical Theory of Nuclear Reactions," in Advances in Nuclear Physics, Vol. 1, ed. by M. Baranger and E. Vogt (New York, Plenum Press, 1968).

Wa 57 K.M. Watson, Phys. Rev. 105, 1388 (1957).

Wa 71 A.H. Wapstra and N.B. Gove, Nuclear Data Tables 9, 265 (1971).

Wi 69 D.H. Wilkinson, "Historical Introduction to Isospin," in Isospin in Nuclear Physics, ed. by D.H. Wilkinson (Amsterdam, North-Holland Publishing Co., 1969).

Wi 71 R.A. Winyard, J.E. Lutkin, and G.W. McBeth, Nucl. Instr. Meth. 95, 141 (1971).